Theoretical Discovery and Experimental Synthesis of Ultra-wide-band-gap Semiconductors for Power Electronics

by

Sieun Chae

A dissertation submitted in partial fulfillment
of the requirements for the degree of
Doctor of Philosophy
(Materials Science and Engineering)
in the University of Michigan
2022

Doctoral Committee:

Assistant Professor John Heron, Co-Chair
Associate Professor Emmanouil Kioupakis, Co-Chair
Professor Zetian Mi
Professor Pierre F. P. Poudeu

Sieun Chae
sieun@umich.edu
ORCID iD: 0000-0002-9489-9023

ACKNOWLEDGEMENTS

Personal acknowledgements

First and foremost, I would like to express my sincere gratitude to my two supervisors, Professor Manos Kioupakis and Professor John Heron. They not only provided excellent guidance throughout my research but also continuously supported me for my professional development. It is an honor for me that they are my PhD advisors, and they will remain as my role model forever.

I would also like to thank my group members. Special thanks to Jihang Lee, Logan Williams, Zihao Deng, Kyle Bushick, Nocona Sanders, Peter Meisenheimer, and Steve Novakov, who gave a lot of help for my research. Thanks also to Kelsey Mengle and Nguyen Vu for our successful collaboration and for being one of my best friends.

The work in this dissertation would not have been possible without the contributions from my collaborators, particularly, Hanjong Paik who gave me endless support and invaluable advice for experimental work and Lucas Pressley who contributed to bulk crystal growth in this project.

Most importantly, I am deeply grateful to my family for supporting all my decisions and being with me during my PhD study.

Funding acknowledgements

The projects in this work were supported through a variety of sources. I gratefully acknowledge the NSF PARADIM under Cooperative Agreement No. DMR-1539918, NSF DMREF Award No. 1534221, NSF Award No. DMR 1810119 (bulk and thin film synthesis and structural characterization), and the Rackham Graduate School. The computational work used the DOE NERSC facility under Contract No. DE-AC02-05CH11231 and the XSEDE facility under NSF grant No. ACI-1548562. I acknowledge the Rackham international student fellowship and Rackham predoctoral

fellowship.

TABLE OF CONTENTS

LIST OF FIGURES

FIGURE

LIST OF TABLES

ABSTRACT

Semiconductors have unique electrical properties such as variable electrical conductivity through doping, making them an essential component of modern electronics. Silicon is the traditional semiconductor material that governs modern microelectronic technology. However, with the advent of artificial intelligence (AI), big data, autonomous vehicles, and Internet of Things (IoT), there is a need for developing advanced semiconductor materials that can operate more energy-efficiently at high power and high frequency. Power electronics is the application of electronics to the control and conversion of electrical power and it seeks to enhance energy conversion efficiency by utilizing ultra-wide-band-gap (> 3.4 eV, UWBG) semiconductors with high carrier mobility and high thermal conductivity. However, materials with wide band gaps generally have heavy effective masses which lead to inefficient charge transport and doping. The state-of-the-art materials suffer from doping asymmetry and/or poor thermal conductivity, which motivates alternative UWBG semiconductors with enhanced material properties.

This thesis investigates theoretical discovery and experimental synthesis of novel UWBG semiconductors that can overcome the challenges faced by the state-of-the-art materials. To discover the extreme limits to semiconductor band gap, wide-band-gap materials are surveyed and the key material factors are identified which enables semiconductivity of materials. It is found that materials composed of light elements and crystallized in densely packed structures give rise to a combination of

wide band gap and light effective mass that enables shallow dopant, high mobility, and weakly bound polarons. For the candidate semiconductors, atomistic calculations are performed to explicitly calculate dopant ionization energies, formation of DX centers, and carrier mobility. Calculation results revealed promising semiconductor materials with band gaps up to 11.6 eV (even wider than insulators), which challenges the conventional gap-based criterion to distinguish semiconductors from insulators.

Among the materials, rutile GeO_2 (r-GeO_2) is identified to be a promising, yet unexplored UWBG (4.68 eV) semiconductor for rapid transformative impact of power electronic applications. Hybrid density functional theory predicted shallow ionization energies for donors such as Sb_{Ge}, As_{Ge}, and F_O, and the ionization energy of 0.45 eV for Al acceptor that can be lowered by heavy Al doping to enable ambipolar doping. The electron and hole mobilities are also calculated (289 cm^2 V^{-1} s^{-1} and 28 cm^2 V^{-1} s^{-1}, respectively), which are close to the state-of-the-art semiconductors such as GaN. Thermal conductivity is also measured for hot-pressed r-GeO_2 polycrystals using laser-flash. The measured value is 51 W m^{-1} K^{-1}, 3 times higher than β-Ga_2O_3. Though thin film growth of r-GeO_2 is challenging due to the presence of kinetically stable glass phase and high vapor pressure of GeO, the first synthesis of single crystal r-GeO_2 thin films is demonstrated using molecular beam epitaxy. Due to the competitive phase space, growth conditions that utilize a novel preoxidized molecular precursor as well as buffer layers with reduced misfit strain are key to realizing the rutile phase. Though the available substrates all have large lattice difference with r-GeO_2 ($> 4\%$), flux synthesis technique and mechanical polishing allow the fabrication of 4×2 mm^2 size r-GeO_2 single crystal substrates with highly crystalline surfaces that can be utilized for epitaxial film growth. This work provides opportunities to realize new UWBG semiconductors with enhanced material properties that can drive energy-efficient power electronics.

CHAPTER I

Introduction

1.1 What is a semiconductor?

Materials are classified into metals, semiconductors, and insulators based on their electrical conductivity. Semiconductors have intermediate conductivities, generally from 10^{-6} to 10^{4} $(\Omega \cdot m)^{-1}$, and have unique electrical properties such as variable electrical conductivity, heterojunection, or light emission, which enable applications in devices therefore become one of the most important class materials in modern microelectronic technology.

According to the band theory[18], the electrical conduction in a semiconductor is attributed to the carriers that are thermally excited from the valence band to the conduction band, and therefore the magnitude of the band gap has been applied as a criterion to distinguish semiconductors from insulators. E.g., materials with relatively narrow band gap ($E_g < 2$ eV) are classified as semiconductors, while wider-gap materials ($E_g > 2$ eV) are identified as insulators.[19] Although conventional semiconductors have relatively narrow gaps (e.g, E_g 1 eV for Si), ultra-wide-band-gap semiconductors such as high Al-content $Al_xGa_{1-x}N$, diamond, and β-Ga_2O_3 are recently discovered as candidate materials to improve the efficiency of high-power electronics. The band gap of these materials ranges from 3.5 eV to 6.2 eV, which would have traditionally been classified in the range of insulators, challenging the gap-based criterion for material

classification.

Then, what is the most important material parameter that distinguishes semiconductors from insulators? Semiconductors are distinct from insulators in that they host delocalized mobile charge carriers that can conduct electricity with high mobility. Intentional doping by impurity atoms is the traditional way of generating free carriers. According to the Bohr model, the dopant ionization energy is given by

$$E^{Bohr}[eV] = 13.6\frac{m^*}{\epsilon_0^2} \tag{1.1}$$

where m^* is an effective mass and ϵ_0 is a static dielectric constant. Charge carriers can also be generated at polar interfaces where the polarization-induced electric field confines carriers at the interface forming two-dimensional electron and hole gases.[20–22] The generated carriers should not be trapped by the interaction with lattice distortions to form polarons. The formation energy of a polaron is given by[15]

$$\frac{E_{polaron}}{E_{Ha}} = -\frac{25}{512}\frac{m^*/m_e}{\epsilon_{eff}^2} \tag{1.2}$$

where ϵ_{eff} is the effective dielectric response obtained by separating the ionic (ϵ_0) from the electronic (ϵ_∞) dielectric response:

$$\frac{1}{\epsilon_{eff}} = \frac{1}{\epsilon_\infty} - \frac{1}{\epsilon_0} \tag{1.3}$$

Carrier mobility characterizes how quickly free carriers can move under an electric field and is defined as

$$\mu = \frac{e\tau}{m^*} \tag{1.4}$$

where τ is scattering time.

Therefore, a light effective mass (m^*) is the key material parameter that simultaneously produces shallow dopants, high carrier mobility, and low polaron dissociation

energies, thus enables semiconducting behavior. Also, ultra-wide-band-gap semiconductors are distinguished from insulators not by a band gap but by a light effective mass. For any material, its electronic band structure contains the information of band gap and effective mass, thus, understanding the properties of band structure is the basis to determine the usefulness of a particular material for semiconductor application.

Various semiconductor materials are developed from elemental Si to III-V compounds or alloys, and each demonstrates its unique physical properties driving different applications that vary from electronics to optoelectronics. In the following chapters, we will explore common semiconductor materials and their applications, and highlight the need for ultra-wide-band-gap semiconductors for the next-generation electronics.

1.2 Traditional semiconductors

The first-generation semiconductor material is Si, Ge, and SiGe. The first working transistor was demonstrated in Ge in 1947.[23] It was not until the late 1950's that Si has become the dominant semiconductor. With a breakthrough in developing the process of thermally grown silicon dioxide to passivate the surface, the first silicon MOSFET (metal-oxide-semiconductor field-effect-transistor) was developed and became the most common type of transistor.[24,25] The rapid growth of Si technology has been predicted by 'Moore's law', i.e., the number of transistors in a silicon chip doubles every year.[26]

Then, the III-As and III-P families have been of interest for the second-generation of semiconductor materials. Unlike Si and Ge, these materials not only have direct band gaps, which is useful for optoelectronic devices, but also allow band gap engineering by compositional modulation of alloys, which allows new type of devices such as high electron mobility transistors (HEMTs) or heterojunction bipolar tran-

sistors (HBTs). In the 1960s, InP laser diodes were first invented.[27] In the 1970s, the discovery of a two-dimensional electron gas (2DEG) at the AlGaAs/GaAs heterojunction has enabled the first HEMTs in GaAs and the development of GaAs- and InGaAs-based HBTs has improved the handling signal frequencies above 10 GHz.[28,29]

With the demands of light emission in the shorter wavelength for optoelectronics as well as higher breakdown voltage for electronics, wide-band-gap (In)GaN and SiC have emerged as the third-generation semiconductor materials. Low-cost, efficient white LEDs using InGaN were commercialized in the 2000's. The 2014 Nobel Prize is awarded for developing methods to activate p-type doping of GaN which enabled GaN blue light emitting diodes (LEDs).[30] The advances in material synthesis of SiC and GaN enabled power devices that can handle a significant power over GaAs-based transistors owing to its much higher critical breakdown field. SiC- and GaN-based electronics are particularly useful for power electronics applications such as electric vehicles, power supplies, or photovoltaic inverters.

1.3 Ultra-wide-band-gap semiconductors

1.3.1 Opportunities

As the wide-band-gap (WBG, $E_g < 3.4$ eV) semiconductors continue to mature, ultra-wide-band-gap (UWBG) semiconductors with band gaps significantly wider than 3.4 eV are researched to revolutionarily improve device performance over the conventional WBG semiconductors. UWBG semiconductors have many useful characteristics that allow new capabilities in electronic/optoelectronic devices.

The most important application of UWBG semiconductors is high-power electronics. For any electrical appliances, it is important that the raw power is converted to a form that is usable in different applications. Power electronics deals with controlling and converting electrical power for the desired specifications, e.g., AC to DC converter

(rectifier), DC to AC converter (inverter), amplifiers, or switches. The most critical factors in designing power electronics are power handling amount and efficiency to minimize the energy losses. Based upon the assumption that power losses are resistive thermal dissipation, Baliga figure of merit (BFOM)[31,32] is commonly used to quantify the efficiency of a low-frequency unipolar power switches, and is defined as:

$$BFOM = \frac{V_{BR}^2}{R_{ON-SP}} \tag{1.5}$$

where V_{BR} is the breakdown voltage (the maximum voltage that can be handled) and R_{ON-SP} is the resistance of the device in the on-state multiplied by the device area. In terms of material parameters, the BFOM can be also expressed as:

$$BFOM = \frac{1}{4}\epsilon_0 \mu E_C^3 \tag{1.6}$$

where ϵ_0 is the static dielectric constant, μ is the carrier mobility, and E_C is the dielectric breakdown field. As the breakdown field scales approximately as the square of the semiconductor band gap, the BFOM scales approximately as the sixth power of the semiconductor band gap (Figure 1.1). Therefore, UWBG semiconductors are extremely advantageous in power electronics with the device performance enhanced by orders-of-magnitude.

UWBG semiconductors are also advantageous in high-frequency technologies. RF power transistors are required for electronic systems that transmit signals into air or space and high output power is desired to improve signal/noise ratio. The inherent limit on the output power that a high frequency device can obtain is determined by the power-frequency limit:

$$f_\tau V_{BR} \leq \frac{E_C v_s}{\pi} \tag{1.7}$$

where f_τ is the cutoff frequency and v_s is the saturated velocity.[33] Therefore, f_τ and

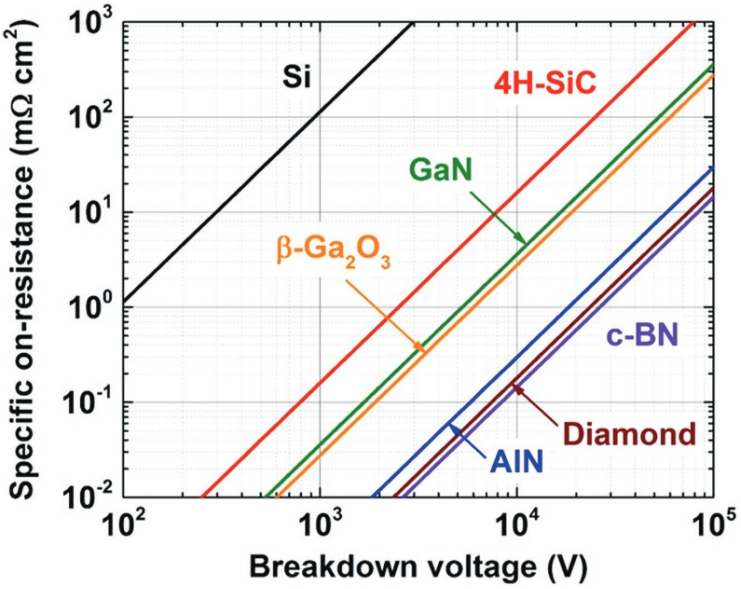

Figure 1.1: Contours of constant Baliga figure-of-merit (BFOM) for various semiconductors, drawn on specific on-resistance versus breakdown voltage plot, printed with permission from Ref.[1]

V_{BR} have to be traded against each other and a higher-breakdown-field allows higher output voltage at given f_τ or higher frequencies at a given supply voltage. The power-frequency limit defines the Johnson Figure of merit (JFOM),[34] which is used to measure the suitability of a material for RF power application. UWBG semiconductors have large JFOM owing to its high breakdown field, showing the promise for RF-power applications.

In optoelectronics, UWBG semiconductors have a band gap range that allows ultraviolet (UV) light detection and emission, particularly UV-B (315 – 280 nm) and UV-C (280 – 200 nm). UV-C radiation is highly effective in killing against viruses and bacteria, suitable for water disinfection or biomedical applications. Also, UV radiation in solar-bind region (240 – 280 nm) is easy to detect a target signal due to little background interference, thus is useful for defense warning systems and communication. While traditional sources in the UV are mercury lamp or excimer which has limited applicability due to its bulky, heavy, and hazardous characteristics and high-

voltage operation, solid-state lighting based on UWBG semiconductors is compact, easy to integrate, and does not contain hazardous substances. Therefore, potential role for UWBG semiconductors in UV LEDs, lasers, solar-bind photodetectors is highly impactful.

1.3.2 Challenges with current materials

A trio of materials have been a particular focus of UWBG semiconductor research: high Al-content $Al_xGa_{1-x}N$, diamond, and β-Ga_2O_3, which have experimentally demonstrated reasonable performance in unipolar field-effect transistors and/or UV light-emitting devices.[1] However, the emerging UWBG semiconductor materials all have significant drawbacks.

For example, $Al_xGa_{1-x}N$ alloy has a direct band gap spanning a wide range (3.4 to 6.0 eV) and a high electron mobility (room-temperature mobility up to 300 cm^2 V^{-1} s^{-1} for AlN)[4], which can be exploited for various electronic and optoelectronic requiring heterostructure and band gap engineering. However, the absence of readily available single-crystal substrates (e.g., an AlN substrate with negligible bowing and low dislocation densities) and difficulty in controlling over doping are the main challenges of $Al_xGa_{1-x}N$.[35] Particularly, both n-type and p-type doping efficiencies decrease with Al content as the dopant ionization energy increases and compensating defects form more easily with increasing x.[36,37] Though Si/Mg is a possible donor/acceptor in $Al_xGa_{1-x}N$, the mobility is suppressed by alloy-disorder scattering.[38]

Diamond has outstanding material properties such as an ultra-wide-band-gap (5.4 eV), high electron and hole mobility (1060 cm^2 V^{-1} s^{-1} for electron and 2000 cm^2 V^{-1} s^{-1} for hole) and a highest known thermal conductivity of any material (¿ 2000 W m^{-1} K^{-1}).[39] However, it also suffers from limited size and poor quality of substrate and inefficient doping especially for n-type doping. Due to the small lattice constant of diamond, the range of dopants that fit into the lattice is severely limited, and the

best substitutional donor (phosphorus) has high activation energy of 0.57 eV.[40,41]

β-Ga_2O_3 is currently the subject of intensive research activity due to the availability of affordable semi-insulating native substrates and good controllability of n-type conduction (n = 10^{15} – 10^{19} cm^{-3}) through Si or Sn doping.[42,43] However, it has poor thermal conductivity (11 W m^{-1} K^{-1} (‖a) and 27 W m^{-1} K^{-1} (‖b)) which limits device operation due to inefficient heat removal.[44] In addition, it cannot be p-type doped which prevents its application to bipolar devices. The two challenges are associated with its low-symmetric, monoclinic crystal structure that leads to flat valence band (thus, heavier hole effective mass) and phonon band folding.[45]

In order to overcome the challenges with the current UWBG semiconductors, alternative UWBG semiconductors must be identified and assessed. The important material properties that need to be assessed for realizing energy efficient, high-power devices are the possibility of n-/p-type doping, high carrier mobilities to reduce energy dissipation during device operation, and high thermal conductivity to efficiently remove the generated waste heat. In addition, the possibility of ambipolar doping can extend its application to bipolar devices.

1.3.3 Goals of this thesis

The goal of the dissertation research is to define semiconductor for clear material classification, discover novel UWBG materials with predicted power electronic metrices that surpass the current materials, synthesize a promising candidate material and experimentally validate its properties to realize power devices with enhanced performance and energy efficiency by transforming the state-of-the-art materials.

1.4 Computational methods

In this dissertation, we applied first-principles calculations based on density functional theory to predict electronic properties of materials. In Chapter 2, we utilized

hybrid density functional theory and defect calculations to computationally discover extreme-gap semiconductors. The same techniques are also utilized in Chapter 3 to predict band structure and dopability of rutile GeO_2.

1.4.1 Density functional theory

Density functional theory (DFT) is first-principles methods that solve the electronic structure of atoms, molecules, and solids. DFT has strong predictive power with relatively low computational cost that can be applied to almost any kind of atomic system. Particularly, predicting fundamental properties of semiconductor materials starts from the accurate prediction of electronic structure which makes DFT an indispensable and practical tool for semiconductor research.

The basis of DFT is the Hohenberg-Kohn theorem.[46] It states that the ground state of a system of many interacting electrons is a functional only of the electron density, ρ. Instead of focusing on the eigenfunctions of individual electrons which are complex numbers with amplitude, the theorem reformulates the many-body problem as an equivalent single-particle problem determined uniquely by the electron density, which reduces the computational problem. Kohn and Sham developed the theorem into a set of mathematical equations that can be solved.27 According to the Kohn-Sham equations:

$$E[\rho] = T_s[\rho] + \int dr v_{ext}(r)\rho(r) + E_H[\rho] + E_{xc}[\rho] \tag{1.8}$$

where $T_s[\rho]$ is the kinetic energy, v_{ext} is the external (ion) potential, E_H is the Coulomb interaction energy of electron density interacting with itself, and E_{xc} is the potential energy from all many-body effects of exchange and correlation. Since the Kohn-Sham operator depends on the density itself and the solution of Kohn-Sham equation yields the orbitals that determine the density, the Kohn-Sham system can be solved

self-consistently and the ground state density and energy are obtained when the convergence is achieved.

The major problem with DFT is that the exact form of E_{xc} is not known and approximate functionals have to be made based upon the electron density. Common approximations include the local-density approximation (LDA) or generalized-gradient approximation (GGA), however, the band gap of a material predicted by these approximations are often underestimated by 50%. Therefore, theories and methods beyond these approximations are proposed for the accurate prediction of a band gap.

1.4.2 Hybrid density functional theory

Hybrid density functional theory approximates the exchange-correlation energy functional that linearly combine a portion of exact exchange from Hatree-Fock theory with the rest of exchange-correlation energy from explicit density functionals. The hybrid functional of Heyd-Scuseria-Ernzerhof (HSE) has shown dramatically improved prediction on solid-state properties relative to semilocal functionals. The HSE functional partitions the Coulomb potential into two ranges and incorporates only short-range HF exchange.

$$E_{xc}^{HSE} = \alpha E_x^{HF,SR}(\omega) + (1-\alpha)E_x^{PBE,SR}(\omega) + E_x^{PBE,LR}(\omega) + E_c^{PBE} \tag{1.9}$$

where α is the mixing parameter, ω is an adjustable parameter controlling the range-separation, $E_x^{HF,SR}(\omega)$ is the short-range Hartree-Fock exact exchange functional, $E_x^{PBE,SR}(\omega)$ and $E_x^{PBE,LR}(\omega)$ are the short-range and long-range components of the PBE exchange functional, and $E_c^{PBE}(\omega)$ is the PBE correlation functional. The HSE06 functional selects the standard values of $\alpha = 0.25$ and $\omega = 0.2$, which has been proven to correct over-delocalization of GGA functional and give an accurate result to most material systems.

1.4.3 Defect calculation

The control of point defects and impurities plays a key role in the electrical/optical properties of semiconductors. For example, shallow dopants (i.e., impurities with small ionization energies) provide mobile carriers that enable n-type or p-type electrical conduction of semiconductors. Deep level defects (i.e., defects with the charge transition level in the band gap far from band edges) act as recombination centers by interacting with both holes from the valence bands and electrons from the conduction bands and affect optical absorption or luminescence. Yet, many point-defect properties are challenging to characterize experimentally, since the point defect-related phenomena occur at the length scale of individual atoms and defect concentrations are in a dilute limit. Modern defect calculations based on hybrid density functional theory have evolved into a powerful tool to characterize defects. In this methodology, defects are modeled in a supercell geometry. Provided that the defects are sufficiently separated, properties of a single isolated defect can be derived. Then, a general thermodynamic formalism is used to calculate formation energies and ionization energies of intrinsic defects and dopants, and these quantities are applied to identify the type of dopants, compensating native defects, and doping efficiency in semiconductors.

The formation energy of a point defect D in charge state q is defined as:[47]

$$E^f(D^q) = E_{tot}(D^q) - E_{tot}(bulk) - \sum n_i(E_i + \mu_i) + q(E_F + E_v) + E_{corr}(D^q) \quad (1.10)$$

where each term is calculated by density functional theory. $E^{tot}(D^q)$ is the total energy of a supercell with a point defect and $E_{tot}(bulk)$ is the total energy of a reference supercell without a point defect. The third term reflects the reservoirs for atoms that are involved in creating defects: n_i is the number of defect atoms added to or removed from the supercell, E_i is the energy per atom in its elemental phase, and μ_i is the chemical potential. The chemical potential term is strongly dependent on

the experimental conditions under which defects are created (e.g., temperature and partial pressure), however, they are subject to specific boundaries set by the existence of secondary phases. Therefore, the bounds on the chemical potentials are set and the defect formation energies are calculated at two extreme growth conditions. The fourth term is the chemical potential of electrons, which is the Fermi energy, E_F, referenced to the valence-band-maximum, E_v. Lastly, $E_{corr}(D^q)$ is the correction energy arising from the periodic defect-defect interaction due to the finite supercell size. We use the SXDFECTALIGN code to compute $E_{corr}(D^q)$ which calculates the electrostatic interaction between supercells as well as the alignment of the average electrostatic potential in the defect supercell with the bulk.[48]

A schematic diagram of the formation energy of defect as a function of the Fermi energy is shown in Fig. 1.2. Defects in semiconductors and insulators can be in several charge states which introduce charge transition levels in the band gap. The thermodynamic transition level $\epsilon(q_1/q_2)$ is defined as the Fermi energy where the formation energies of charge states q_1 and q_2 are equal:[47]

$$\epsilon(q_1/q_2) = \frac{E^f(D^{q_1}; E_F = 0) - E^f(D^{q_2}; E_F = 0)}{q_1 - q_2} \tag{1.11}$$

where $E^f(D^q; E_F = 0)$ is the formation energy of the defect D in the charge state q where the fermi energy is at the VBM. The thermodynamic transition levels correspond to ionization energies; shallow defects have a transition level positioned near band edges such that the defect is likely to be thermally ionized at room temperature, while deep defects have high ionization energies that are not likely to be ionized at room temperature.

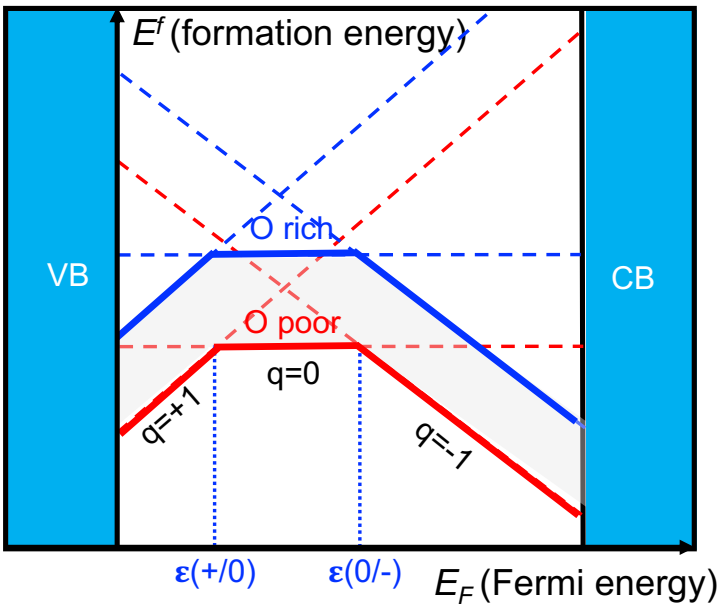

Figure 1.2: Schematic illustration of formation energy vs Fermi level for a defect that can occur in three charge states (q = +1, 0, and -1). The red lines indicate formation energy at oxygen poor environment while the blue lines indicate oxygen rich environment.

1.5 Experimental method

1.5.1 Molecular beam epitaxy

The epitaxial thin film growth techniques are essential part in semiconductor technology because all active devices are produced on these high-quality epitaxial thin films. The epitaxial growth techniques allow fabrication of new materials or new structures (e.g., heterostructures, low-dimensional structures) by using appropriate substrates and growth conditions such as temperature, pressure, and precursors. Especially, the epitaxial techniques have very slow growth rate (1 mono layer per second) that allows precise control of thickness or doping profiles, making them useful in device technology.

Molecular beam epitaxy (MBE) is one of the most important epitaxial growth techniques as almost all semiconductors have been grown by this technique and

demonstrated high purity, high mobility, and good controllability. MBE is an ultra-high vacuum (10^{-8} - 10^{-12} Torr) technique where crucibles containing a variety of source materials are placed in the chamber and the source materials are evaporated upon heating and deposits on a heated substrate. Unlike metal organic chemical vapor deposition (MOCVD) which is another important growth technique widely used in semiconductor technology, MBE typically uses elemental sources and does not involve complex chemical reactions, thus is considered as the simplest and most fundamental epitaxial technique. The low background pressure in MBE allows the use of reflection-high-energy electron diffraction (RHEED) systems for monitoring film growth *in situ*.

As illustrated in Figure 1.3 MBE system typically consists of vacuum pumps (turbo pumps and cryogenic pumps), ionization gauge, effusion cells containing elemental sources and effusion cell shutters, a substrate heater, a pyrometer for measuring the substrate temperature, a substrate rotating holder, a quartz crystal microbalance for measuring elemental fluxes, RHEED gun and fluorescent screen. An electron beam evaporator is sometimes used to evaporate an elemental source.

1.5.2 X-ray Diffraction

X-ray diffraction technique is used for the structural analysis of crystalline materials. The underlying principles of X-ray diffraction is Bragg's law, which relates the angular position of diffracted X-rays to the interplanar spacing of sample:

$$n\lambda = 2d_{hkl}sin\theta_B \tag{1.12}$$

where n is the diffraction order, λ is the wavelength of X-ray beam, d_{hkl} is interplanar spacing, and θ_B is the Bragg angle. Figure 1.4 describes the geometry of a typical diffractometer and the notation used for the angles. Various scan modes are

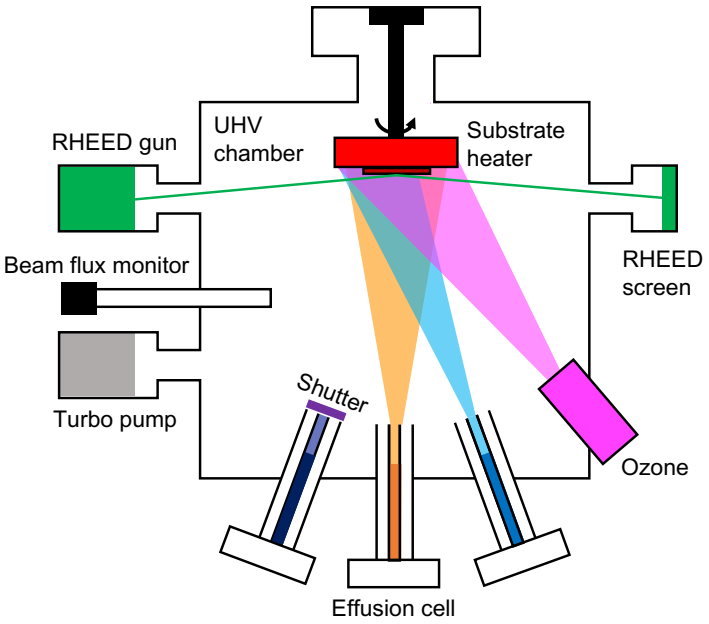

Figure 1.3: Schematic of a molecular beam epitaxy system.

used to obtain the information on the sample such as lattice parameters, degree of crystallinity, film thickness, or grain size.

During the symmetric 2θ-ω scan, the Bragg plane is kept parallel to the surface of the sample, therefore, an interplanar spacing for the planes parallel to the sample surface is obtained from the diffraction peak position, from which the out-of-plane lattice parameter of a thin film can be obtained. On the other hand, during the asymmetric 2θ-ω scan, the sample is tilted along χ axis so that the Bragg plane is no longer parallel with the sample surface. Therefore one can measure an interplanar spacing of different crystallographic directions in the sample, which can be used to calculate the in-plane lattice parameter.

Rocking curve is ω scan at a fixed Bragg angle ($2\theta_B$). A perfect crystal will produce a very sharp peak when the plane normal is parallel to the diffraction vector. However, any defects, dislocations, mosaicity, or substrate curvature create disruptions in the perfect periodicity of atomic planes, which result in broadening of the rocking curve. Therefore, the full-width half-maximum (FWHM) of the rocking curve is generally

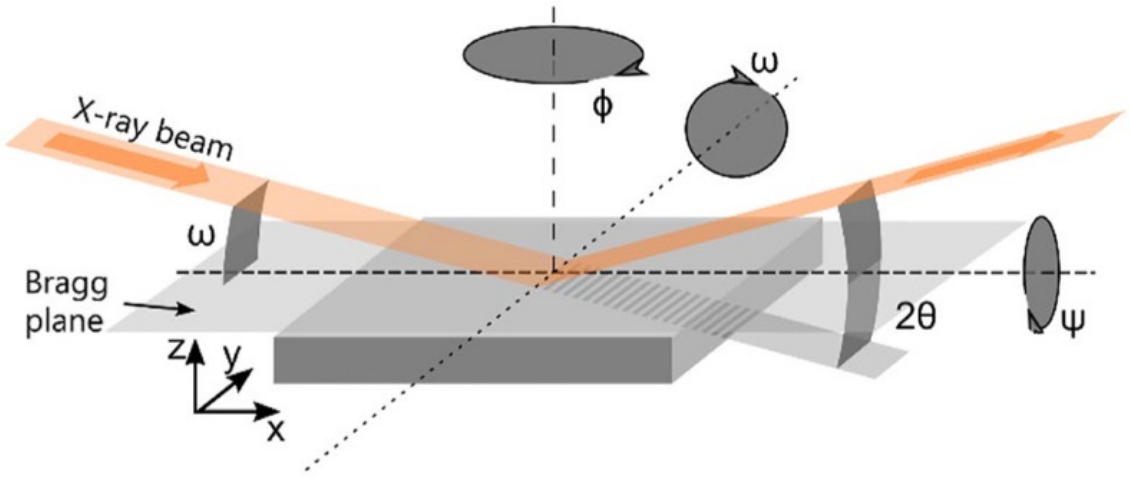

Figure 1.4: The schematic of X-ray diffraction measurement, reprinted with permission from Ref.[2]

used as an indication of the quality of crystals.[2]

X-ray reflectivity can be used to measure the thickness, roughness, and density of thin films. When a X-ray beam is incident on a sample surface at a grazing angle smaller than a critical value (θ_c), the beam undergoes total reflection. Above the critical angle, x-rays penetrate into the film by refraction. If the film and the substrate are made up of different substance, therefore a different electron density, reflection occurs at the interface. The interferenece of individual X-rays reflected each surface or interface results in oscillation pattern in the reflectivity data.[49] Based on the oscillation pattern, the thickness of film can be calculated using the equation:

$$\theta_m^2 = (\frac{\lambda}{2d})^2 m^2 + \theta_c^2 \tag{1.13}$$

where θ_m is the peak position, m is the order of peak, and d is the thickness of the film.

Reciprocal space mapping (RSM) records diffraction intensity distribution by scanning both diffraction angle and sample rotation axes. The shape of reciprocal lattice point determines d spacing variation of films due to strain distribution,

defect, or compositional gradient. The following equation converts reciprocal space coordinates into real space coordinates:

$$Q_x = \frac{1}{\lambda}[cos\omega - cos(2\theta - \omega)] \tag{1.14}$$

$$Q_z = \frac{1}{\lambda}[sin\omega + sin(2\theta - \omega)] \tag{1.15}$$

1.6 Organization of thesis

This dissertation contains computational discovery and experimental synthesis to develop novel UWBG semiconductors that outperforms the state-of-the-art materials. This work is organized into the following three chapters. In Chapter II, we develop a theoretical framework to uncover new ultra-wide-band-gap semiconductors and find the extreme limits to semiconductor band gap. Chapter III showcases rutile GeO_2, an alternative UWBG semiconductor with ambipolar doping, high carrier mobility, and high thermal conductivity. We also demonstrate the first thin film synthesis and single crystal substrates of rutile GeO_2. Finally, Chapter IV gives a summary of this work and provides directions for future work.

CHAPTER II

Computational Discovery of Extreme-band-gap Semiconductors

The magnitude of the band gap is a common criterion to distinguish semiconductors from insulators; semiconductors typically have band gaps narrower than 3 eV, while materials with wider band gaps tend to be insulating. However, ultra-wide-band-gap (UWBG) semiconductors such as AlGaN, diamond, BN and β-Ga_2O_3 challenge this gap-based criterion for materials classification and raise the question of how wide the band gap of a material can be while maintaining shallow dopants and mobile carriers. Here we develop a materials-discovery strategy to identify semiconductors with band gaps wider than AlN (6.2 eV). We discover that materials composed of light elements and crystallized in densely packed structures give rise to a combination of wide band gap ($>$ 7eV) and light effective masses ($<$ 0.7 m_e for electron and $<$ 2 m_e for hole) that enable shallow dopants, high mobility, and weakly bound polarons. We apply the hydrogenic Bohr model, which reproduces experimental shallow-dopant activation energies, to screen for materials with shallow dopants, and we validate the model predictions with atomistic defect calculations. Our work identifies materials with band gaps as wide as 11.6 eV that host shallow dopants and mobile carriers, revealing that there is no intrinsic upper limit to the band gap of semiconductors.

2.1 Background and motivation

In described in Chapter I, light effective mass is the key material parameter that enables semiconducvitiy as light effective mass allows shallow dopant to generate charge carriers, low polaron binding energy to suppress charge localization associated with lattice distortion, and high mobility to effectively conduct carriers under an applied electric field. In general, however, the carrier effective masses increase with increasing band gap, leading to doping inefficiency and carrier localization. Then, a fundamental question arises: (1) What is the true definition of a semiconductor? (2) What are the key structural and chemical material factors that enable electrical conduction in UWBG semiconductors? (3) How wide can the band gap of semiconductor be, and which material is the widest-gap semiconductor?

In this chapter, we address these questions by using first-principles calculation combined with high-throughput data analysis. We surveyed materials, particularly binary compounds having simple crystal structure, and calculated band structure and effective mass using density functional theory. We then investigated the chemical and structural factors that produce materials with ultra-wide-band-gap and semiconductor behavior and developed materials discovery strategy to computationally identify new extreme-gap semiconductors.

2.2 Method

2.2.1 Band structure

We performed first-principles calculations based on hybrid density functional theory using the Vienna Ab initio Simulation Package (VASP).[50,51] We first calculate the crystal structure and electronic band structure of the oxides, nitrides, and carbides listed in Fig. 2.1 using the Heyd-Scuseria-Ernzerhof (HSE06)[52] functional and the projected augmented wave (PAW) method. All structures are fully relaxed using

the quasi-Newton algorithm with a maximum force criterion of 0.01 eV/Å and fully converged cuttoff energy and Brillouin zone sampling grids are used for each material. The amount of Hartree-Fock exchange was adjusted separately for each material between 25 – 35 % to bring its calculated band gap close to the experimental value. Static dielectric constants for all materials are calculated with density functional perturbation theory using the Perdew-Burke-Ernzerhof (PBE) exchange-correlation functional (Fig. 2.2).[53]

2.2.2 Band alignment

To align the calculated band structures for MgO and the BeO polytypes to vacuum, we generated slab structures using the bulk relaxed lattice constants. Non-polar planes of the highest atomic density (lowest surface energy) are exposed to vacuum: (001) for MgO and rs-BeO, (110) for zb-BeO, and (100) for wz-BeO. All slabs consist of 12 layers of atomic planes and a 12 Å-thick vacuum region along the out-of-plane direction. We then calculated the plane-averaged electrostatic potential inside the slab and the vacuum region to align the bulk bands of each material to the vacuum level.[54]

2.2.3 Effective mass

Based on our calculated band structure using HSE06 functional, we obtained the hole and electron effective mass by fitting the valence and conduction bands near the extrema with the hyperbolic equation:

$$E(k) = \frac{\mp 1 \pm \sqrt{1 + (4\alpha\hbar k)/(2m^*)}}{2\alpha} + E_1 \tag{2.1}$$

where $E(k)$ is band energy as a function of crystal momentum k, α is the non-parabolicity fitting parameter, $\hbar$ is the reduced Planck constant, m^* is the electron

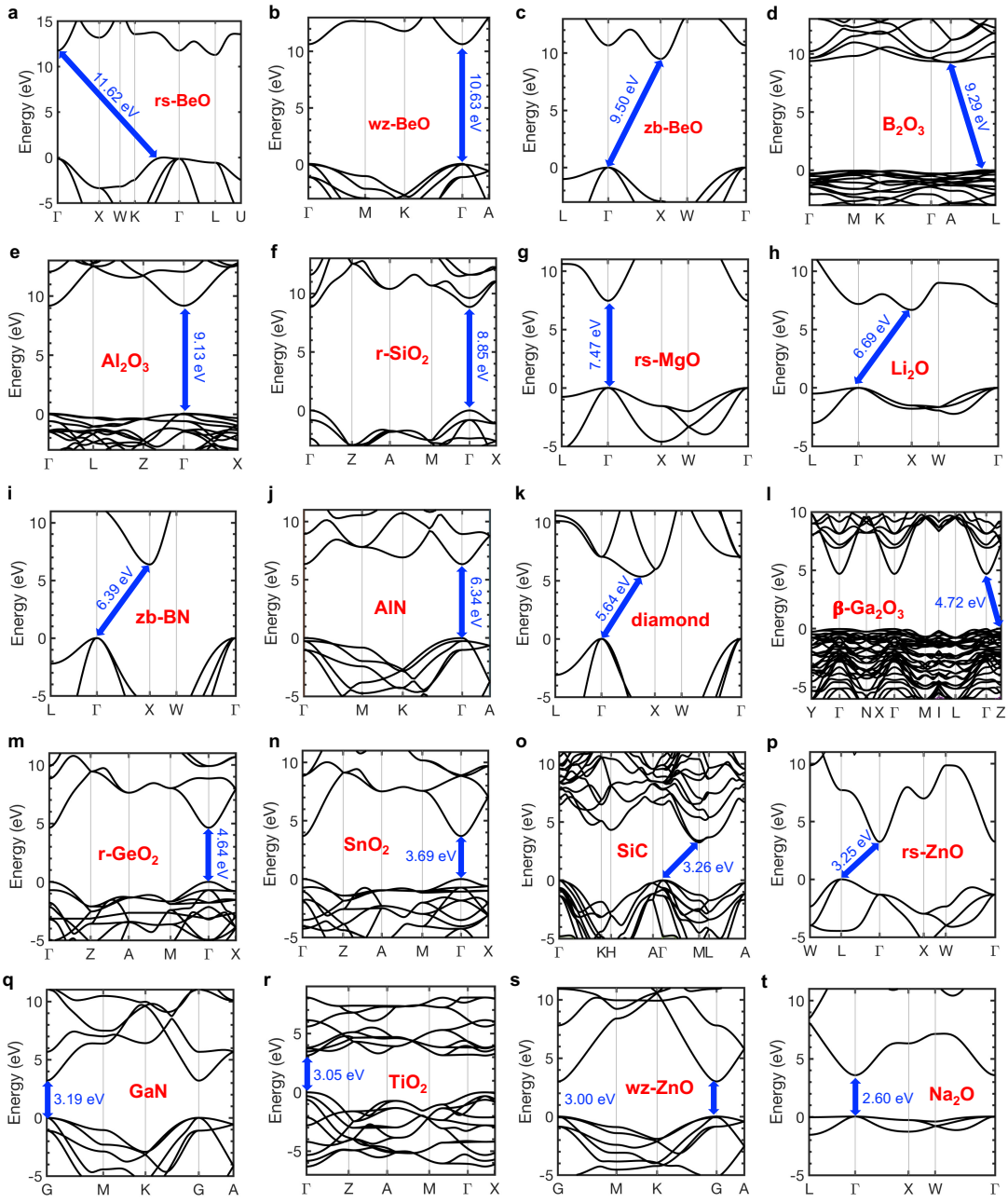

Figure 2.1: The HSE06-calculated band structure of binary oxides, nitrides, and carbides composed of light elements in a simple crystal structure. The plots are ordered in terms of the magnitude of the band gap.

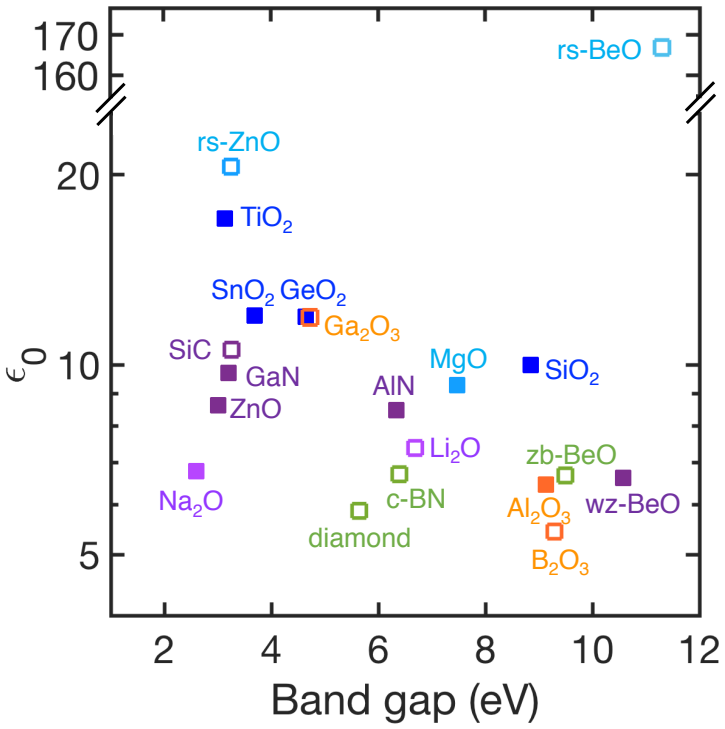

Figure 2.2: The calculated static dielectric constant of binary oxides, nitrides, and carbides as a function of a HSE06-calculated band gap. Dielectric constant generally decreases with increasing band gap.

(–/+) or hole (+/–) effective mass, and E_1 is the VBM (–/+) or CBM (+/–) value. The data for the effective mass is shown in Table 2.1.

2.2.4 Defects and dopants

For the calculation of the formation energy and thermodynamic transition levels of native point defects in r-SiO_2, rs-/zb-/wz-BeO, MgO, and Al_2O_3, we modeled a 72-atom supercell for r-SiO_2, and wz-BeO, a 64-atom supercell for rs-BeO, zb-BeO and MgO, and 120-atom supercell for Al_2O_3. $2 \times 2 \times 2$ centered Brillouin-zone sampling mesh were used for all supercells. In the case for intentional dopants, to predict more accurate value of ionization energies, we used 216-atom supercell for r-SiO_2, rs-BeO, zb-BeO and MgO and 192-atom supercell for wz-BeO and used $2 \times 2 \times 2$ centered Brillouin-zone for all these materials. Using the HSE06 functional[52], we calculated the formation energy of a point defect D in charge state q by using the methodology described in Section 1.3.3. We considered two limits of growth conditions, which are the extreme O-rich/cation-poor and cation-rich/O-poor conditions. We also calculated the formation energy of secondary phases to limit the chemical potentials of the impurities.

2.2.5 Mobility and breakdown field

We performed quasiparticle mobility calculations for zb-BeO and wz-BeO starting from the local density approximation exchange-correlation functional[55] within Quantum ESPRESSO.[56] Phonon frequencies were calculated using density functional perturbation theory on a $6 \times 6 \times 6$ Brillouin-zone (BZ) grid for zb-BeO and on an $8 \times 8 \times 6$ BZ grid for wz-BeO. Quasiparticle energies were calculated with the G0W0 method[57] as implemented in BerkeleyGW[58] using a $6 \times 6 \times 6$ BZ sampling grid for zb-BeO and an $8 \times 8 \times 6$ BZ grid for wz-BeO, a screening plane-wave cutoff energy of 40 Ry, and a summation over unoccupied states up to 20 Ry within the static remain-

Table 2.1: The calculated effective masses of the materials studied

	Electron effective mass (m_e)	Hole effective mass (m_h)
GaN	$m_e^*(\Gamma \to A) = 0.182$ $m_e^*(\Gamma \to M) = 0.151$ $m_e^*(\Gamma \to K) = 0.100$ $m_{e,ave}^* = 0.140$	$m_h^*(\Gamma \to A) = 1.874$ $m_h^*(\Gamma \to M) = 1.508$ $m_h^*(\Gamma \to K) = 0.870$ $m_{h,ave}^* = 1.350$
AlN	$m_e^*(\Gamma \to A) = 0.298$ $m_e^*(\Gamma \to M) = 0.392$ $m_e^*(\Gamma \to K) = 0.303$ $m_{e,ave}^* = 0.328$	$m_h^*(\Gamma \to A) = 0.250$ $m_h^*(\Gamma \to M) = 4.121$ $m_h^*(\Gamma \to K) = 3.539$ $m_{h,ave}^* = 1.539$
wz-BeO	$m_e^*(\Gamma \to A) = 0.521$ $m_e^*(\Gamma \to M) = 0.781$ $m_e^*(\Gamma \to K) = 0.609$ $m_{e,ave}^* = 0.628$	$m_h^*(\Gamma \to A) = 0.362$ $m_h^*(\Gamma \to M) = 3.543$ $m_h^*(\Gamma \to K) = 2.776$ $m_{h,ave}^* = 1.526$
wz-ZnO	$m_e^*(\Gamma \to A) = 0.252$ $m_e^*(\Gamma \to M) = 0.334$ $m_e^*(\Gamma \to K) = 0.251$ $m_{e,ave}^* = 0.276$	$m_h^*(\Gamma \to A) = 2.628$ $m_h^*(\Gamma \to M) = 2.994$ $m_h^*(\Gamma \to K) = 2.229$ $m_{h,ave}^* = 2.598$
SiC	$m_e^*(M \to L) = 0.291$ $m_e^*(M \to \Gamma) = 0.520$ $m_{e,ave}^* = 0.353$	$m_h^*(\Gamma \to A) = 1.473$ $m_h^*(\Gamma \to M) = 2.825$ $m_h^*(\Gamma \to K) = 1.650$ $m_{h,ave}^* = 1.901$
r-SiO_2	$m_e^*(\Gamma \to Z) = 0.367$ $m_e^*(\Gamma \to X) = 0.488$ $m_{e,ave}^* = 0.444$	$m_h^*(\Gamma \to Z) = 1.574$ $m_h^*(\Gamma \to X) = 1.047$ $m_{h,ave}^* = 1.199$
r-GeO_2	$m_e^*(\Gamma \to Z) = 0.234$ $m_e^*(\Gamma \to X) = 0.307$ $m_{e,ave}^* = 0.280$	$m_h^*(\Gamma \to Z) = 1.565$ $m_h^*(\Gamma \to X) = 1.091$ $m_{h,ave}^* = 1.230$
SnO_2	$m_e^*(\Gamma \to Z) = 0.212$ $m_e^*(\Gamma \to X) = 0.264$ $m_{e,ave}^* = 0.245$	$m_h^*(\Gamma \to Z) = 1.577$ $m_h^*(\Gamma \to X) = 1.194$ $m_{h,ave}^* = 1.310$
r-TiO_2	$m_e^*(\Gamma \to Z) = 0.537$ $m_e^*(\Gamma \to X) = 1.076$ $m_{e,ave}^* = 0.853$	$m_h^*(\Gamma \to Z) = 3.290$ $m_h^*(\Gamma \to X) = 2.389$ $m_{h,ave}^* = 2.658$

zb-BN	$m_e^*(X \to \Gamma) = 0.808$ $m_e^*(X \to W) = 0.279$ $m_{e,ave}^* = 0.398$	$m_{hh}^*(\Gamma \to L) = 1.144$ $m_{hh}^*(\Gamma \to X) = 0.484$ $m_{hh}^*(\Gamma \to W) = 1.558$ $m_{hh,ave}^* = 0.952$ $m_{lh}^*(\Gamma \to L) = 1.144$ $m_{lh}^*(\Gamma \to X) = 0.484$ $m_{lh}^*(\Gamma \to W) = 0.484$ $m_{lh,ave}^* = 0.645$ $m_{soh}^*(\Gamma \to L) = 0.220$ $m_{soh}^*(\Gamma \to X) = 0.462$ $m_{soh}^*(\Gamma \to W) = 0.302$ $m_{soh,ave}^* = 0.304$ $m_{h,ave}^* = 0.634$
diamond	$m_e^*(X \to \Gamma) = 1.645$ $m_e^*(X \to X) = 1.384$ $m_{e,ave}^* = 1.466$	$m_{hh}^*(\Gamma \to L) = 0.656$ $m_{hh}^*(\Gamma \to X) = 0.472$ $m_{hh}^*(\Gamma \to W) = 1.075$ $m_{hh,ave}^* = 0.693$ $m_{lh}^*(\Gamma \to L) = 0.656$ $m_{lh}^*(\Gamma \to X) = 0.282$ $m_{lh}^*(\Gamma \to W) = 0.283$ $m_{lh,ave}^* = 0.374$ $m_{soh}^*(\Gamma \to L) = 0.163$ $m_{soh}^*(\Gamma \to X) = 0.282$ $m_{soh}^*(\Gamma \to W) = 0.211$ $m_{soh,ave}^* = 0.213$ $m_{h,ave}^* = 0.427$
zb-BeO	$m_e^*(X \to \Gamma) = 0.674$ $m_e^*(X \to X) = 0.379$ $m_{e,ave}^* = 0.459$	$m_{hh}^*(\Gamma \to L) = 3.119$ $m_{hh}^*(\Gamma \to X) = 1.172$ $m_{hh}^*(\Gamma \to W) = 3.223$ $m_{hh,ave}^* = 2.275$ $m_{lh}^*(\Gamma \to L) = 2.808$ $m_{lh}^*(\Gamma \to X) = 1.170$ $m_{lh}^*(\Gamma \to W) = 1.171$ $m_{lh,ave}^* = 1.567$ $m_{soh}^*(\Gamma \to L) = 2.806$ $m_{soh}^*(\Gamma \to X) = 0.543$ $m_{soh}^*(\Gamma \to W) = 0.419$ $m_{soh,ave}^* = 0.861$ $m_{h,ave}^* = 1.568$

rs-BeO	$m_e^*(\Gamma \to L) = 0.595$ $m_e^*(\Gamma \to X) = 0.606$ $m_e^*(\Gamma \to W) = 0.602$ $m_{e,ave}^* = 0.601$	$m_{hh}^*(VBM \to K/\Gamma) = 2.172$ $m_{hh}^*(VBM \to P) = 0.375$ $m_{hh,ave}^* = 0.673$
MgO	$m_e^*(\Gamma \to L) = 0.358$ $m_e^*(\Gamma \to X) = 0.358$ $m_e^*(\Gamma \to W) = 0.357$ $m_{e,ave}^* = 0.358$	$m_{hh}^*(\Gamma \to L) = 3.155$ $m_{hh}^*(\Gamma \to X) = 1.852$ $m_{hh}^*(\Gamma \to W) = 3.220$ $m_{hh,ave}^* = 2.660$ $m_{lh}^*(\Gamma \to L) = 3.157$ $m_{lh}^*(\Gamma \to X) = 1.867$ $m_{lh}^*(\Gamma \to W) = 1.872$ $m_{lh,ave}^* = 2.226$ $m_{soh}^*(\Gamma \to L) = 0.346$ $m_{soh}^*(\Gamma \to X) = 0.408$ $m_{soh}^*(\Gamma \to W) = 0.372$ $m_{soh,ave}^* = 0.374$ $m_{h,ave}^* = 1.753$
rs-ZnO	$m_e^*(\Gamma \to L) = 0.237$ $m_e^*(\Gamma \to X) = 0.238$ $m_e^*(\Gamma \to W) = 0.237$ $m_{e,ave}^* = 0.238$	$m_{hh}^*(L \to \Gamma) = 2.102$ $m_{hh}^*(L \to W) = 1.258$ $m_{hh,ave}^* = 1.493$ $m_{lh}^*(L \to \Gamma) = 2.091$ $m_{lh}^*(L \to W) = 0.349$ $m_{lh,ave}^* = 0.634$ $m_{h,ave}^* = 1.063$
Na_2O	$m_e^*(\Gamma \to L) = 0.368$ $m_e^*(\Gamma \to X) = 0.368$ $m_e^*(\Gamma \to W) = 0.368$ $m_{e,ave}^* = 0.368$	flat band

Li_2O	$m_e^*(X \to \Gamma) = 0.770$ $m_e^*(X \to W) = 0.421$ $m_{e,ave}^* = 0.515$	$m_{hh}^*(\Gamma \to L) = 3.882$ $m_{hh}^*(\Gamma \to X) = 1.676$ $m_{hh}^*(\Gamma \to W) = 4.680$ $m_{hh,ave}^* = 3.123$ $m_{lh}^*(\Gamma \to L) = 3.884$ $m_{lh}^*(\Gamma \to X) = 1.671$ $m_{lh}^*(\Gamma \to W) = 1.670$ $m_{lh,ave}^* = 2.213$ $m_{soh}^*(\Gamma \to L) = 0.559$ $m_{soh}^*(\Gamma \to X) = 0.910$ $m_{soh}^*(\Gamma \to W) = 0.674$ $m_{soh,ave}^* = 0.700$ $m_{h,ave}^* = 2.012$
B_2O_3	$m_e^*(A \to \Gamma) = 1.694$ $m_e^*(A \to L) = 2.174$ $m_{e,ave}^* = 2.001$	flat band
Al_2O_3	$m_e^*(\Gamma \to L) = 0.378$ $m_e^*(\Gamma \to Z) = 0.408$ $m_e^*(\Gamma \to X) = 0.376$ $m_{e,ave}^* = 0.387$	$m_h^*(\Gamma \to L) = 3.683$ $m_h^*(\Gamma \to Z) = 0.316$ $m_h^*(\Gamma \to X) = 4.876$ $m_{h,ave}^* = 1.782$
β-Ga_2O_3	$m_e^*(\Gamma \to Y) = 0.280$ $m_e^*(\Gamma \to Z) = 0.271$ $m_e^*(\Gamma \to L) = 0.277$ $m_{e,ave}^* = 0.276$	flat band

der approach.[59] Electron-phonon coupling matrix elements were evaluated within the Electron-Phonon-Wannier (EPW)[60] code and interpolated to fine electron and phonon BZ sampling meshes up to 120 × 120 × 120 for zb-BeO and 96 × 96 × 72 for wz-BeO. The phonon-limited electron mobility was evaluated as a function of temperature with the iterative Boltzmann Transport Equation method,[61,62] for states within a 0.5 eV energy window above the conduction band minimum. The imaginary self energy of electrons due to the electron-phonon interaction (i.e., the inverse of the carrier lifetime), Im(Σ), was computed for states within a 0.25 eV energy window above the conduction band minimum.

2.3 Result

2.3.1 Effective mass versus band gap

Based on the band structure and effective mass results Fig. 2.1 and Table 2.1, we analyzed chemical and structural factors of materials that lead to ultrawide band gaps and light carrier masses. First, for wider band gap, materials need to be consisted of lighter elements since the energy difference between adjacent orbitals is larger for lower principal quantum numbers (i.e., electrons closer to nucleus). We therefore focus on carbides, nitrides, and oxides, which happen to be known families of UWBG semiconductors. Among these three families, oxides tend to have wider gaps since O is more electronegative than N or C. Fig. 2.3(a) also shows that the band gap generally increases for compounds with lighter cations (smaller cation radius) and larger ionicity of bonding. Among the materials we studied, we found that the materials having band gaps wider than 7 eV (wider than currently studied UWBG semiconductors such as c-BN or AlN) are oxides of the lightest 2+, 3+, and 4+ cations (2nd and 3rd row in the periodic table) such as Be^{2+}/Mg^{2+}, B^{3+}/Al^{3+} and Si^{4+}.

We next identified materials having small carrier effective mass. Two criteria

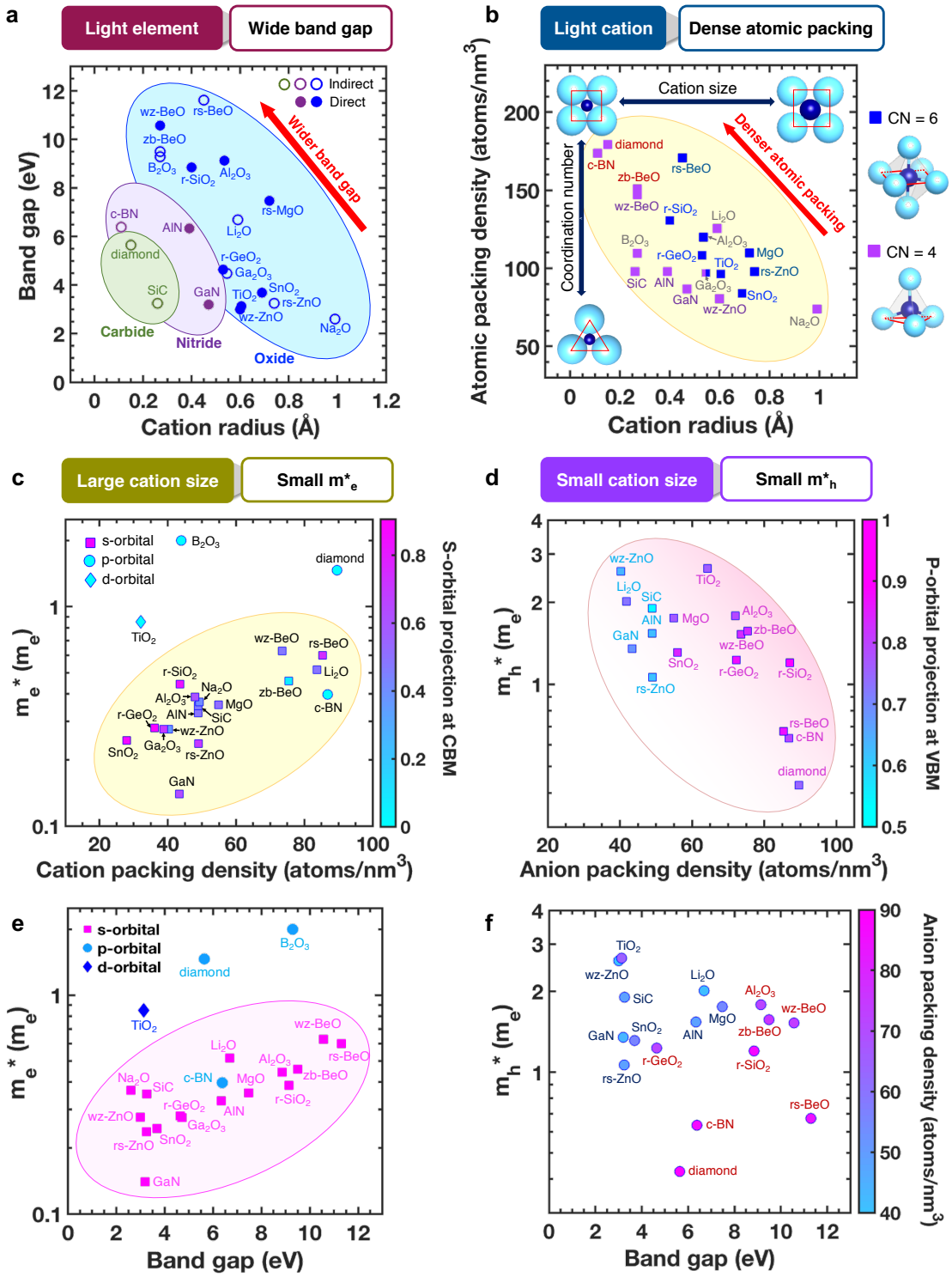

Figure 2.3: Schematic workflow for screening extreme-band-gap materials with light electron and hole effective masses

Figure 2.3: continued from previous page
....(a) The HES06-calculated band gap of binary oxides, nitrides, and carbides as a function of cation radius. Wider band gaps can be achieved for the materials having a smaller (lighter) cation as well as larger ionicity of bonds. (b)Atomic packing density as a function of the constituent cation radius for two different cation coordination environments. Materials have been more densely packed atomic structure when having smaller cation radius or having octahedrally coordinated (CN=6) cations. (c) The HSE06-calculated electron effective mass as a function of cation packing density and the amount of s-orbital characters at conduction band maximum (CBM). Materials generally have small effective mass for larger size of the cation s-orbital which leads to smaller cation packing density. (d) The HSE06-calculated hole effective mass as a function of anion packing density. Hole effective mass generally reduces when the anions are more densely packed and the interaction between the anion 2p-orbitals is maximized, or when the valence bands have a mixed character between the anion 2p-orbitals and the cations s-/d-orbitals. (e) The HSE06-calculated electron effective mass as a function of band gap. Electron effective mass generally increases with increasing the band gap and materials generally have a small effective mass when CBM is consisted of s-orbitals of cations. (f) The HSE06-calculated hole effective mass as a function of band gap and anion packing density. Hole effective mass generally decrease with increasing the anion packing density

are applied: (1) materials consisted of main-group elements (2) materials having dense atomic packing and highly symmetric crystal structure. The conduction band of binary oxides, nitrides, and carbides primarily consists of the lowest unoccupied cation orbital, which is the s orbital for the main group elements (exceptions are the heaviest p-block cations such as Sn^{2+}, Pb^{2+}, Bi^{3+}, etc.) and the d/f orbitals for transition metals/rare earths. However, the d and f orbitals are strongly localized near the nucleus and give rise to flat bands with heavy effective masses, while the directional p orbitals similarly yield poor overlap and heavier effective masses along the direction perpendicular to their lobes. We therefore exclude transition metals, rare earths, and heavy p-block elements from our investigation. Moreover, we expect that atomically dense and highly symmetric crystal structures with simple cation:anion ratios (e.g., 1:1 or 1:2) yield lighter carrier masses due to the stronger orbital overlap between adjacent atoms and reduced band folding at the Brillouin-zone edges. We thus focus on materials in the zinc blende (zb), rocksalt (rs), wurtzite (wz), and

rutile (r) structures. Fig. 2.3(b) illustrates the atomic packing density for those materials. We find that materials have more densely packed atomic structure when having smaller cations. For similar size of cations, denser atomic packing is achieved when cations have octahedrally coordinated environment (CN = 6).

We then examine the effects of chemistry and crystal structure on the electron and hole effective masses. Fig. 2.3(c) shows the DFT-calculated electron effective mass as a function of cation packing density as well as the amount of s-orbital characters at conduction band maximum (CBM). Most of the main-group oxides/nitrides/carbides with s-orbital CBM character have light electron effective masses (less than 0.7 m_e) that generally decrease with increasing cation s-orbital character of the CBM wave function. Also, the larger cation s-orbitals lead to the larger overlap, yielding smaller effective masses. As the cation packing density becomes smaller for larger size of cations, electron effective masses decrease with decreasing cation packing density.

On the other hand, the valence band primarily consists of the more localized anion 2p orbitals, which give rise to heavier effective masses for holes than electrons. However, we find that the hole effective mass decreases with increasing anion packing density and, correspondingly, stronger overlap between 2p orbitals on adjacent anion atoms (Fig. 2.3(d)). The exception is when the valence bands have a mixed character of cation s-/d-orbitals: these materials tend to have smaller hole effective masses at a given anion packing density. Therefore, denser anion packing is the key for the light effective mass, which can be achieved for smaller cation since smaller cation radii decrease the distance between neighboring anions as well as for crystal structures with octahedrally coordinated cations (rocksalt and rutile) rather than tetrahedrally coordinated structures (wurtzite and zincblende).

Finally, in order to identify materials having wide band gap as well as small effective masses, we plotted electron/hole effective masses as a function of band gaps in Fig. 2.3(e-f). We find that the electron mass generally increases with the increasing

band gaps. However, since the materials having s-orbital characters at CBM have relatively light electron effective masses, oxides of the lightest main-group cations such as BeO polytypes, MgO, B_2O_3, Al_2O_3, and r-SiO_2 have band gaps wider than 7 eV and electron effective masses less than 0.7 m_e. On the other hand, materials with dense anion packing have relatively light hole effective masses ($< 2\ m_e$) despite wide band gaps (> 7 eV), and the materials that fall into this criterion are r-SiO_2, MgO, Al_2O_3, and BeO polytypes.

2.3.2 Ionization energy predicted by the Bohr model

Next, we apply the Bohr model, which treats the dopant-bound carriers as hydrogenic atoms, to evaluate the dopant ionization energies. Although the Bohr-model predictions may fail for strongly bound carriers, which experience a local potential that deviates from the screened Coulomb form and may also form polarons (i.e., the model may predict some false positives), shallow dopants are well described by the model and will be identified in our search (no false negatives). Combining the Bohr model with the DFT-calculated effective masses (Table 2.1) and static dielectric constants (Fig. 2.2), we estimate the donor and acceptor ionization energies of the investigated materials as a function of their band gap and reproduce the data for known semiconductors in good agreement with experiment (Fig. 2.4(c)).

Donor ionization energies generally increase with the band gap (Figure 2.4(a)). Our algorithm recovers established n-type semiconductors such as GaN, SiC, AlN, wz-ZnO, TiO_2, SnO_2, and β-Ga_2O_3. In addition, we identified several less explored materials such as rs-ZnO, r-GeO_2, rs-MgO, Al_2O_3, r-SiO_2, and BeO polytypes, all of which are predicted to host shallow donors (ionization energy less than 0.21 eV). Ga-doped rs-ZnO is known to exhibit high conductivity under high pressure,[63] while r-GeO_2 is predicted to be n-type dopable with Sb, As, and F dopants by hybrid density functional theory,[64] further validating the accuracy of our model.

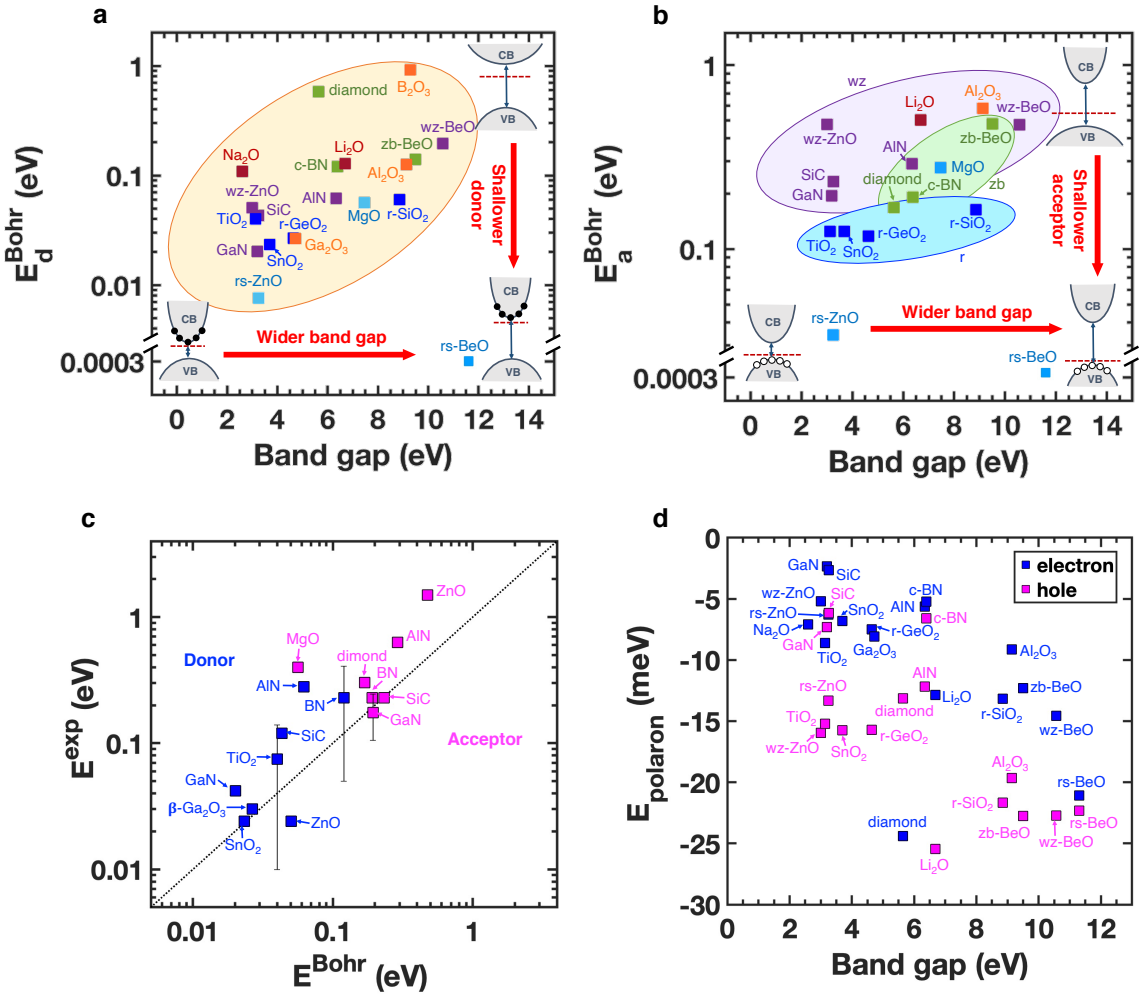

Figure 2.4: Ionization energies predicted by the Bohr model (a-b) The donor (E_d^{Bohr}) and acceptor (E_a^{Bohr}) ionization energies evaluated with the Bohr model for wide-band-gap materials as a function of the band gap. The model identifies several extreme-band-gap materials with shallow dopants such as MgO, r-SiO_2, and rs-BeO that have not been explored as semiconductors. (c) The correlation between the donor and acceptor ionization energies predicted by Bohr model (E^{Bohr}) and the donor and acceptor ionization energies determined by experiment (E^{exp}). The experimental values for donor ionization energies are adopted from ref: GaN,[3] AlN,[4] SiC,[5] wz-ZnO,[6] SnO_2,[7] TiO_2,[8,9] zb-BN,[10] and Ga_2O_3.[11] The experimental values for acceptor ionization energies are adopted from the ref: GaN,[3] AlN,[4] SiC,[5] wz-ZnO,[12] zb-BN,[10] diamond,[13] and rs-MgO.[14] (d) Polaron binding energies predicted by the equation in ref:[15]

The acceptor ionization energies (Fig. 2.4(b)) are generally higher than donors due to the heavier hole effective masses and increase with increasing band gap. However, we found an outlying trend for the rutile binary oxides; their acceptor ionization energies remain approximately constant with increasing band gap. This is because their lattice constant decreases and the oxygen density increases with increasing band gap, leading to easier hole hopping and lighter hole effective mass. Particularly, r-SiO_2 has an extreme band gap (8.85 eV) but a lower predicted acceptor ionization energy than diamond or c-BN, which are known p-type materials. rs-BeO also emerges as a candidate extreme-band-gap material with exceptionally shallow dopants of both types, due to its unusually high dielectric constant ($\epsilon_0 = 167$).

2.3.3 Polaron binding energy

Next, we performed atomistic defect calculation for the extreme-band-gap materials predicted by the Bohr model to host shallow dopants to identify dopant impurities and their atomic configuration. Specifically, although substitutional impurity atoms may act as shallow dopants at the undistorted site, their incorporation into the lattice could be accompanied by large distortions off the substitutional site, also known as polaronic effects, that may increase the ionization energy. For example, acceptor impurities in wide-band-gap oxides can cause formation of trapped hole polarons that inhibits p-type doping.[65] Moreover, these distortions may favor the capture of an additional electron or hole, which would convert the dopants into compensators, such as the deep DX-centers that limit n-type doping in AlGaN.[66] Our atomistic calculations determine accurate ionization energies of dopants by explicitly calculating distorted atomic configurations and their relative stability compared to the undistorted substitution. We performed explicit defect calculation for the extreme-band-gap (> 7 eV) materials with the Bohr ionization energy less than 0.2 eV, i.e., MgO, r-SiO_2, Al_2O_3, and BeO polytypes for n-type material and MgO, r-SiO_2, and rs-BeO for

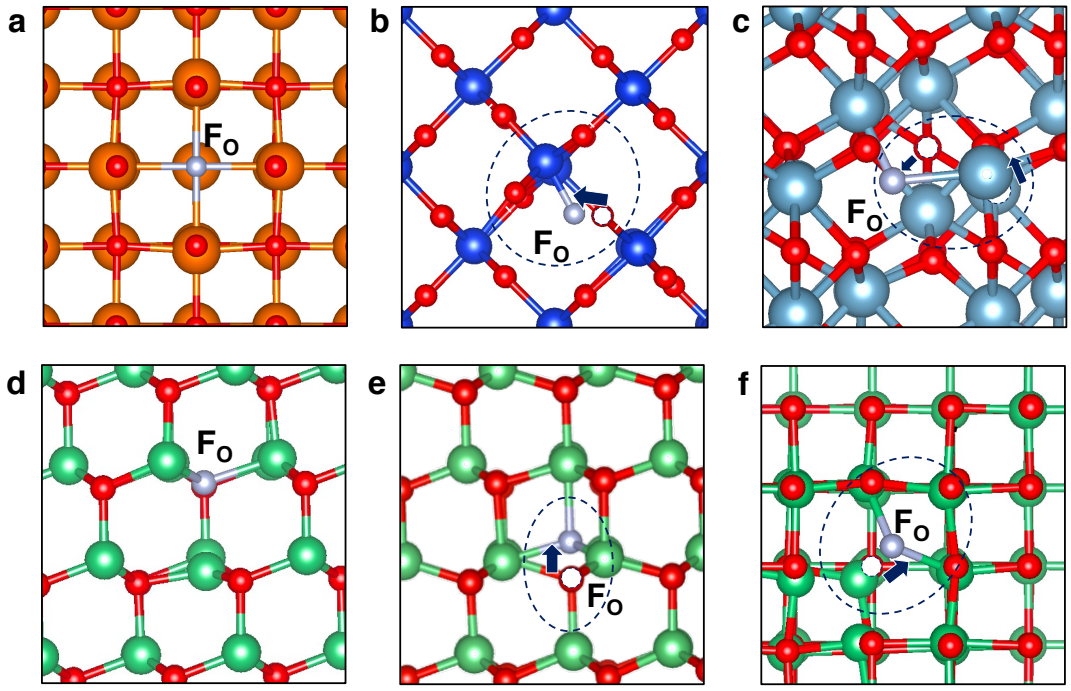

Figure 2.5: The configuration of F_O in (a) MgO, (b) r-SiO_2, (c) Al_2O_3, (d) zb-BeO, (e) wz-BeO, and (f) rs-BeO

p-type material.

We find that the energetic preference for polaron formation depends both on the host materials as well as the type of impurity atom. We predict donor defects tend to form DX centers in r-SiO_2, Al_2O_3, wz-BeO, and rs-BeO (Fig. 2.5(b,c,e,f)). On the other hand, the formation of DX center in zb-BeO depends on the type of dopant: F_O does not form DX center (Fig. 2.5(d)) while B_{Be} donor defect does form DX center in zb-BeO,. We predict the origin of the difference is the lack of third-nearest-neighbor interactions in zb due to its different stacking sequence than wz.[67] In the case of MgO, donor defects such as F_O, Al_{Mg}, and Ga_{Mg} do not form DX center and electron wavefunction at CBM is spatially delocalized (Fig. 2.5(a)).

On the other hand, the AX center is not stable for $Li_{Mg/Be}$ and $Na_{Mg/Be}$ acceptors in MgO and rs-BeO (Fig. 2.6(a-b)). We also predict negligibly small trapping energy (less than 0.025 eV, in Figure 2.4(d)) for holes in MgO and rs-BeO, indicating that

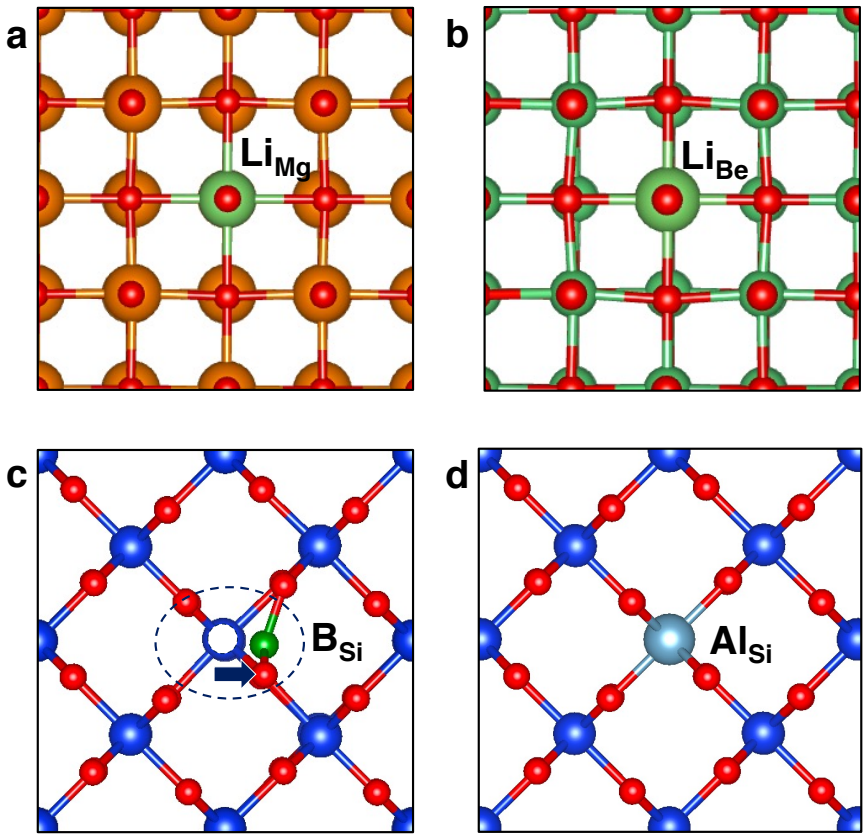

Figure 2.6: The configuration of (a) Li_{Mg} in MgO, (b) Li_{Mg} in rs-BeO, (c) B_{Si} and (d) Al_{Si} in r-SiO_2 in the neutral charge state.

holes are not likely to form self-trapped polarons in MgO and rs-BeO. The AX center is not stable in r-SiO_2 (Fig. 2.6(c-d)), however, both B_{Si} and Al_{Si} are deep acceptors.

2.3.4 Candidate extreme-gap semiconductors

We then calculated the donor and acceptor ionization energies of the impurities that do not favor the formation of DX or AX centers. Overall, we identified rs-MgO a promising ambipolarly dopable material and rs-BeO a promising p-type dopable material. On the other hand, we predict deep ionization energy for F_O donors (0.78 eV) in zb-BeO and Al_{Si} (1.81 eV) acceptors in r-SiO_2.

Rs-MgO has a direct band gap of 7.64 eV but relatively light electron and hole

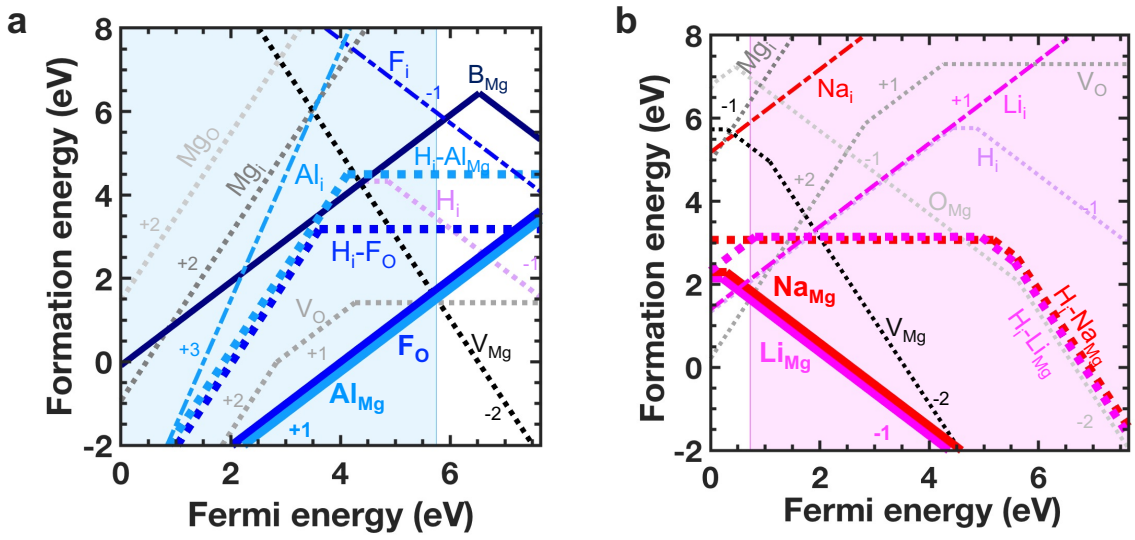

Figure 2.7: (a) Formation energy of donor impurities and intrinsic defects in MgO as a function of the Fermi level under cation-rich/O-poor conditions. F_O and Al_{Mg} are shallow donors with ionization energies less than 0.07 eV. (b) Formation energy of acceptor impurities and intrinsic defects in MgO as a function of the Fermi level under cation-poor/O-rich conditions. Li_{Mg} and Na_{Mg} are shallow acceptors with ionization energy of 0.07 eV and 0.17 eV, respectively.

effective masses (0.358 m_e and 1.841 m_e respectively). Our calculations predict low ionization energies both for donors (F_O and Al_{Mg}) and acceptors (Li_{Mg} and Na_{Mg}); F_O and Al_{Mg} donors are stable in +1 charge state throughout the entire Fermi energy range, while Li_{Mg} and Na_{Mg} have a shallow ionization energy of 0.21 eV (Fig. 2.7). N-type doping of MgO has not been demonstrated, which we attribute to compensation by Mg vacancies and H interstitials. However, p-type conduction in Li-doped MgO single crystals has been demonstrated experimentally,[14,68] despite our prediction of weak compensation by oxygen vacancies and Li interstitials, validating our calculation results. Our calculation results show MgO is a promising ambipolarly dopably material.

Rs-BeO has the widest band gap (11.62 eV) among the three BeO polymorphs. We predict shallow ionization energies for both Li_{Be} (0.07 eV) and Na_{Be} (0.17 eV) in rs-BeO, though there are compensating defects such as O vacancies, H, Be, and

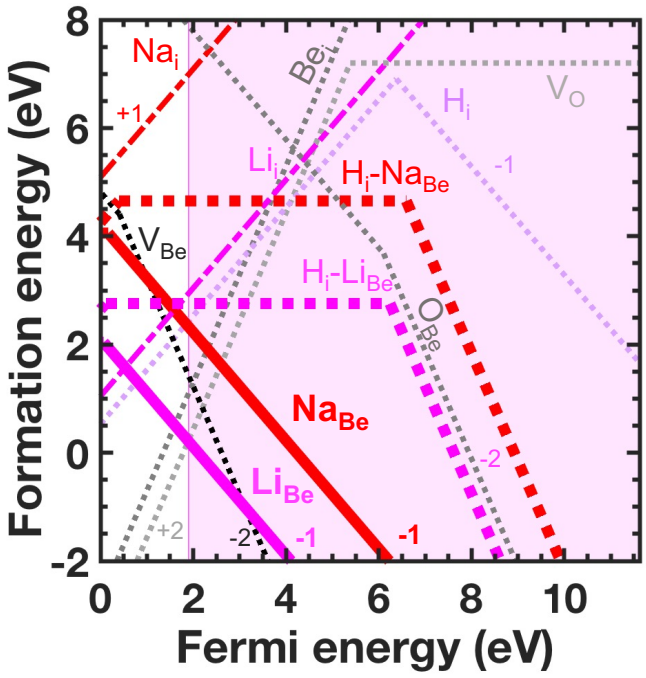

Figure 2.8: Formation energy of acceptor impurities and intrinsic defects in rs-BeO as a function of the Fermi level at Mg-poor/O-rich growth condition. Acceptors in rs-BeO have shallow ionization energy of 0.07 eV for Li and 0.17 eV for Na.

Li interstitials (Fig. 2.8). We attribute the shallower acceptor ionization energies in rs-BeO to its shallow valence bands. In Fig. 2.9 (a), we compared the band alignment of BeO polytypes as well as rocksalt ZnO and MgO. Compared to zb-BeO and wz-BeO, rs-BeO has denser oxygen packing due to octahedral coordination, which leads to higher-lying valence band edge similarly close to rs-MgO or rs-ZnO while acceptor defect level positioned close to each other. Therefore, rs-BeO has shallower acceptor ionization energy despite its extreme band gap.

We also calculated phonon-limited electron and hole mobility of MgO and rs-BeO in Fig. 2.9 (b-c). At 300 K, the calculated electron mobility is 141 cm^2 V^{-1} s^{-1} for MgO and 272 cm^2 V^{-1} s^{-1} for rs-BeO. These are comparable to the state-of-the-art UWBG semiconductors such as β-Ga_2O_3 or AlGaN. The calculated room temperature hole mobility is 17 cm^2 V^{-1} s^{-1} for MgO and 12 cm^2 V^{-1} s^{-1} for rs-BeO, which are relatively small but also comparable to common p-type semiconductors.

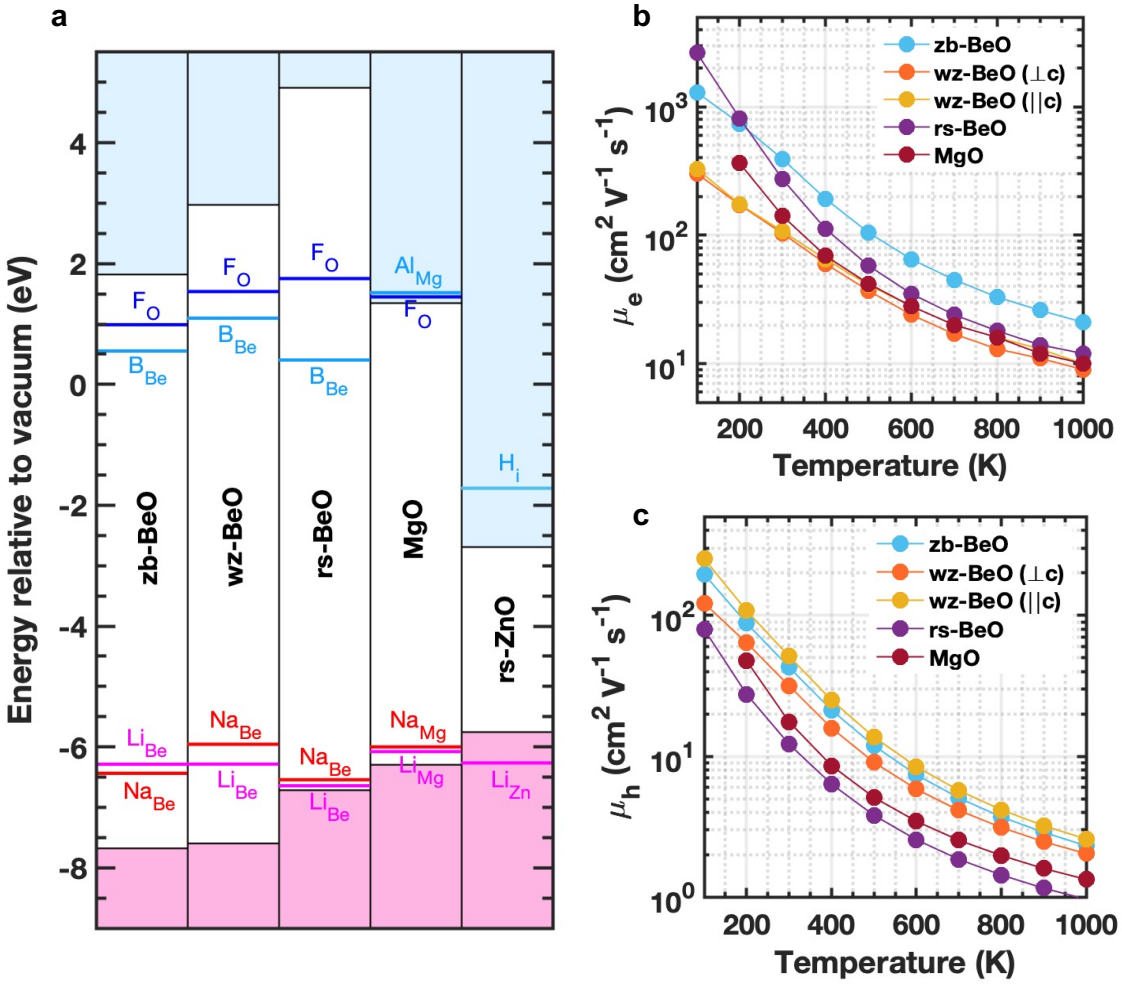

Figure 2.9: Extreme-band-gap materials with shallow dopants and mobile carriers. (a) Absolute band positions relative to vacuum and dopant energy levels of BeO polytypes, MgO, and rocksalt ZnO. Despite its ultra-wide-band-gap (11.62 eV and 7.64 eV), rs-BeO and MgO host shallow dopants. (b) Electron and (c) hole mobility of BeO polytypes and MgO as a function of temperature.

Previous efforts[69],68 to analyze semiconductor dopability focused on dopant compensation by unintentional defects (e.g., vacancies and interstitials) under thermodynamic equilibrium. However, several nonequilibrium techniques have been developed over the years to manipulate the Fermi level during growth and circumvent dopant compensation, such as above-gap illumination,[70] junction-assisted epitaxy,[71] and co-doping with intentional mobile compensators that are subsequently removed by annealing.[72] We therefore argue that the ultimate limitation of semiconductor dopability is dopant ionization, rather than dopant compensation. Thus, combined with the prediction for dopants, polarons, and mobility, we determine MgO and rs-BeO can conduct electrons and/or holes with a carrier source provided by traditional doping.

2.4 Conclusion

In summary, we analyzed the structural and chemical factors that produce materials with ultra-wide-band-gaps and semiconducting behavior. The discovery of shallow dopants and mobile carriers in materials such as rs-MgO and rs-BeO with band gaps as wide as 11.6 eV, i.e. near the upper limit of the band gaps of insulators, addresses a fundamental question in materials science and proves that there is no practical upper bound to the band gap of semiconductors. Our developed theoretical framework for the prediction of dopant activation is validated by direct experimental evidence for a wide range of UWBG semiconductors. The framework can naturally be deployed in a high-throughput fashion to discover new semiconductors that surpass the current state of the art for potentially transformative applications in transparent conductors, power electronics, and UV optoelectronics.

CHAPTER III

Rutile Germanium Oxide: An Alternative Ultra-wide-band-gap Semiconductor

Rutile GeO_2 (r-GeO_2) is a potential ultra-wide-band-gap (UWBG, 4.68 eV) semiconductor, yet is unexplored for electronic applications. By using a combined theoretical and experimental approach, we assessed the important material properties of r-GeO_2 for power electronic applications and its potential to transform the current state-of-the-art materials. Our first-principles calculations predict shallow ionization energies (< 0.04 eV) for donors such Sb_{Ge}, As_{Ge}, and F_O, and an ionization energy of 0.45 eV for AlGe acceptors, suggesting the possibility of ambipolar doping. Theory also predicts a phonon-limited electron mobility of 289 $cm^2\ V^{-1}\ s^{-1}$ and hole mobility of 28 $cm^2\ V^{-1}\ s^{-1}$ at room temperature, further suggesting that r-GeO_2 is a promising ambipolar semiconductor. Due to the highly symmetric crystal structure, r-GeO_2 has thermal conductivity of 51 $W\ m^{-1}\ K^{-1}$, which is experimentally measured for our bulk, polycrystalline sample. Though the thin-film synthesis of r-GeO_2 has remained challenging due to the presence of highly metastable amorphous phase, we demonstrate the first synthesis of single crystalline thin films of r-GeO_2 on a sapphire substrate as well as a TiO_2 substrate using ozone-assisted molecular beam epitaxy. We also showcase the first r-GeO_2 single crystal substrates that can be potentially applied for homoepitaxial film growth. Our work motivates further exploration of

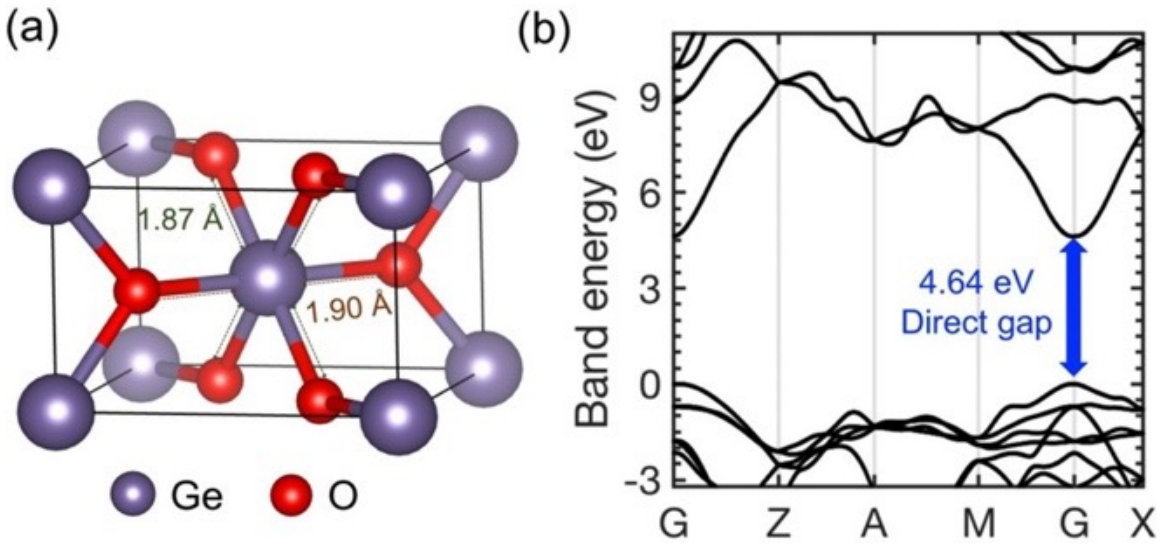

Figure 3.1: (a) Crystal structure of rutile GeO_2. (b) The electronic band structure of rutile GeO_2 calculated with the HSE06 hybrid functional.

r-GeO_2 as an alternative UWBG semiconductor that can overcome the limitations of the current UWBG semiconductor materials.

3.1 Band structure and effective mass

In periodic table, Ge is the group 14 element between Si and Sn, sitting in the fourth period next to Ga. Accordingly, GeO_2 has an ultra-wide-band-gap similar to that of Ga2O3 but adopts chemical and structural properties analogous to SiO_2 or SnO_2. Though both Ga_2O_3 and SnO_2 are established wide-band-gap n-type semiconductors, a little has been known about the semiconducting properties of GeO_2. While SiO_2 is stable in the quartz phase and SnO_2 is stable in the rutile phase, both quartz and rutile are deeply stable polymorphs of GeO_2 under ambient condition. Among them, the rutile phase is the high-density phase with octahedral coordination and chemically resistant when exposed to solvents (especially, insoluble in water)[73], thus is better suited for device application.

Fig. 3.1 (a) and (b) shows the crystal structure and band structure of r-GeO_2 calculated by HSE06 hybrid density functional theory. By applying 35% mixing of

Hartree-Fock exchange, we calculate the fundamental band gap of 4.64 eV at Γ, which is close to the experimentally measured band gap (4.68 eV)[74] and the band gap calculated by G_0W_0 method (4.44 eV)[75]. Despite its ultra-wide-band-gap, r-GeO_2 exhibits relatively light electron and hole effective masses. The effective mass is obtained by fitting the hyperbolic equation to the HSE06 band structure. The electron effective mass along $\Gamma \rightarrow Z$ and $\Gamma \rightarrow X$ direction is 0.234 m_e and 0.307 m_e, and the density of states effective mass of electron (calculated by the geometric mean) is 0.280 m_e. The values are similar to common n-type semiconductors such as β-Ga_2O_3 (0.23 – 0.34 m_e)[76], SnO_2 (0.23 – 0.34 m_e)[77], and GaN (0.19 – 0.21 m_e)[78]. The small electron effective mass of r-GeO_2 is attributed to the broad conduction bands consisted of delocalized Ge 4s orbitals.

On the other hand, the hole effective mass of r-GeO_2 is 1.091 m_e along $\Gamma \rightarrow X$ and 1.565 m_e along $\Gamma \rightarrow Z$ direction, and the density of states effective mass of hole is 1.230 m_e. The values are notably small compared to other wide-band-gap oxide semiconductors such as β-Ga_2O_3 which has a flat valence band giving rise to trapped hole polarons[65,79] but are close to p-type dopable semiconductors such as GaN (1.69 – 1.76 m_e for heavy holes).[80] Though the valence bands of r-GeO_2 consist of localized O 2p orbitals, the rutile structure has a close-packed oxygen structure which allow holes to conduct easily through oxygen orbitals, therefore, promising hole-transport property is also expected for r-GeO_2.

The combination of the ultra-wide-band-gap and the delocalized nature of electrons and holes makes r-GeO_2 a promising UWBG semiconductor with ambipolar dopability, however, the semiconductor properties of r-GeO_2 is largely unexplored. In addition, thin-film growth of single-crystalline r-GeO_2 has been not reported until recently, which has challenged the study of r-GeO_2 for electronic applications. In this work, we applied first-principles calculations and experimental techniques to characterize the fundamental material properties of r-GeO_2 such as dopability, mobility,

and thermal conductivity and assess its potential for power electronic application by comparing the Baliga figure of merit of r-GeO_2 with the current state-of-the-art materials. We also demonstrate the first thin film synthesis and substrate synthesis of single crystalline r-GeO_2 which opens the possibility to realize r-GeO_2-based electronics.

3.2 Donors and acceptors

3.2.1 Calculation method

To identify potential donors and acceptors in r-GeO_2, we apply hybrid density functional theory and the modern defect calculation methodology to calculate the formation energy of a point defects as a function of the Fermi level.28 We use the project augmented wave (PAW) method and the Heyd-Scuseria-Ernzerhof (HSE06)[52] functional with 35% mixing of Hartree-Fock exchange as implemented in the Vienna Ab initio Simulation Package (VASP)[50,51]. The employed pseudopotentials for Ge and O are the GW-compatible pseudopotentials with a plane-wave cutoff energy of 400 eV. We modeled point defects and impurities using 72-atom supercells and a 2 × 2 × 2 centered mesh of k-points sampling. All bulk and defect structures are relaxed using the quasi-Newton algorithm with a maximum force criterion of 0.01 eV/Å. For defect-formation energy calculation, we calculate the correction energy for the unphysical electrostatic interaction between the periodic image charges introduced by supercell approximation using the SXDEFECTALIGN[48] code and we apply the static dielectric constant of the host material to $\epsilon_0 = 13.28$. We calculate the chemical potential at the two limits of growth environments: extreme O-rich/Ge-poor [$\mu_O = 0$ eV and $\mu_{Ge} = \Delta H_f(GeO_2)$, where $\Delta H_f(GeO_2)$ = -5.49 eV/formula unit] and extreme O-poor/Ge-rich [$\mu_O = \Delta H_f$(GeO2) and $\mu_{Ge} = 0$ eV] conditions and the chemical potentials of the impurity species are limited by the formation of secondary phases such as Al_2O_3,

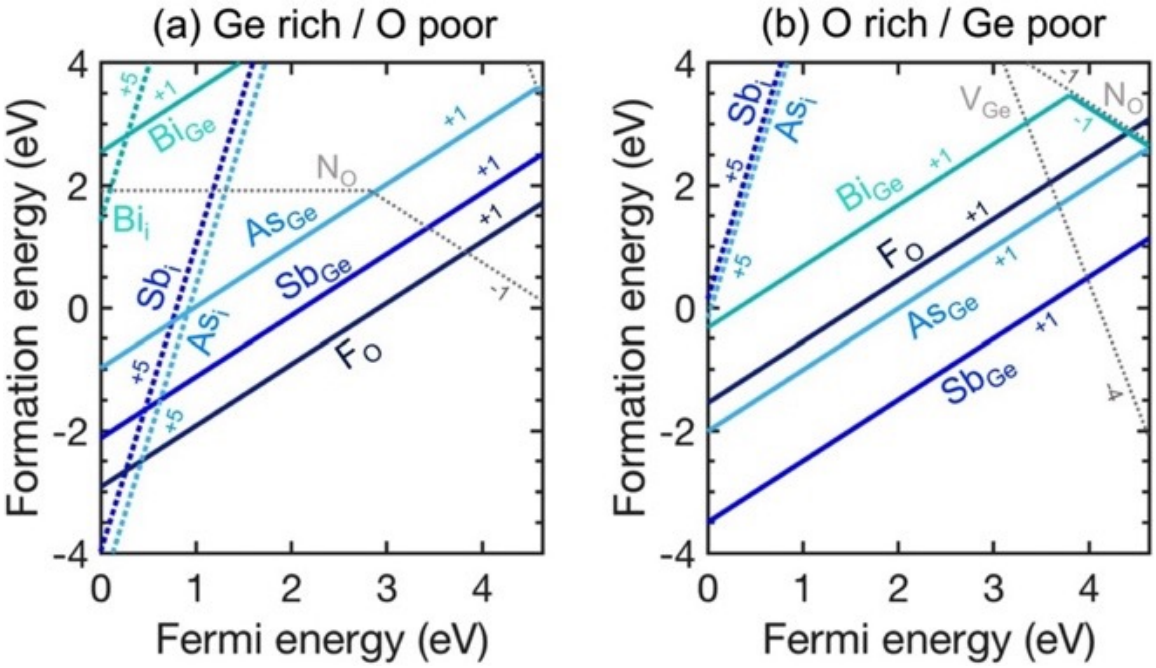

Figure 3.2: Formation energy of donor defects and potential charge-compensating native defects as a function of the Fermi level in the limit of (a) Ge rich/O poor and (b) O rich/Ge poor conditions.

Ga_2O_3, In_2O_3, Sb_2O_3, As_2O_5, and GeF_4. We perform spin-polarized calculations for supercells with odd numbers of electrons and consider spin-orbit coupling for Bi defect.

3.2.2 Donors

In Fig. 3.2, we calculate the formation energy of donor defects as a function of the Fermi level along with potential charge-compensating native defects. The calculated donor defects are group-15 elements substituting the Ge site such as Sb_{Ge}, As_{Ge}, and Bi_{Ge}, and F dopant substituting the O site (F_O). All the investigated dopants, except for Bi, are shallow donors with an ionization energy less than 0.04 eV, suggesting promising n-type dopability of r-GeO_2. The formation energies of donors vary depending on the growth conditions: F_O forms more easily under O-poor conditions, whereas Sb_{Ge} and As_{Ge} form more easily under O-rich conditions. We predict that possible sources of donor compensation are N_O (a deep acceptor with an

acceptor ionization energy of 3.03 eV) under O-poor conditions and V_{Ge} (a shallow acceptor) under O-rich conditions. Therefore, Ge rich/O poor conditions are required with the absence of nitrogen impurity to avoid the charge compensation of both V_{Ge} and N_O and enhance doping efficiency.

3.2.3 Acceptors

We then investigated group-13 elements (Al, Ga, and In) substituting the Ge site for acceptor defects in GeO_2 (Fig. 3.3). In order to calculate the formation of localized hole polarons which inhibits p-type doping in many oxides such as SnO_2 and β-Ga_2O_3,[65] we performed the structural optimization of acceptor defects by intentionally displacing an oxygen atom next to an acceptor defect from its symmetric position. We find that in the neutral charge state, all the acceptor defects prefer to form a hole polaron, which is localized on an oxygen atom next to the dopant accompanied by a local lattice distortion. As a result, the energy difference of the localized and delocalized hole state, i.e., the self-trapping energy of polaron (EST), is required to create free holes, which we calculate is 0.45 eV for Al_{Ge}, 0.54 eV for Ga_{Ge}, and 0.48 eV for In_{Ge}, and it corresponds to the 0/-1 ionization energy. The competing energy for the formation of a hole polaron is the strain energy (ES), which is calculated from the energy difference between the atomic configuration corresponding to the delocalized hole and the atomic configuration corresponding to the localized hole, both in the charge-neutral state.

Among the acceptor defects, we suggest Al_{Ge} is the most promising p-dopant candidate in r-GeO_2 as it has lower formation energy and ionization energy compared to Ga_{Ge} and In_{Ge} (Fig. 3.3). Though 0.45 eV acceptor ionization energy of Al_{Ge} is relatively high, we expect that hole conduction can be achieved by impurity-band formation at acceptor concentrations exceeding the Mott-transition limit. We estimate the critical Mott density (n_c) for Al acceptors to be 2.07×10^{20} cm^{-3} by using

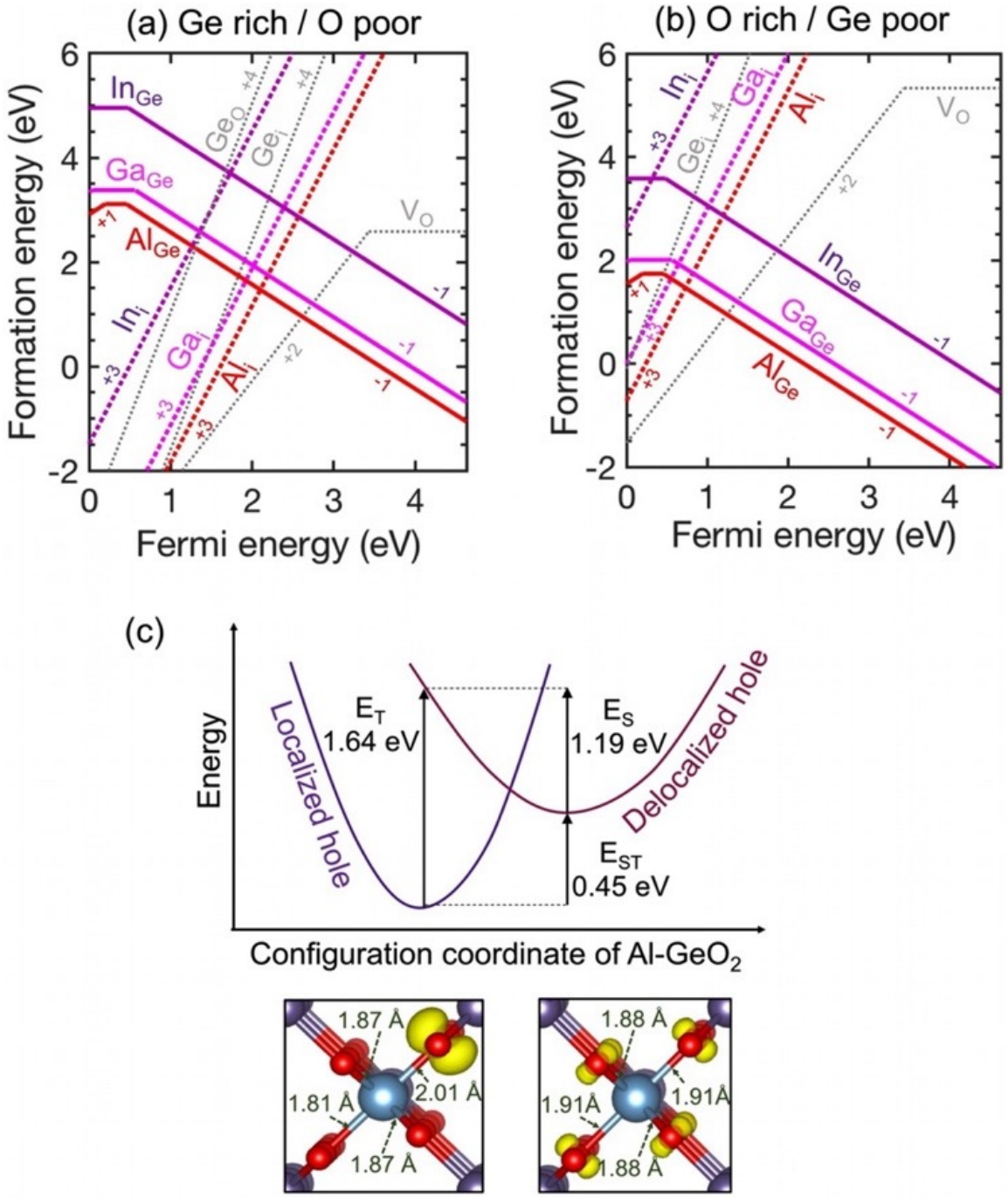

Figure 3.3: (a-b) Formation energy of acceptor defects and potential charge compensating intrinsic defects as a function of the Fermi level in the limit of (a) Ge rich/O poor and (b) O rich/Ge poor conditions. (c) Configuration coordinate diagram for the formation of localized hole polarons in Al-doped r-GeO_2. ET, EST, and ES indicate the vertical excitation energy, the polaron self-trapping energy, and the strain energy, respectively. The insets show the isosurface of the band-decomposed charge density at the VBM for the localized and the delocalized holes near an Al_{Ge} dopant.

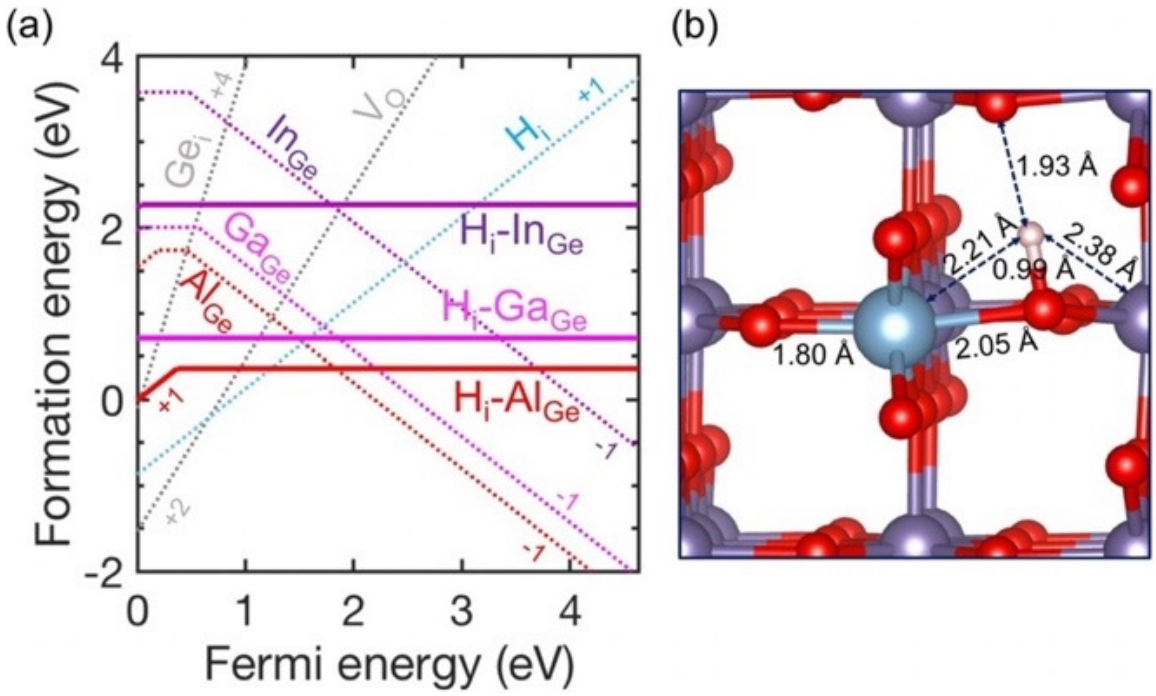

Figure 3.4: (a) Formation energy of H_i-acceptor defect complexes as a function of the Fermi level along with H_i, acceptors, and potential charge compensating defects in the limit of Ge poor/O rich condition. (b) The atomic configuration of the H_i-Al_{Ge} defect complex in r-GeO_2.

the relation, n_c $(0.2/a_H)^3$, where a_H is the acceptor-bound hole wave function and is calculated to be a_H = 3.38 Å.[81] Although the solubility of Al_{Ge} is limited at the Fermi level near the VBM, the heavy doping of Al_{Ge} up to the critical Mott density can be achieved by hydrogen co-doping at a growth temperature above 536 °C. Owing to the strong Coulomb interaction between Hi and Al_{Ge}, the formation energy of H_i-acceptor defect complexes is only 0.36 eV in the neutral charge state (Fig. 3.4). Therefore, the H co-doping can effectively enhance the solubility of Al_{Ge} acceptor up to the Mott-transition limit. At the same time, H co-doping shifts the Fermi level far above the VBM, which increases the formation energy of V_O and prevents the charge compensation from V_O. In order to reactivate the hole carrier, H needs to be dissociated from Al acceptors. We calculated the binding energy between Al_{Ge} and H_i is 0.96 eV, which is achievable using high-temperature post-annealing techniques. This technique has been widely used for p-type doping of GaN with Mg, where thermal annealing at 700 °C effectively dissociates H that binds to Mg with a binding energy of 0.7 eV.[72,82] Therefore, we suggest the possibility of p-type doping of r-GeO_2 with Al dopants by co-doping with hydrogen and subsequent annealing to lower the large acceptor ionization energy and overcome the passivation from compensating defects such as V_O.

3.3 Mobility

Bushick et al.[83] predicted phonon-limited electron and hole mobilities of r-GeO_2 by first-principles calculation. The calculation is based on density functional theory and density functional perturbation theory within Quantum ESPRESSO[55,56,84] and the iterative Boltzmann transport equation with the EPW code[60,62,85]. Fig. 3.5 shows the calculation results on the temperature dependence of the electron and hole mobility along $\Gamma \rightarrow X$ ($\perp c$) and $\Gamma \rightarrow Z$ ($\parallel c$) directions. The converged carrier mobilities at 300 K are $\mu_{elec,\perp c}$ = 244 cm^2 V^{-1} s^{-1}, $\mu_{elec,\parallel c}$ = 377 cm^2 V^{-1} s^{-1}, $\mu_{hole,\perp c}$ = 27 cm^2

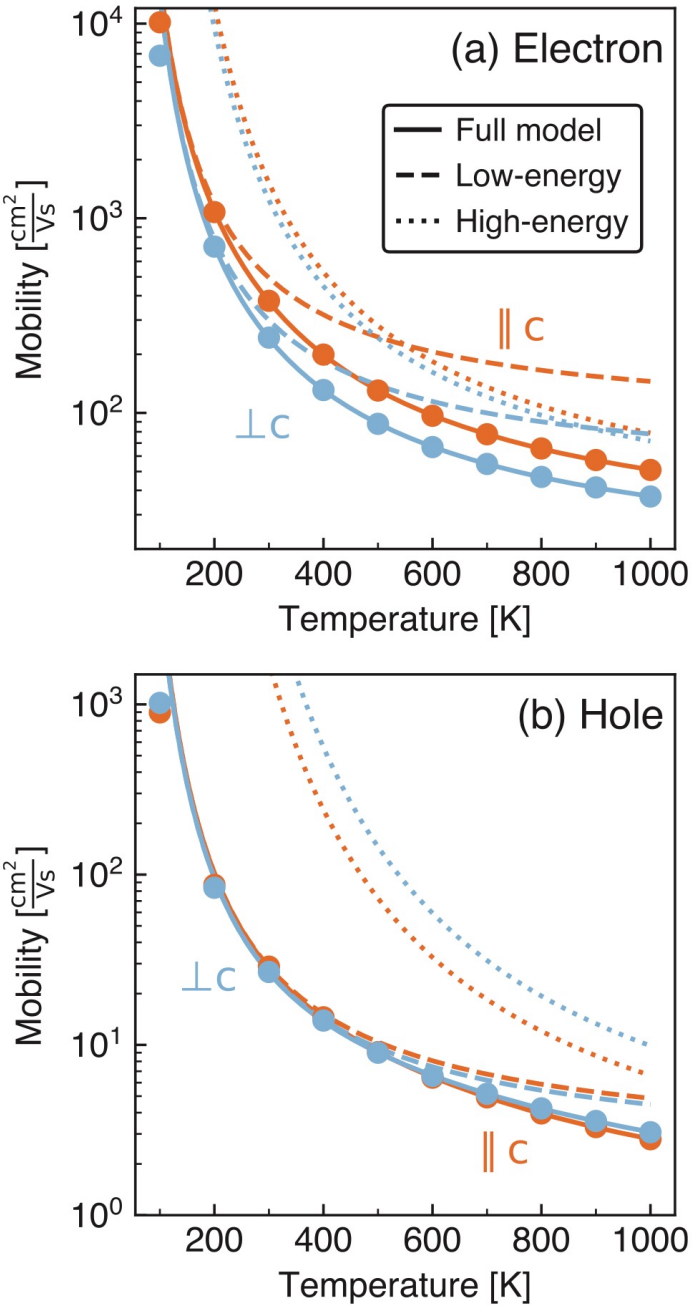

Figure 3.5: Electron and hole mobility of r-GeO_2 along the $\perp$ c and $\parallel$ c directions as a function of temperature for a carrier concentration of $n = 10^{17}$ cm^{-3}. The solid curves are fitted to the equation: $\frac{1}{\mu(T)} = \frac{1}{\mu_1} e^{-\frac{T_1}{T}} + \frac{1}{\mu_2} e^{-\frac{T_2}{T}}$, where (μ_1, T_1) characterizes to the low-energy polar-optical modes (the dashed line) and (μ_2, T_2) characterizes to the high-energy polar-optical modes (the dotted line).

V^{-1} s^{-1}, and $\mu_{hole,\|c} = 29$ cm^2 V^{-1} s^{-1}. The anisotropy of the mobility is primarily driven by the anisotropy of the effective mass. E.g., electron effective mass obtained from G_0W_0 band structure is 1.7 times lighter for the direction compared to the direction, which is consistent with the 1.5 times higher mobility along the direction. On the other hand, hole mobility is approximately isotropic due to the relatively small directional dependence of the hole effective mass. By fitting the calculation data on the temperature dependency equation with two characteristic optical modes, it is determined that the low-energy polar-optical phonon modes are the dominant contribution to the carrier scattering at room temperature.

Compared to emerging UWBG semiconductors, the electron mobility of r-GeO_2 is lower than AlN and diamond, but is approximately 2 times higher than β-Ga_2O_3 where the highest Hall mobility measured is 184 cm^2 V^{-1} s^{-1} at 300 K[86]. In addition, while p-type doping of β-Ga_2O_3 is limited by self-trapped hole polarons[65], the hole mobility of r-GeO_2 is comparable to that of GaN (31 cm^2 V^{-1} s^{-1})[87], which is a known ambipolar semiconductor applicable to bipolar junctions. Combined with the theoretical prediction of ambipolar dopability, the predicted electron and hole mobilities show that r-GeO_2 is a promising ambipolar UWBG semiconductor.

3.4 Thermal conductivity

3.4.1 Synthesis of bulk r-GeO_2 pellets

To characterize the thermal conductivity of r-GeO_2, we synthesized a polycrystalline, bulk pellet of r-GeO_2 using hot-press. Quartz-phase GeO_2 powder (Alfa Aesar, 99.999%) were loaded into a 10 mm-diameter graphite die and sintered at 800 °C under a pressure of 100 MPa for 3 hrs while the chamber environment being kept under vacuum (10^{-2} Torr) during the pressing. After hot-pressing, a dense, bulk pellet is obtained, and the x-ray diffraction (XRD) indicates that the phase of GeO_2 trans-

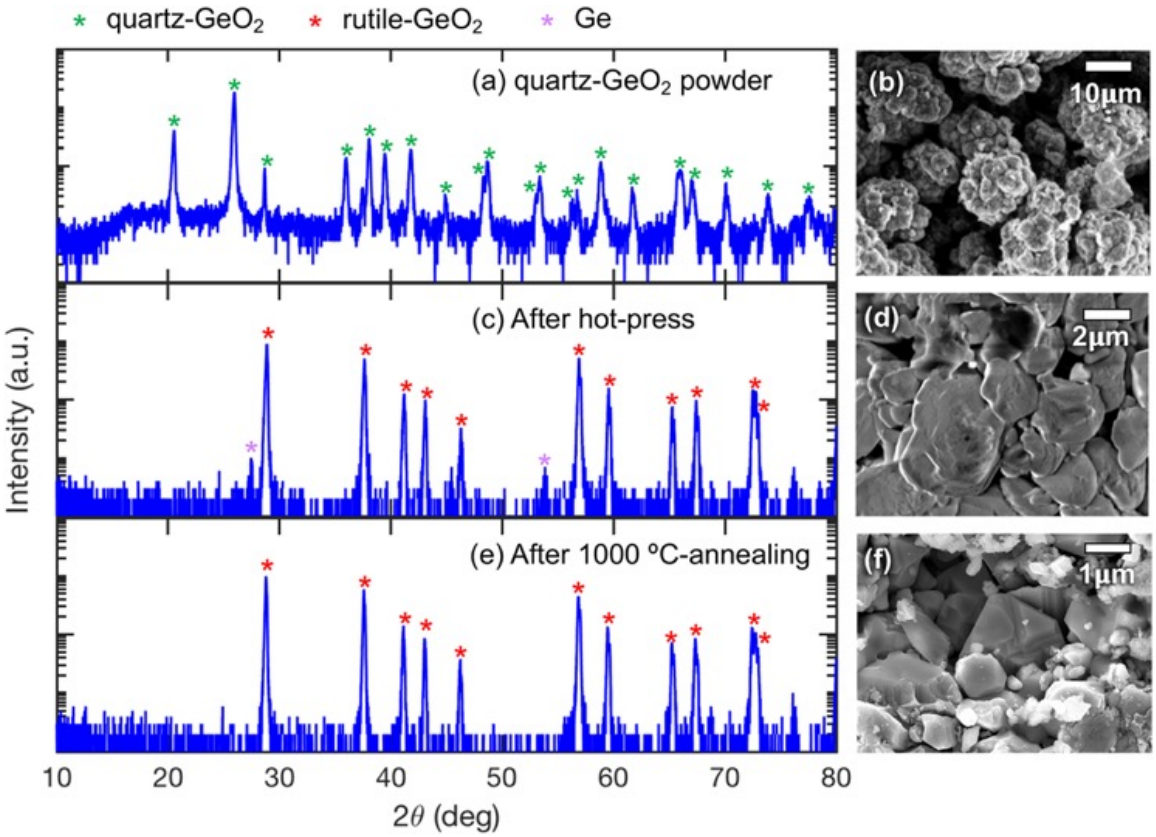

Figure 3.6: X-ray diffraction pattern and scanning electron microscope images of (a-b) GeO_2 powders, (c-d) a GeO_2 pellet after hot pressing at 800 °C and 100 MPa, and (e-f) a GeO_2 pellet after hot pressing and subsequent annealing at 1000 °C in the air. A phase-pure rutile GeO_2 pellet is obtained through hot-pressing and subsequent annealing, with grain sizes of 1.50 ± 0.30 μm.

formed from quartz into rutile (Fig. 3.6 (a) and (c)). However, $< 2\%$ impurity Ge phase is also observed by the XRD. In order to oxidize any Ge impurity phase, we annealed the hot-pressed pellet at 1000 °C in the air for 2 hrs. Our XRD analysis shows that the final project is a polycrystalline rutile GeO_2 pellet without a noticeable impurity phase (Fig. 3.6 (e)). The scanning electron microscope (SEM) images in Fig. (b, d, f) show the change of microstructure of our sample before and after hot-press and after subsequent annealing. We observed grain size of 2 – 5 μm for the pellet after hot-pressing. The subsequent annealing recovers the 3-dimensional grain structures with the average grain size of 1.50 μm.

3.4.2 Thermal conductivity measurement of r-GeO_2

We measured the mass density (ρ) of our pellet using Helium gas pycnometry on a Micromeritics Accupyc II 1340. We obtained $\rho = 6.39 \pm 0.04$ g cm^{-3}, which is 1.9% higher than the ideal value for rutile GeO_2 (6.27 g cm^{-3}). We subsequently measured specific heat capacity (C_p) and thermal diffusivity (D) of the r-GeO_2 pellets as a function of temperature by using a laser flash system (Linseis LFA-1000). Pellets were lightly coated with graphite spray to absorb the laser. During the measurement, the laser heats the sample from the bottom side and the detector detects the time-dependent temperature rise on top. To avoid any oxidation during the measurement at high temperature, the measurement was performed under flowing N_2 gas. For each measurement step, we measured a Pyroceram 9606 reference sample and determined the measurement error, which is $< 1\%$ for specific heat capacity and $< 4\%$ for thermal diffusivity.

Fig. 3.7 (a) shows the specific heat capacity of our r-GeO_2 sample, which is compared with the theoretical values of the constant-volume specific heat capacity (C_v) of r-GeO_2 from ref.[88] as well as from our calculation and the experimentally measured C_p data from ref.[89]. The difference between C_p and C_v (C_p - $C_v = \frac{TV\alpha^2}{K}$)

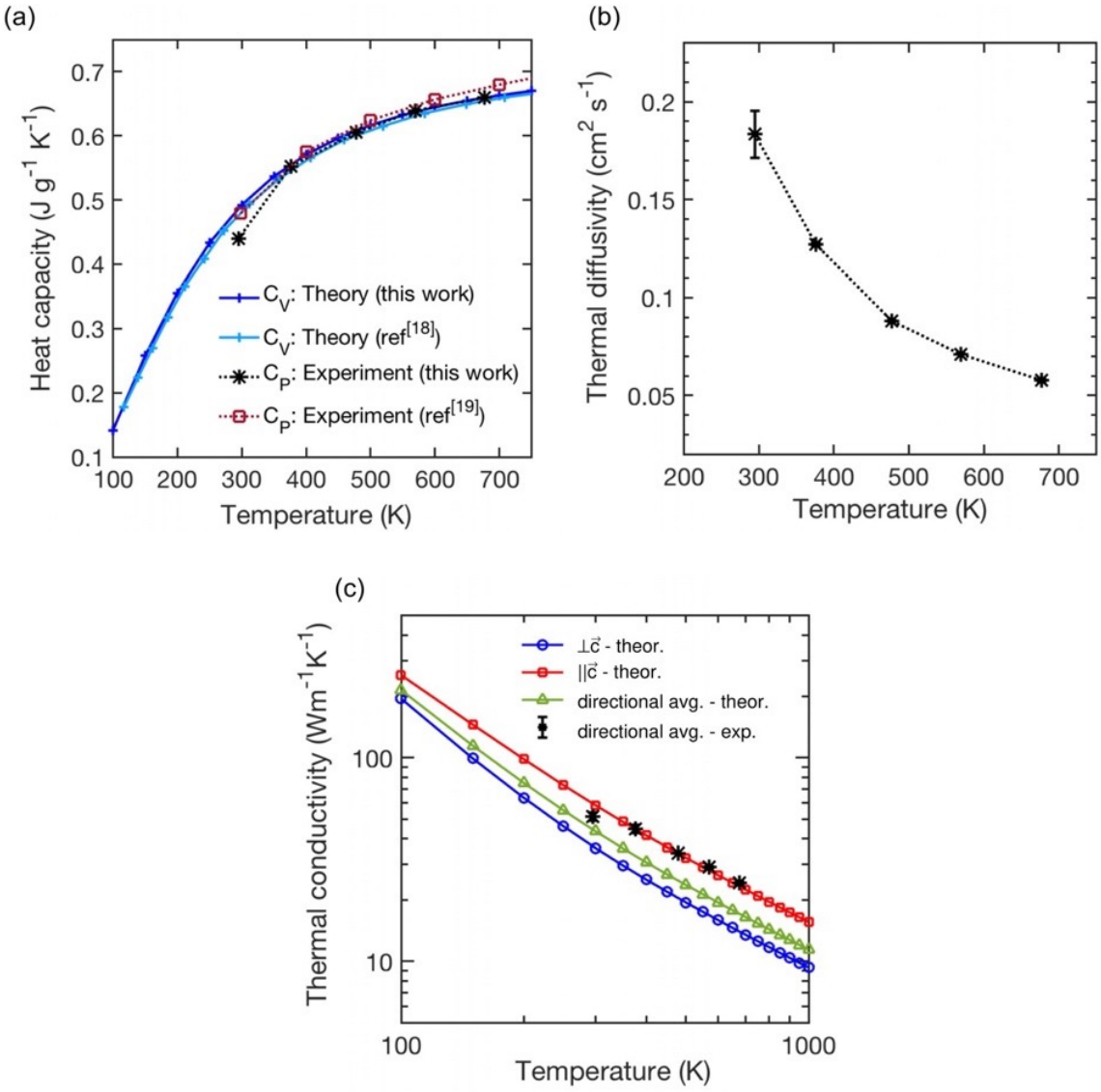

Figure 3.7: (a) The calculated constant-volume specific heat (C_v) of r-GeO_2 and the measured constant-pressure specific heat (C_p) of r-GeO_2 as a function of temperature. Our measured C_p data shows good agreement with our calculated C_v data and the data from previous reports. (b) Thermal diffusivity of polycrystalline r-GeO_2 as a function of temperature measured by the laser-flash method. (c) Experimental and theoretical thermal conductivity of r-GeO_2 from 100 K to 1000 K.

is estimated to be less than 1 % at room temperature, where V is the molar volume (1.597×10^{-7} m^3 g^{-1}), α is the thermal expansion coefficient (14.2×10^{-6} K^{-1}), and K is the compressibility (4.05×10^{-12} Pa^{-1}). Our C_p data agrees well with the reported C_p and C_v data. Fig. 3.7 (b) shows the temperature dependent thermal diffusivity of our r-GeO_2 sample. Thermal diffusivity decreases upon heating from 0.183 cm^2 s^{-1} at room temperature to 0.058 cm^2 s^{-1} at 677 K.

We then obtained the thermal conductivity (κ) of our r-GeO_2 sample as a function of temperature using the equation:

$$\kappa = D \cdot C_p \cdot \rho \tag{3.1}$$

and plotted in Fig. 3.7 (c). The measured thermal conductivity values are also compared with the theoretical thermal conductivity values calculated based on the density functional perturbation theory and Boltzmann transport equation (BTE) as implemented in the almaBTE software.[90] The measured thermal conductivity is slightly higher than the directionally averaged values of the theory throughout the temperature range. We observe that the temperature dependence of the measured thermal conductivity is consistent with the trend predicted by theory (1/T), which indicates the thermal transport is governed by phonon scattering. The measured thermal conductivity at 300 K is 51 W m^{-1} K^{-1}, approximately 2 times higher than the highest value of β-Ga_2O_3,[44] demonstrating that r-GeO_2 is a promising alternative material that can solve the thermal management challenges with β-Ga_2O_3-based electronics. In addition, while β-Ga_2O_3 can only be grown on thermally poor substrate (e.g., Al_2O_3), the higher symmetry of r-GeO_2 allows thin-film growth on thermally conductive epitaxial substrates such as SnO_2 ($\kappa \sim 100$ W m^{-1} K^{-1})[91,92], therefore, r-GeO_2 enables electronic device architectures with better thermal conduction.

3.5 Thin film growth of r-GeO_2 by molecular beam epitaxy

3.5.1 Challenges with the film growth of r-GeO_2

Current semiconductor devices are based upon the fabrication of high-quality thin films. Despite the superior material properties of r-GeO_2 predicted by theory, experimental investigation of r-GeO_2 for its potential electronic applications has been limited by the technical challenges associated with the material synthesis of r-GeO_2 as a crystalline thin film. A major challenge for synthesis of r-GeO_2 thin films lies in the presence of deeply metastable competing phases – quartz and amorphous phases (Fig. 3.8). Particularly, along with SiO_2 and BO_3, GeO_2 is a strong glass former.[93] Prior works report the growth of GeO_2 films using pulsed laser deposition,[94–96] sputtering,[97–100] and thermal evaporation,[101] but the as-deposited GeO_2 films are all amorphous, indicating a strong tendency for glass formation. In addition, the high pressure of GeO poses a challenge in r-GeO_2 thin film synthesis as it induces a significant desorption rate during the deposition process. The volatilization of GeO has been a big challenge in Ge CMOS which even occurs below 500 °C at the Ge and GeO_2 interface.[18,102] The thermodynamically unstable nature of Ge native oxides significantly limits the material processing window such as growth temperature and pressure.

In addition, candidate substrates for r-GeO_2 epitaxial film growth all have relatively large lattice mismatch. Though rutile compounds exist in a wide range of lattice parameters, TiO_2 and MgF_2 are among the few commercial substrates having the rutile crystal structure (Fig. 3.9). Among these, TiO_2 has the smaller misfit with GeO_2 (4.46 % and 3.35 % along the a and c axis). However, the disadvantage of a TiO_2 substrate is that it has a narrower band gap (3.0 eV) than GeO_2 and becomes easily conductive under the formation of oxygen vacancies or impurity defects, which affects the electrical and optical characterization of GeO_2 thin films. A MgF_2

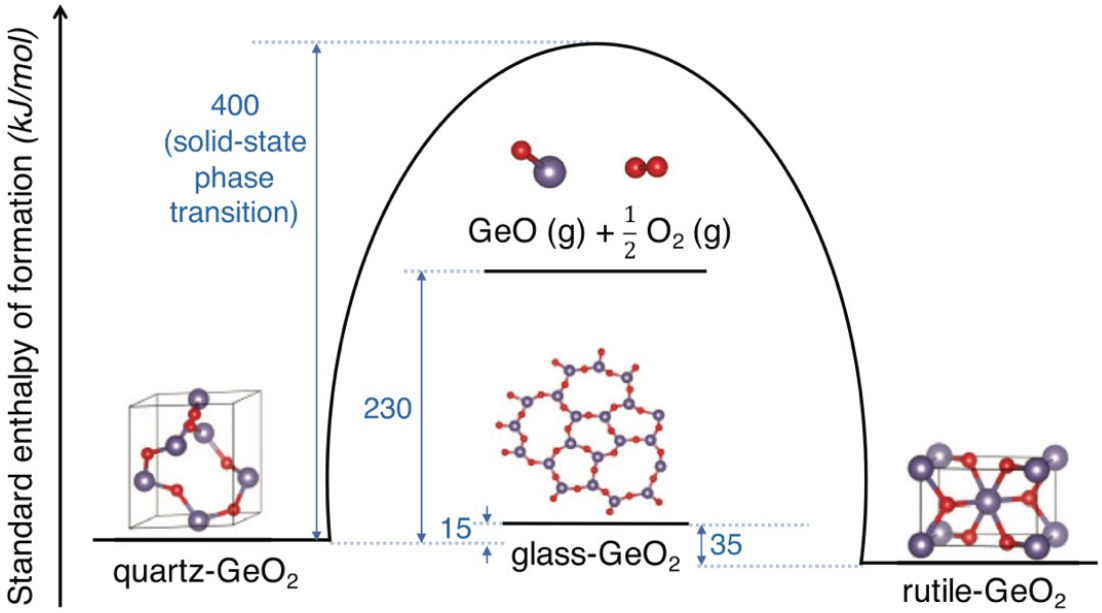

nd GeO and O_2 molecules crystallize into the rutile phase on the substrates [GeO (g) + $\frac{1}{2}O_2$ (g) → rutile-GeO_2]. The values for the energy differences are from refs.[103–106]]Reaction coordinate-energy diagram for different polymorphs of GeO_2. At the atmospheric condition, the thermodynamic stability of both metastable quartz and glass phases is competitive to the thermodynamically stable rutile phase. Solid-state reaction of quartz to rutile requires traversing a large energy barrier (400 kJ/mol at 1 atm). Much less energy is required to sublime GeO_2 as GeO (g) + $\frac{1}{2}O_2$ (g) and re-condensate it into the rutile phase. For the molecular beam epitaxy of r-GeO_2, quartz-GeO_2 powders are evaporated using the effusion cell [quartz-GeO_2 → GeO (g) + $\frac{1}{2}O_2$ (g)] and GeO and O_2 molecules crystallize into the rutile phase on the substrates [GeO (g) + $\frac{1}{2}O_2$ (g) → rutile-GeO_2]. The values for the energy differences are from refs.[103–106]

Figure 3.8: a

substrate has large lattice misfit of 5.22 % ($\parallel a$) and 6.44 % ($\parallel c$) with GeO_2 and it complicates the growth of oxide films as the surface termination of fluorine often challenges the interfacial bonding of oxides, whereas a non-isostructural sapphire substrate can lead to degraded crystallinity of films with high density of defects and dislocations. Sapphire (Al_2O_3) is also a widely used substrate that templates rutile films due to the coincidence of the atomic configuration in certain planes. Prior works have reported the growth of rutile films (e.g. SnO_2) on sapphire substrates with various orientations and determined the orientation relationships between the rutile and sapphire are $(101)//(1\bar{1}02)$, $(001)//(10\bar{1}0)$, and $(\bar{1}01)//(11\bar{2}0)$.[107,108] Though Al_2O_3 is a widely used insulating substrate for UWBG semiconductor thin films due to wide band gap of 7.8 eV, it also has large lattice misfit with GeO_2 (8.09 % and -3.63 % along a and c axis respectively).

In this work, we synthesized r-GeO_2 thin films on sapphire substrates using molecular beam epitaxy. We control the competing reactions and stabilize the rutile-phase growth by utilizing (1) a buffer layer with reduced lattice misfit to reduce epitaxial strain and (2) the growth condition that allows the condensation of the preoxidized molecular precursor yet provides sufficient adatom mobility. We will discuss the details of growth condition in the following sections.

3.5.2 Experimental procedure

Experimental procedure for the r-GeO_2 growth on (Sn,Ge)O_2/SnO_2-buffered R-plane sapphire substrates is described. Prior to growth, a 200 nm thick Pt was deposited on the back side of the substrates to enhance the efficiency of radiation heating from the substrate heater. For Ge and Sn source, GeO_2 powder (Alfa Aesar, 99.999%) and SnO_2 powder (Alfa Aesar, 99.996%) were used to generate preoxidized mono-oxide beam fluxes. The flux from the source materials was calibrated using a quartz crystal microbalance (QCM) before each deposition. For GeO_2 deposition, the

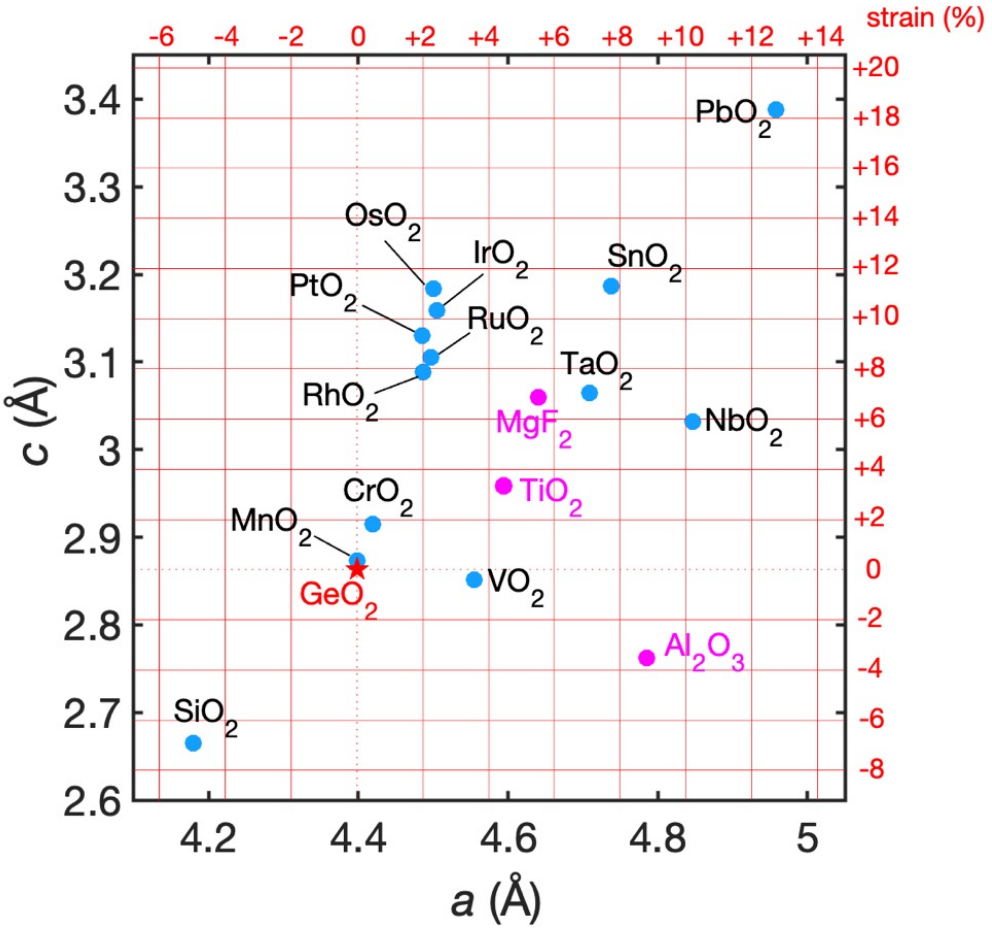

Figure 3.9: The a and c lattice parameters of rutile compounds. The grid line indicates misfit strain with respect to GeO_2. TiO_2, MgF_2 and Al_2O_3 are commercially available rutile substrates. The lattice parameters of Al_2O_3 are chosen to meet the epitaxial relation with rutile structure (the a lattice parameter is the a lattice parameter in the hexagonal conventional cell of Al_2O_3 and the c lattice parameter is $a/\sqrt{3}$). The lattice parameter information on the the plot is adopted in ref.[16]

flux of GeO_2 was calibrated at 6.9×10^{13} molecules cm^{-2} s^{-1}. For the deposition of a (Sn,Ge)O_2 buffer layer, the flux of GeO_2 was varied from 5.5×10^{12} to 1.4×10^{14} molecules cm^{-2} s^{-1} and the flux of SnO_2 from 8.5×10^{12} to 5.3×10^{13} molecules cm^{-2} s^{-1} to study the compositional effect of the (Sn,Ge)O_2 buffer layer on the crystallinity of r-GeO_2 thin film. Owing to the generation of the parasitic oxygen molecule while heating GeO_2 and SnO_2 sources, the base pressure of the growth chamber was on the order of 10^{-7} Torr.

For the deposition of Ge_2/(Sn,Ge)O_2/SnO_2 films on a sapphire substrate, we first deposited a rutile SnO_2 seed layer at a substrate temperature of 600 °C and an ozone back ground pressure of 7×10^{-6} Torr for 15 min, and then opened both GeO_2 and SnO_2 shutters to deposit the (Sn,Ge)O_2 buffer layer for 1 hr. After the buffer layer deposition, the substrate was cooled down to 450 °C, the ozone background pressure was decreased to 1×10^{-6} Torr, and a GeO_2 thin film was deposited.

3.5.3 Precursor

For oxide MBE, it is typical to co-supply elemental metal and reactive oxygen species (i.e., ozone or oxygen plasma), and films are synthesized from the oxidation of metal species. However, in the case of group-III and IV oxides (e.g., Ga_2O_3, In_2O_3, SnO_2, or GeO_2), the elemental metal can oxidize into suboxides (e.g., Ga_2O, In_2O, SnO, and GeO) on the film surface, which can lead to metal-rich stoichiometry of films or high desorption rate. The use of a pre-oxidized metal source can have advantages in achieving a better growth rate and film quality as it uses simpler reaction kinetics without intermediate reaction products.[109] For instance, Raghavan et al.[110] achieved two-dimensional growth of $BaSnO_3$ films with enhanced mobility by using a SnO_2 source, contrary to a Sn source which causes the formation of Sn-excess defective interface layers and promotes island growth of films with degraded mobility. GeO (g) is even more volatile than SnO (g) or Ga_2O (g).[111] To prevent similar challenges of

using metallic source, we use a GeO_2 powder for the Ge source, evaporate the source in the effusion cell to establish a molecular flux of GeO (g), and have GeO (g) oxidize with ozone on the substrate surface to form GeO_2 films.

3.5.4 Temperature and pressure

In order to determine the growth window (substrate temperature, T_s and total background pressure including ozone and molecular oxygen flux from the source, P) for the epitaxial stabilization of r-GeO_2 films, we studied the growth of GeO_2 films on a (Sn,Ge)O_2/SnO_2-buffered R-plane sapphire substrate at a range of T_s (from 375 °C to 750 °C) and P (from 10^{-6} Torr to 10^{-5} Torr). Since the stabilization of r-GeO_2 is dependent on the composition of (Sn,Ge)O_2 buffer layer as will be discussed later, we used the (Sn,Ge)O_2 buffer layer with the maximal Ge incorporation while maintaining the rutile structure which leads to the minimum misfit strains of 5.0 % and 4.4 % along the [$\bar{1}$01] and [010] axis. An empirical phase diagram is shown in Fig. 3.9 (a). We find that GeO (g) desorption dominates when $T_s \geq 600$ °C and $P = 10^{-6}$ Torr and $T_s \geq 750$ °C and $P = 10^{-5}$ Torr, as determined by monitoring RHEED patterns during GeO_2 deposition, indicating highly volatile properties of GeO (g). For all T_s studied at $P = 10^{-5}$ Torr and $T_s = 475$ °C at $P = 10^{-6}$ Torr, the resultant films are in amorphous phase (Fig. 3.9 (b,d)). We assume that the amount of oxygen reactants on the film surface are too high compared to GeO_x (g) reactants in this regime due to either high oxygen pressure at $P = 10^{-5}$ Torr or the sublimination of GeO (g) at $T_s \geq 475$ °C, and the imbalance between the amount of GeO_x (g) and O_2 (g) reactants promotes the formation of amorphous phase. At $T_s \leq 400$ °C, the film deposits as amorphous, suggesting that this temperature range does not provide sufficient adatom mobility to crystallize.

The range of T_s from 425 °C to 450 °C at $P = 10^{-6}$ Torr is found to stabilize crystalline r-GeO_2 throughout the deposition. In this growth window, the RHHED

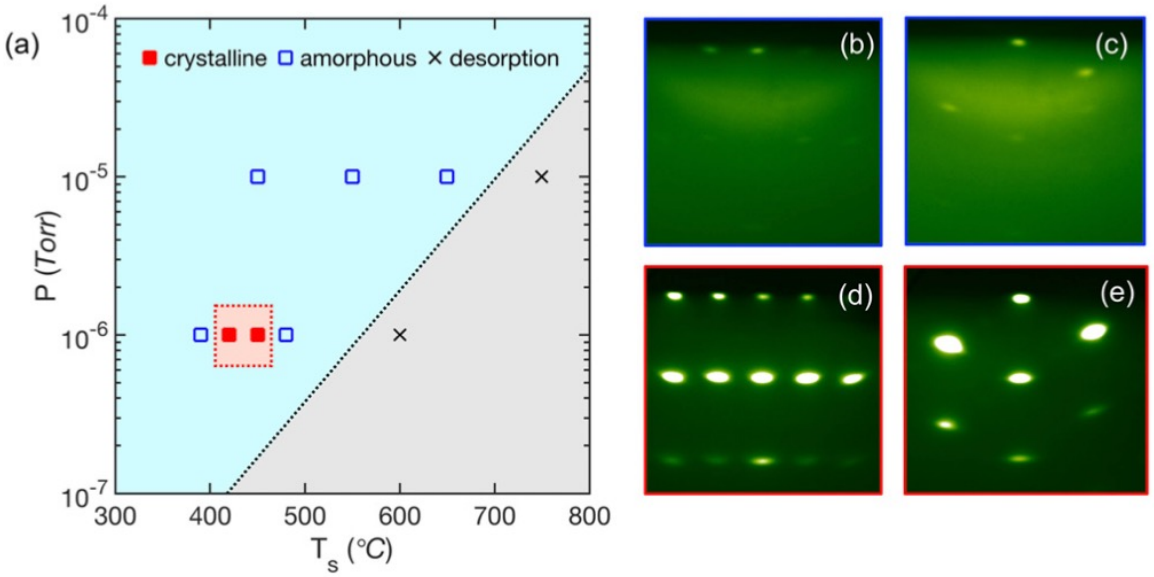

nd (c,e) z = $[1\bar{1}\bar{1}]$. A hazy background and a ring feature are seen for (b,c) amorphous GeO_2 films and (d,e) bright diffraction spots are seen for single crystalline r-GeO_2 films.](a) The substrate temperature (T_s) and pressure (P) phase map for GeO_2 film deposition on a (Sn,Ge)O_2/SnO_2-buffered R-plane sapphire substrate. (b)-(e) RHEED patterns observed after 2 h deposition of GeO_2 films recorded at two different azimuths of (b,d) z = $[10\bar{1}]$ and (c,e) z = $[1\bar{1}\bar{1}]$. A hazy background and a ring feature are seen for (b,c) amorphous GeO_2 films and (d,e) bright diffraction spots are seen for single crystalline r-GeO_2 films.

Figure 3.10: a

pattern remain spotty throughout the growth as shown in Fig. 3.9 (d) and (e), indicating a three-dimensional growth mode but a single crystalline film. Our results indicate that the stabilization of r-GeO_2 thin films requires a thermodynamic growth condition that balances GeO (g) adsorption and desorption yet provides sufficient adatom mobility as well as a proper ratio between GeO_x (g) and O_2 (g) reactants.

3.5.5 Buffer layer

To investigate the effect of lattice mismatch on the epitaxial stabilization of r-GeO_2 thin films, we synthesized a GeO_2 thin film on a (Sn,Ge)O_2 buffer layer with varied composition (Fig. 3.11(a-d)). The composition of a (Sn,Ge)O_2 buffer layer is tuned by adjusting the supplied flux ratio between SnO_2 and GeO_2 as well as

the ozone pressure (Fig. 3.11(e)). When the supplied flux ratio between SnO_2 and GeO_2 is 1 : 0.1 at the background ozone pressure of 1×10^{-6} Torr, the 101 peak position of the (Sn,Ge)O_2 layer from x-ray diffraction does not noticeably shift from the SnO_2 (101) peak position, indicating a highly Sn rich film with the corresponding lattice misfit strains with r-GeO_2 of 9.0 % and 7.1 % along the [$\bar{1}$01] and [010] axis, respectively (Fig. 3.11 (a)). When the supplied flux ratio between SnO_2 and GeO_2 is 1 : 0.4, we observe a distinct (Sn,Ge)O_2 (101) peak, still, the peak position is much closer to SnO_2 (Fig. 3.11(b)). In these two cases, GeO_2 films deposited on top of the Sn-rich (Sn,Ge)O_2 buffer layer immediately turned into the amorphous phase as observed by in situ RHEED pattern.

When the supplied flux ratio between SnO_2 and GeO_2 is 1 : 2.5, the (Sn,Ge)O_2 film peak further moved toward the GeO_2 film peak position and the corresponding lattice constants are $a = 4.618$ Å and $c = 3.059$ Å (the corresponding misfit strains with GeO_2 are 5.8 % and 4.8 % along the [$\bar{1}$01] and [010] axis respectively). On this buffer layer, GeO_2 starts grow in the crystalline phase (Fig. 3.11(c)) but transits into the amorphous phase after 30 min of deposition as observed by in situ RHEED. To incorporate more Ge into the (Sn,Ge)O_2 buffer layer and further reduce the misfit-strain on the GeO_2 film, the ozone pressure was increased up to 7×10^{-6} Torr at the fixed flux ratio of SnO_2 and GeO_2 (1 : 2.5) to reduce desorption of volatile GeO (g). The lattice constants for this (Sn,Ge)O_2 buffer layer are $a = 4.598$ Å and $c = 3.026$ Å, which are approximately the average value of SnO_2 and GeO_2, and the corresponding calculated misfit strains with GeO_2 are 5.0 % and 4.4 % along the [$\bar{1}$01] and [010] axis respectively. Using this buffer layer, we were able to stabilize rutile GeO_2 throughout the 2 hours (or longer) deposition ($\sim$20 nm thick film) as shown in Fig. 3.11(d). Our results show that the degree of lattice mismatch is crucial for epitaxial stabilization of the r-GeO_2 thin film, and the lattice mismatch value smaller than 4.4 % ($\parallel a$) and 5.3 % ($\parallel c$) is required to stabilize a r-GeO_2 thin film on a (Sn,Ge)O_2/SnO_2 buffered

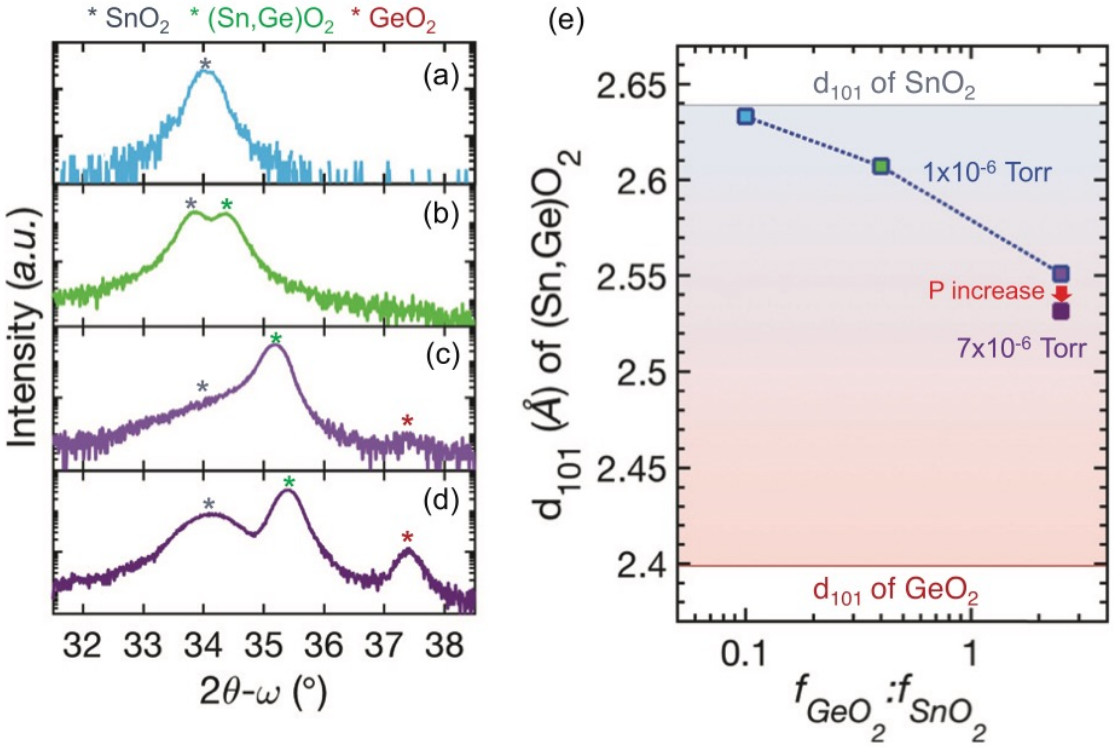

Figure 3.11: (a) – (d) X-ray diffraction of 2 hours-deposited GeO_2/(Sn,Ge)O_2/SnO_2 films on R-plane sapphire substrates with the varied composition of (Sn,Ge)O_2. The composition is tuned by the incoming flux ratio between GeO_2 and SnO_2 as well as the ozone pressure. The GeO_2:SnO_2 flux ratio is (a) 0.1, (b) 0.4, and (c-d) 2.5 and the ozone pressure during (Sn,Ge)O_2 deposition is (a-c) 1×10^{-6} Torr and (d) 7×10^{-6} Torr. (e) The out-of-plane planar spacing, d_{101}, of (Sn,Ge)O_2 as a function of the ratio between the supplied flux ($f_{GeO_2} : f_{SnO_2}$) deposited at different ozone pressures.

sapphire substrate.

3.5.6 Structural characterization of r-GeO_2 thin films

We then analyzed the crystal structure and epitaxial registry of 4 hrs-grown r-GeO_2 thin films on the optimized (Sn,Ge)O_2 buffer layers (flux ratio of Ge : Sn = 2.5 : 1 and P = 7×10^{-6} Torr). In Fig. 3.12(a), we observe strong diffraction peaks for the films in the x-ray diffraction $2\theta - \omega$ scan, which correspond to the (101)-orientation of rutile SnO_2, (Sn,Ge)O_2, and GeO_2, respectively. No other peaks corresponding to impurity phase or other orientation are present in the wide-range x-ray diffraction

scan, revealing single-crystalline r-GeO_2 thin films. The out-of-plane planar spacing, d_{101}, is determined to be 2.629 Å for SnO_2, 2.533 Å for (Sn,Ge)O_2, and 2.401 Å for GeO_2. The measured d_{101} values for SnO_2 and GeO_2 are close to the bulk values (2.639 Å for SnO_2 and 2.400 Å for GeO_2).

In order to determine the lattice constants and in-plane misfit strain of the films, a reciprocal space map around the asymmetric 112 reflections of the rutile films was measured in Fig. 3.12(b). The a and c lattice parameters of the SnO_2 film determined by a reciprocal space map are 4.612 Å and 3.199 Å and the corresponding film strains along the a and c directions are -2.50 % and 0.61 %, respectively. The a and c lattice parameters of the (Sn,Ge)O_2 film are 4.598 Å and 3.026 Å, and assuming linear Vegard's law for the a and c lattice parameters, we estimated the composition of Ge in the (Sn,Ge)O_2 film is 0.39 – 0.49. The a and c lattice parameters of the GeO_2 film are 4.390 Å and 2.865 Å. These values are close to the bulk lattice constants (a = 4.394 Å and c = 2.866 Å), suggesting that the GeO_2 film is relaxed at 40 nm thickness.

We then determined the epitaxial relationship of our samples from the x-ray diffraction $2\theta - \omega$ scan for the asymmetric rutile 002 Bragg peaks in skew geometry at $\chi = 33^\circ$ (Fig. 3.12(c)). The [001] directions of the rutile layers are found to be parallel to the $[1\bar{1}00]$ direction of the Al_2O_3 substrate. Projection of these directions onto the (101) and (1bar102) planes of GeO_2 and Al_2O_3, respectively, gives an in-plane registry of [010] GeO_2 ∥ $[11\bar{2}0]$ Al_2O_3 and $[\bar{1}01]$ GeO_2 ∥ $[\bar{1}101]$ Al_2O_3, which agrees with the prior reports on (101)-oriented SnO_2 film growth on R-plane sapphire substrate.[112] The schematic showing the epitaxial relationship between (101)-oriented rutile and $(1\bar{1}02)$-oriented corundum crystal structures is illustrated in Fig. 3.12 (d-f).

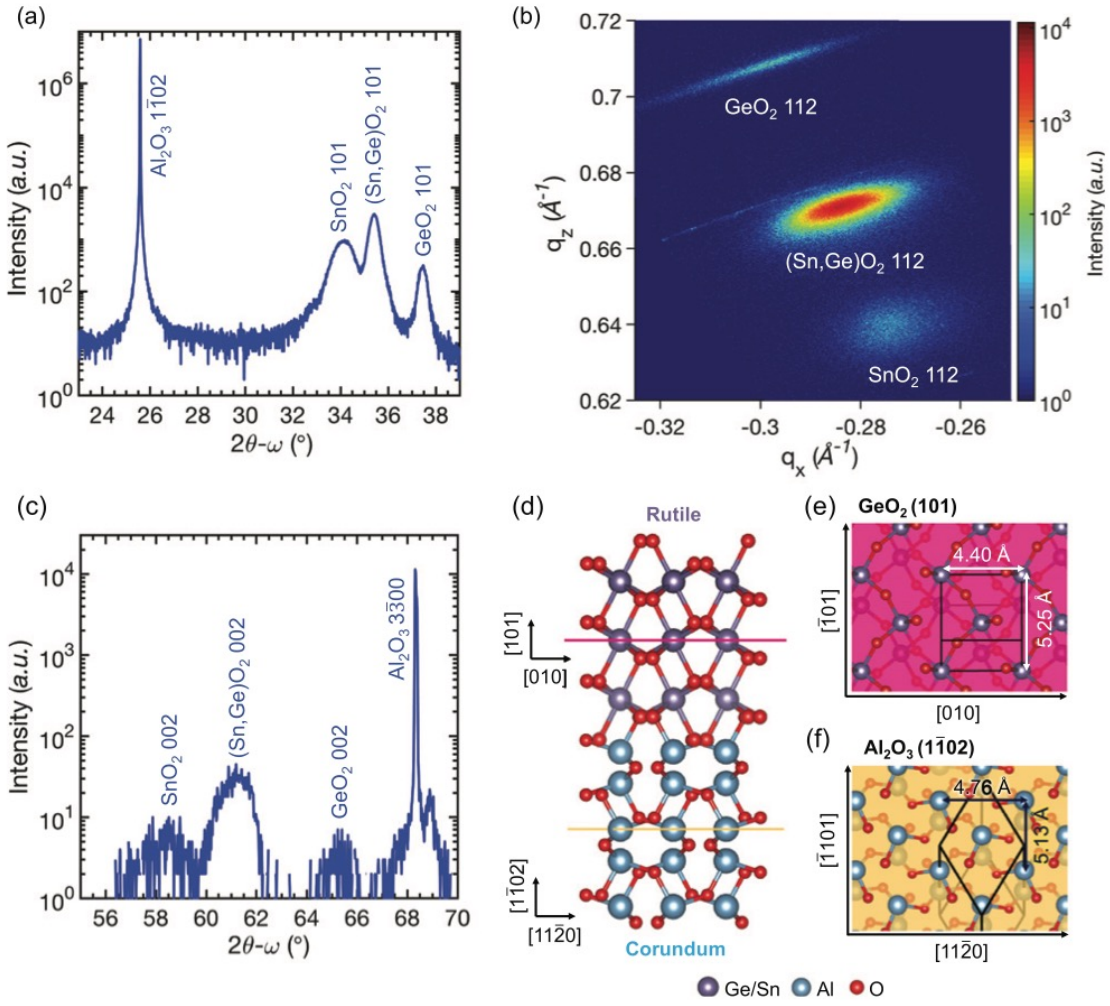

eO$_2$ ‖ [11$\bar{2}$0] Al_2O_3 and [$\bar{1}$01] GeO_2 ‖ [$\bar{1}$101] Al_2O_3. (d) Schematic of the epitaxial relationship between (101)-oriented rutile and (1$\bar{1}$02)-oriented corundum crystal structures viewed in the cross section down the [1$\bar{1}$01] axis of the corundum structure. (e-f) Schematics of the surface atomic configurations of (e) (101) r-GeO2 and (f) (1$\bar{1}$02) sapphire.](a) Symmetric X-ray diffraction of r-GeO_2/(Sn,Ge)O_2/SnO_2 films on a R-plane sapphire substrate. The layers were deposited for 15 min (SnO_2), 1 hr ((Sn,Ge)O_2), and 4 hrs (r-GeO_2). (b) An asymmetric reciprocal space map around the 112 reflections of the films. (c) Asymmetric X-ray diffraction of r-GeO_2/(Sn,Ge)O_2/SnO_2 films on a R-plane sapphire substrate in skew-geometry with chi = 33°. The in-plane registry is [010] GeO_2 ‖ [11$\bar{2}$0] Al_2O_3 and [$\bar{1}$01] GeO_2 ‖ [$\bar{1}$101] Al_2O_3. (d) Schematic of the epitaxial relationship between (101)-oriented rutile and (1$\bar{1}$02)-oriented corundum crystal structures viewed in the cross section down the [1$\bar{1}$01] axis of the corundum structure. (e-f) Schematics of the surface atomic configurations of (e) (101) r-GeO2 and (f) (1$\bar{1}$02) sapphire.

Figure 3.12: G

3.6 Single crystal substrates of r-GeO_2

3.6.1 Motivation

All mature semiconductors can be grown with a high degree of crystallinity and can operate only if their defects and dopants can be controlled. For high structural quality, it is essential that a high-quality of (nearly) lattice-matched substrate is substrate is available. Although we demonstrate that single-crystalline r-GeO_2 thin films can be grown by molecular beam epitaxy, the available substrates all have large lattice difference with r-GeO_2 ($> 4\%$) leading to degraded crystallinity of r-GeO_2 thin films with high density of defects and dislocations. Therefore, a high-quality of lattice-matched substrate, or homoepitaxial substrates, will be needed to enhance structural quality of r-GeO_2 thin films and better control dopants in the films.

Various bulk synthesis techniques have been attempted to realize r-GeO_2 single crystals. Though GeO_2 has relatively low melting point (1115 °C), conventional crystal growth techniques from the melt such as Czochralski (CZ) or float zone (FZ) are not suitable for achieving r-GeO_2 single crystals owing to the presence of a high-temperature stable phase, quartz GeO_2, as shown in the phase diagram.[113] Instead, synthesis techniques that utilize lower temperature (less than 1030 °C where rutile phase is thermodynamically stable) or high pressure (to increase the rutile-to-quartz transition temperature) can synthesize r-GeO_2 crystals. For instance, the top-seeded flux technique is reported by Goodrum,[114] where alkali-oxide solvents are utilized to effectively lower the liquidus temperature below the rutile-to-quartz transition temperature and 10 mm-long r-GeO_2 crystals are synthesized at a temperature between 975 °C to 1050 °C. Single-crystal r-GeO_2 growth by chemical vapor transport is also reported. Agafonov et al.[115,116] synthesized r-GeO_2 crystals with a size of 0.5 × 0.5 × 2 mm^3 using a temperature gradient of 1000 – 900 °C in a sealed tube, where GeO_2 vaporizes at the high temperature zone and GeO molecules are carried by $TeCl_4$ and

HCl transport agents and re-condensed into rutile phase at the low temperature zone.

Despite the successful synthesis of millimeter-size r-GeO_2 crystals, the application of r-GeO_2 single crystals for thin film growth substrates has not been studied. In this section, by applying flux synthesis and mechanical polishing techniques, we showcase 4×2 mm^2 size r-GeO_2 single crystal substrates with highly crystalline surfaces that can be utilized for epitaxial film growth.

3.6.2 Experimental procedure

GeO_2 (Puratronic®, 99.999%), MoO_3 (Alfa Aesar, 99.95%), and Li_2CO_3 (ProChem Inc. ACS grade purity) were weighed in an approximate 1:16:10.5 molar ratio, with no drying or treatment of materials prior to reaction. Materials were loaded into a 30 mL Pt crucible (XRF Scientific, GC530). Crucible was loosely covered with a Pt lid and heated to 980 °C at a rate of 100 °C/hr, where the temperature was held for 1 hour. Then, the system was cooled to 600 °C at a rate of 0.5 °C/hr, upon which it was rapidly cooled to room temperature. Crystals were extracted from the crucible by sonicating the flux in deionized water. The largest size crystals were grown using the 0.5 °C/hr cooling rate along with crystals from previous growths as attempted seeds.

We then polished the crystal surface by using mechanical polisher and abrasives. The crystal was first mounted on a polisher using a thinning fixture and mounting wax. The crystal surface was then ground using 6 μm, followed by 3 μm, and lastly 1 μm diamond lapping films at the rotation speed of 30 rpm. To remove the finest scratches, we ground the surface again by using 0.05 m aluminum oxide abrasive film discs, followed by Final Green^{TM} films for the final step, at the rotation speed of 10 rpm for 1 hour at each step. Finally, to relieve any mechanical stress and repair surface crystallinity disrupted by the polishing step, the crystals were annealed in a tube furnace at 700 °C for 3 hours with 50 sccm O_2 gas flowing at the atmospheric

pressure.

3.6.3 Structural characterization of r-GeO_2 crystals

The optical image of the synthesized r-GeO_2 crystals is shown in Fig. 3.13(a). The crystals have a plate-shape geometry consistent with the Wulff construction for rutile crystals118 and the size of the crystals ranges from 1mm to 4 mm. Bulk crystallinity of our crystals is analyzed by the scanning transmission electron microscopy (STEM) and x-ray diffraction. The STEM images in Fig. 3.13(b-c) show that the r-GeO_2 crystals are highly crystalline with all atomic columns including O are clearly visible in the annual bright field (ABF) image. The planar spacing of $(\bar{1}10)$ and (001) are identified to be 3.17 Å and 2.86 Å, which agrees with the bulk lattice parameters of r-GeO_2. The x-ray diffraction was measured for a r-GeO_2 crystal with the largest-area facet oriented to the top surface. We observed two strong Bragg peaks at $2\theta = 28.61^\circ$ and $2\theta = 59.31^\circ$ which correspond to the (110) family of planes of r-GeO_2. Our result agrees with the Wulff construction for the rutile structures as the (110) plane has the lowest surface energy. No other diffraction peaks are detected, indicating that our r-GeO_2 crystals a single crystal without noticeable impurity phase.

To determine crystalline quality of our r-GeO_2 crystals, we measured the x-ray rocking curve of the 110 reflection and compared to the commercially available substrates such as a R-plane sapphire substrate. The FWHM of the X-ray rocking curve of the (110)-oriented r-GeO_2 single crystal was measured 0.0572°. This value is ∼6.7 times larger than that of the R-plane sapphire substrate (FWHM = 0.0085°).

3.6.4 Surface characterization of r-GeO_2 crystals

Figs. 3.14 (a) and (b) show the atomic force microscopy images of (a) as-grown r-GeO_2 single crystals and (b) r-GeO_2 single crystals after mechanical polishing. Before polishing, the surface has a nm-range roughness with pits of ∼300 nm width and

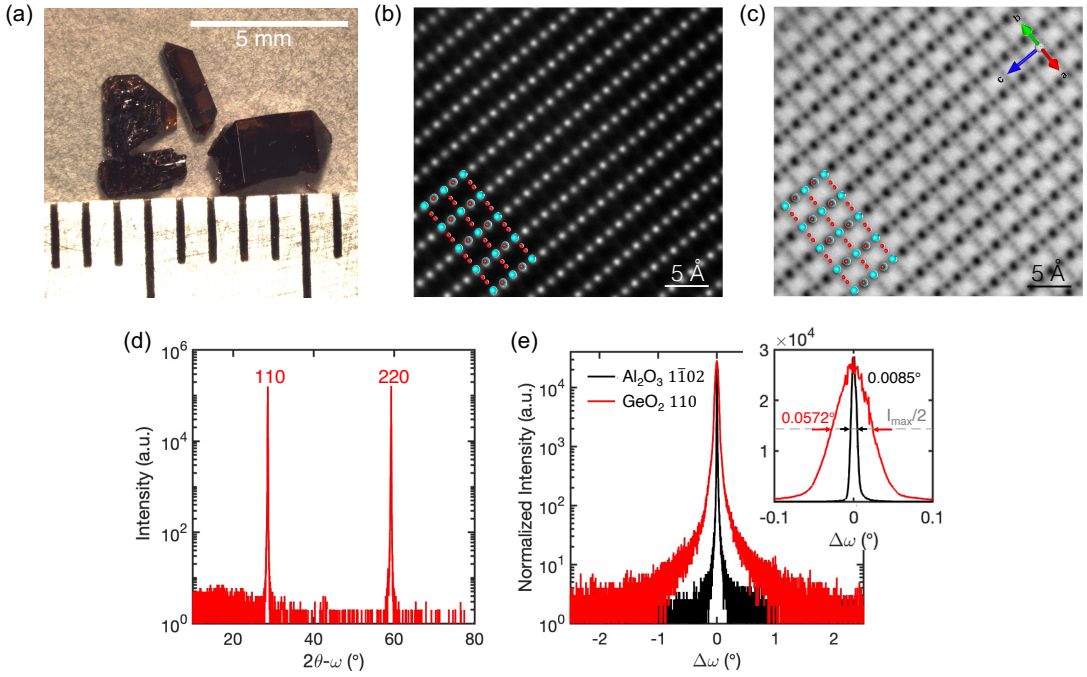

one axis. The overlayer represents the rutile structure with blue and red dots representing Ge and O atoms respectively and corroborates the rutile structure. The a and c lattice parameters are 4.40 Å and 2.86 Å respectively. (d) X-ray diffraction or r-GeO_2 single crystals with the largest-area facet oriented out-of-plane. (e) X-ray rocking curve of r-GeO_2 110 diffraction peak compared with the 1$\bar{1}$02 peak of a Al_2O_3 single crystal substrate purchased at MTI corporation.](a) Optical image of r-GeO_2 single crystals synthesized by the flux method. Crystal sizes reach up to 4 mm. (b) High-angle annular dark field and (b) bright field scanning transmission electron microscopy images of r-GeO_2 single crystals taken at the [110] zone axis. The overlayer represents the rutile structure with blue and red dots representing Ge and O atoms respectively and corroborates the rutile structure. The a and c lattice parameters are 4.40 Å and 2.86 Å respectively. (d) X-ray diffraction or r-GeO_2 single crystals with the largest-area facet oriented out-of-plane. (e) X-ray rocking curve of r-GeO_2 110 diffraction peak compared with the 1$\bar{1}$02 peak of a Al_2O_3 single crystal substrate purchased at MTI corporation.

Figure 3.13: z

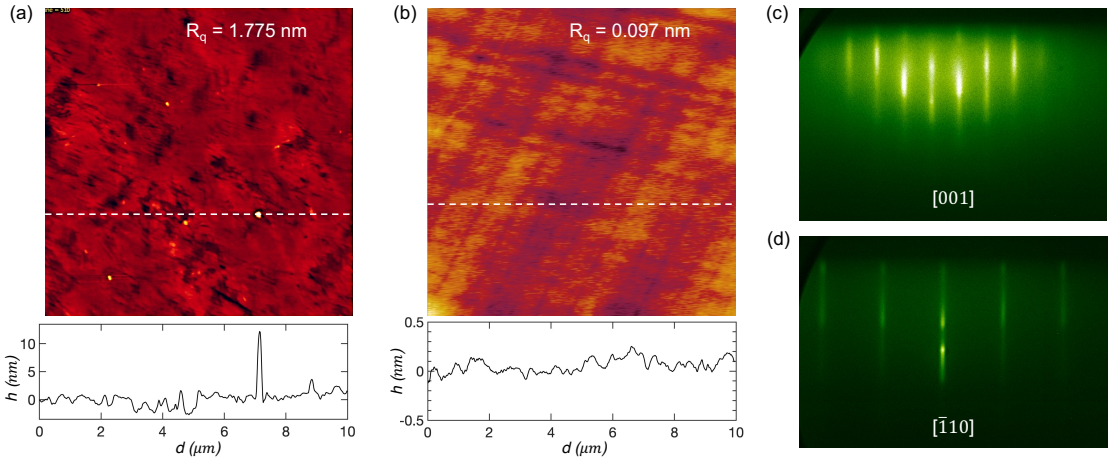

or (c) and [$\bar{1}$10] for (d).](a) Atomic force microscopy scanning of as-grown r-GeO_2 single crystals. (b) Atomic force microscopy scanning of r-GeO_2 single crystal substrates after mechanical polishing. The height profile is obtained for the white dashed line in the scanning image. (c-d) RHEED patterns observed for the polished, post-annealed surface of r-GeO_2 single-crystal substrate showing a highly crystalline surface after preparation. The surface orientation is (110) and the azimuth is [001] for (c) and [$\bar{1}$10] for (d).

Figure 3.14: f

∼4 nm depth along with small (∼12 nm diameter) particles. On the other hand, after mechanical polishing, the surface roughness less than 0.1 nm is achieved, and surface particles are removed, indicating that the surface roughness is effectively reduced by mechanical polishing. We also observed a single-crystalline surface for the polished surface by RHEED. Fig. 3.14 (c-d) shows the RHEED patterns of the (110) plane of r-GeO_2 crystals after polishing and post-annealing, recorded at two different azimuths of [001] for (c) and [$\bar{1}$10] for (d). The RHEED patterns show a streaky diffraction pattern and clear anisotropy consistent with the (110) rutile surface structure, indicating the feasibility of our r-GeO_2 single crystals for epitaxial film growth substrates.

3.7 Conclusion

In summary, we assessed the promise of r-GeO_2 for power electronics applications. First-principles calculations predicted shallow ionization energies for donors and the

ionization energy of 0.45 eV for Al acceptors. Calculated electron and hole mobilities of 289 cm^2 V^{-1} s^{-1} and 28 cm^2 V^{-1} s^{-1} are remarkably close to the state-of-the-art semiconductors such as GaN. Thermal conductivity of 51 W m^{-1} K^{-1} is experimentally measured for polycrystalline, bulk r-GeO_2, which can overcome the thermal challenge of β-Ga_2O_3. Utilizing a novel preoxidized source in molecular beam epitaxy, the first synthesis of single-crystalline r-GeO_2 thin film on (Sn,Ge)O_2/SnO_2-buffered sapphire substrates is found ina narrow range of conditions that balance GeO (g) adsorption/desorption. The demonstration of r-GeO_2 single crystal substrates provides the opportunity to grow homoepitaxial r-GeO_2 thin film. Our work motivates further exploration of r-GeO_2 as an alternative UWBG semiconductor that can advance the power electronics technology.

Reproduced from [S. Chae, J. Lee, K. A. Mengle, J. T. Heron and E. Kioupakis, Appl. Phys. Lett. 114, 102104 (2019).], [S. Chae, K. A. Mengle, R. Lu, A. Olvera, N. Sanders, J. Lee, P. F. P. Poudeu, J. T. Heron and E. Kioupakis, Appl. Phys. Lett. 117, 102106 (2020).], [S. Chae, H. Paik, N. M. Vu, E. Kioupakis and J. T. Heron, Appl. Phys. Lett. 117, 072105 (2020).], [K. Bushick, K. A. Mengle, S. Chae and Kioupakis, Appl. Phys. Lett. 117, 182104 (2020).], [S. Chae, K. Mengle, K. Bushick, J. Lee, N. Sanders, Z. Deng, Z. Mi, P. F. P. Poudeu, H. Paik, J. T. Heron and E. Kioupakis, Appl. Phys. Lett. 118, 260501 (2021).], with the permission of AIP Publishing.

CHAPTER IV

Summary and Future Work

4.1 Summary

Semiconductors have unique electrical properties that distinguish themselves from metals and insulators. Their electrical conductivity can be tuned by doping or electrostatic fields, which is essential for microelectronic devices. Silicon is the traditional semiconductor material that has governed modern microelectronic technology, however, silicon based microelectronic devices are not fast, dense, and efficient enough to keep up with the growing demands for high performance computing in AI era. As semiconductors with wider band gap have higher breakdown voltages which allow devices to operate at high power and high speed, ultra-wide-band-gap (UWBG, $>$ 3.4 eV) semiconductors have emerged as potential solutions for energy-efficient high power and RF electronics. In addition to ultra-wide-band-gap, high mobility and high thermal conductivity contribute to high power conversion efficiency and ambipolar dopability allows wide-range device applications. Common UWBG semiconductors such as AlGaN/AlN, diamond, and β-Ga_2O_3 all suffer from intrinsic doping and/or thermal management challenges, which motivates to search for novel UWBG materials with superior properties.

In section 2, through a high-throughput survey of wide-band-gap materials combined with first-principles calculations, it is found that the key material parameter

Table 4.1: Baliga's figure of merit (BFOM = $\frac{1}{4}\epsilon_0\mu E_c^3$) and thermal conductivity for silicon and common ultra-wide-band-gap semiconductors. ϵ_0 is the static dielectric constant, μ_e/μ_h is the electron/hole mobility at room temperature, E_c is the dielectric breakdown field predicted based on the breakdown vs band gap relation established by Ref.[17], E_d/E_a is the donor/acceptor ionization energy, and κ is the thermal conductivity at room temperature. μ_e/μ_h is the experimental maximum realized values for all materials except r-GeO_2, whereas μ_e/μ_h of r-GeO_2 is phonon-limited mobility calculated by the density functional theory.

Materials	ϵ_0	μ_e/μ_h (**cm^2 V^{-1} s^{-1}**)	E_c (**MV cm^{-1}**)	E_d/E_a (**eV**)	**n-/p-BFOM** (**10^6 V^2 Ω^{-1} cm^{-2}**)	κ (**W m^{-1} K^{-1}**)
Si	11.9[117]	1240[118]/ 450[119]	0.3[17]	0.04/ 0.05[120]	8.8/3.2[83]	130[120]
4H-SiC	9.7[118]	980[118]/ 120[120]	2.5[17]	0.05/ 0.19[121]	3300/404[83]	370[1]
GaN	10.4[122]	1000[123]/ 31[87]	3.3[17]	0.04/ 0.21	8300/257[83]	253[1]
β-Ga_2O_3	10.0[122]	184[86]/-	6.4[17]	0.04[124]/ 1.1[125]	6300[83]/-	11; 27[44]
AlN	9.1[126]	426[127]/ 14[128]	15.4[1]	0.25[129]/ 1.4[128]	336000/ 11000[1]	286; 319[130]
c-BN	7.1[131]	200[131]/ 500[132]	17.5[1]	0.15[133]/ 0.24[134]	27800/ 695000[1]	1600[135]
diamond	5.7[120]	1060/ 2000[39]	13.0[1]	0.57/ 0.38[39]	294000/ 554000[1]	2290-3450[39]
r-GeO_2	14.5($\perp$c)[136] 12.2($\parallel$c)[136]	244/27[83] 377/29[83]	7.0[83]	<0.04/ 0.45[64]	27000/3000[83] 35000/2700[83]	51[90]

that distinguishes semiconductors from insulators is not their band gap, but their light carrier effective mass. It is also found that small cation radius, densely packed crystal structure, and s-orbital characteristics of conduction band enable the combination of wide band gap and light carrier effective mass, and find the extreme limits to semiconductor band gap. This leads to the discovery of materials having a band gap even wider than canonical insulators but having a small effective mass that allows semiconductivity such as MgO (7.47 eV) and rs-BeO (11.6 eV), demonstrating that the magnitude of band gap can no longer be a criterion to distinguish semiconductors from insulators.

In section 3, we identify that rutile GeO_2 (r-GeO_2) is an unexplored, but promising UWBG semiconductor that can solve the challenges of the emerging UWBG materials (Table 4.1). Based on density functional theory calculation, r-GeO_2 is predicted to be ambipolarly doped and have high electron and hole mobilities (up to 377 cm^2 V^{-1} s^{-1} and 29 cm^2 V^{-1} s^{-1}), which leads to high BFOM. r-GeO_2 has high thermal conductivity of 51 W m^{-1} K^{-1} that can solve the thermal management issue of β-Ga_2O_3. The subsequent realization of single-crystalline r-GeO_2 thin films by molecular beam epitaxy as well as single-crystalline r-GeO_2 substrates by flux synthesis provide the opportunity to realize r-GeO_2 for electronic applications.

4.2 Future work

4.2.1 High-throughput discovery of novel UWBG semiconductors using materials informatics

In section 2, a theoretical framework is developed to identify novel UWBG semiconductors and find the limit to semiconductor band gap. However, this work focuses on finding candidate materials from binary oxides with simple crystal structure. The future work will be to expand the compositional space of materials to include complex oxides and other ceramic materials and to search for UWBG semiconductors with enhanced mobility and doping properties that can advance energy efficiency of power electronics.

Data-mining and machine-learning algorithms have allowed high-throughput materials discovery based on materials database. High-throughput computation combined with open-access data allows a broad computational survey of over 130,000 inorganic compounds to identify novel semiconductors. To screen promising semiconductors, descriptors such as ionization energy and polaron binding energy can be used which can be calculated given by the effective mass and dielectric constant

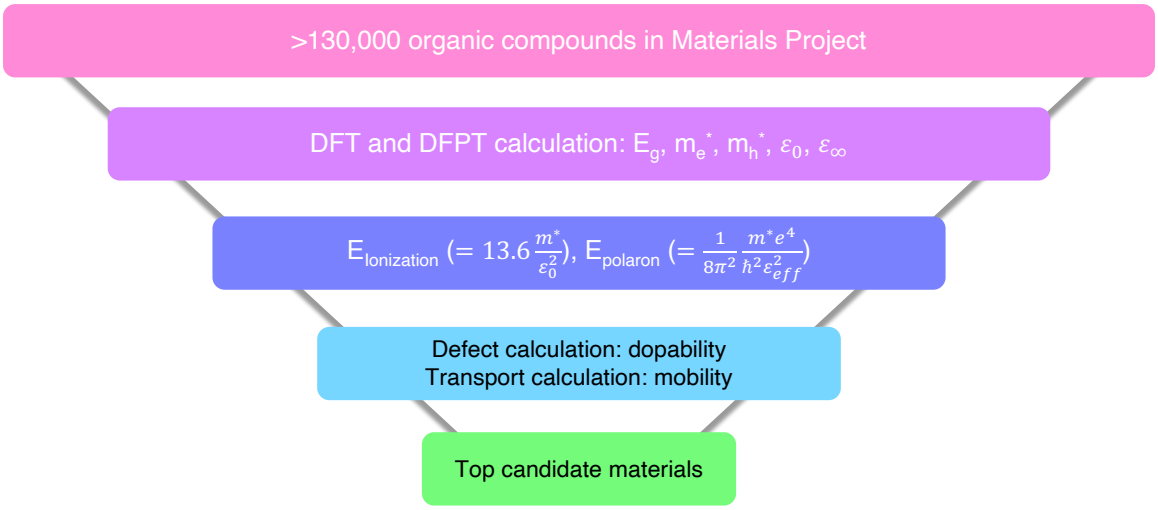

Figure 4.1: High-throughput survey of novel UWBG semiconductors

data precomputed by DFT and DFPT and stored in Materials Project. For materials identified to have shallow ionization energy and negligible polaron binding energy, atomistic calculations can be performed to predict charge compensation and mobility, and materials with dopability and high mobility are further screened. Also, machine-learning algorithms can be employed to reveal complex relationships between variables in database (e.g., relationship between chemical/structural properties and semiconductivity), which can be used to guide to invent new materials. Experiment can then be investigated only for the most promising material candidates identified which drastically expedites findings of new materials. The workflow of high-throughput discovery of novel UWBG semiconductors is summarized in Figure 4.1.

4.2.2 Doping of r-GeO_2 thin-films

Section 3 illustrates the compelling material properties of r-GeO_2 that can be exploited for high-power or RF electronics and showcases the fabrication of high-quality r-GeO_2 thin-films and single-crystalline substrates. Future research work remains for the experimental demonstration of n-type and p-type doped r-GeO_2 thin films and electrical characterization to realize r-GeO_2 based power electronics. The successful

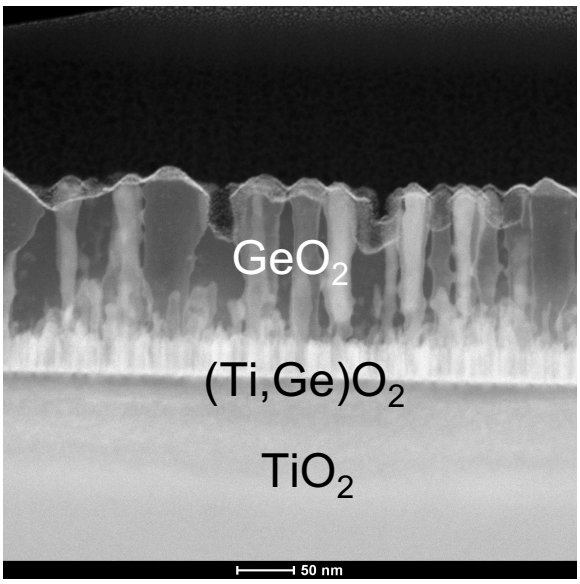

Figure 4.2: Transmission electron microscopy image of r-GeO_2 thin films grown on (Ti,Ge)O_2-buffered TiO_2 (001) substrates

demonstration of doped r-GeO_2 thin films will open new avenues in power electronic research that may lead to improved energy efficiency.

Based on initial findings, r-GeO_2 thin films grown on heteroepitaxial substrates are insulating and it is attributed to the microsctructure of the films. r-GeO_2 thin films prefer columnar growth in (001) and (101) orientations. The cross-sectional image of transmission electron microscopy in Figure 4.2 shows the columnar grains of r-GeO_2 thin films. It is possible that carrier mobility is limited at the columnar grain boundaries. In addition, the large lattice misfit ($> 4\%$) between substrates and thin films leads to the formation of a large density of dislocations which consume free carriers and act as scattering centers.

Doping of r-GeO_2 thin films is expected to be achieved by improving the quality of microsctructure through layer-by-layer growth. To promote layer-by-layer growth, different growth orientations or substrates with reduced lattice mismatch need to be explored. For example, layer-by-layer growth can be promoted on (110) orientation as (110) plane has the lowest surface energy and has less number of dangling bond exposed to the surface (Figure 4.3(c)) as compared to (001) and (101) orientations

where the surface contains larger number of dangling bonds (Figure 4.3(a) and (b), respectively). In addition, the availability of r-GeO_2 substrates (Figure 3.13) now allows exploration of homoepitaxial thin film growth of r-GeO_2, which may allow better quality of r-GeO_2 thin films with significantly suppressed dislocations.

For doping of r-GeO_2, both n-type and p-type doping needs to be demonstrated. According to density functional theory calculation in Figures 3.2 and 3.3, candidate n-type dopants are Sb, As, and F and candidate p-type dopants are Al, Ga, and In. Finally, r-GeO_2 p-n homojunction can be fabricated as the geometric structure illustrated in Figure 4.4, which is integral in semiconductor diodes or LED lighting applications.

4.2.3 Band enginnering of rutile semiconductor alloys

Alloying is a power method to tailor the band structure of a semiconductor to produce desired electronic and optoelectronic property for device needs. For example, semiconductor alloys are formed to tailor a band gap for desirable wavelength of light emission in optoelectronics or to create a material with a proper lattice constant to match with an available substrate. Though alloys of III-V compounds such as InGaAlAs or group IV compounds such as SiGe have made significant contributions in high speed electronics and optoelectronics, there is a lack of study in rutile oxide semiconductor system.

Particularly, alloys made from rutile SiO_2, GeO_2, and SnO_2 can span a large range of band gap (from 3.7 eV to 8.9 eV), remaining direct throughout the composition range, and have small effective mass arising from s-orbital characteristics of conduction bands (Figure 4.5(a)). As these compounds share similar band features, the band gap and effective mass of the alloy (A_xB_{1-x}) can be reasonably approximated

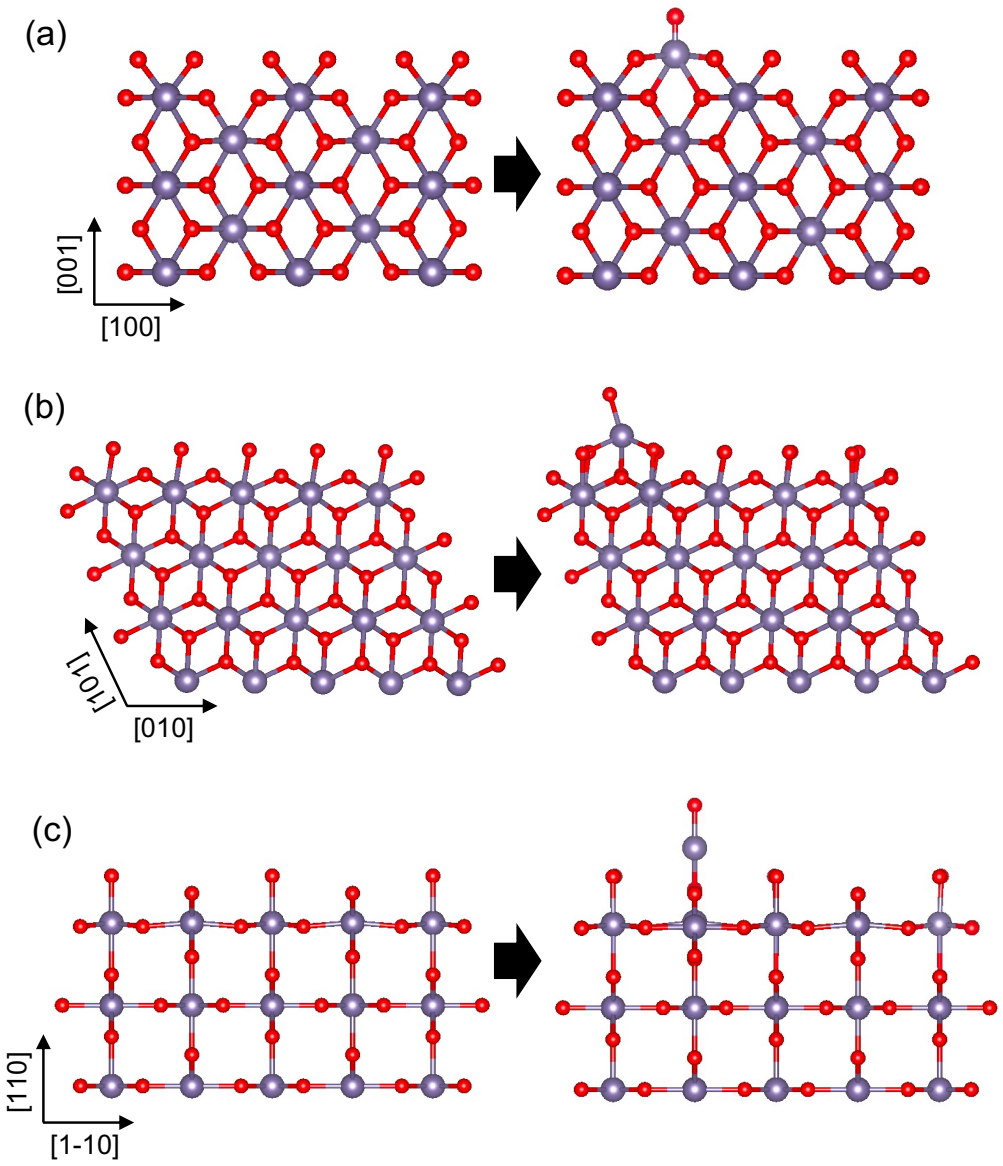

Figure 4.3: Side view of r-GeO_2 atomic structure for various surface orientation: (a) (001), (b) (101), and (c) (110)

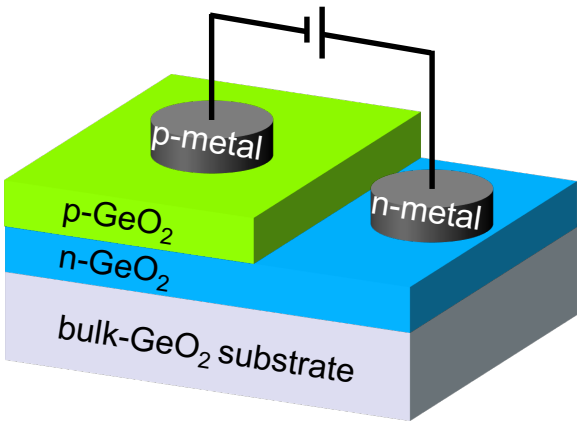

Figure 4.4: Schematic of r-GeO_2 p-n homojunctions

by using virtual crystal approximation:

$$E_g^{alloy} = xE_g^A + (1-x)E_g^B + cx^2 \tag{4.1}$$

$$\frac{1}{m^*_{alloy}} = \frac{x}{m^*_A} + \frac{1-x}{m^*_B} \tag{4.2}$$

where E_g^{alloy} is the band gap of alloy, m^*_{alloy} is the effective mass of alloy, and c is a bowing parameter arising from the increasing disorder due to the alloying. The $SiO_2/GeO_2/SnO_2$ alloy system exhibits a band gap tunable in the ultra-wide-band-gap range as well as light electron effective masses (Figure 4.5(a-b)), making them desirable for high power generation electronic applications.

The initial finding suggests that single-crystalline thin films of $Sn_{1-x}Ge_xO_2$ alloy can be synthesized on bare sapphire substrates up to x = 0.5 using molecular beam epitaxy. Figure 4.6(a) shows the x-ray diffraction of $Sn_{0.5}Ge_{0.5}O_2$ thin films. The out-of-plane lattice parameter is 2.560 Å, suggesting that the alloy approximately follows the Vegard's law. We find that the band gap is tunable by alloying: a band gap of 4.05 eV was measured for $Sn_{0.5}Ge_{0.5}O_2$ thin films by UV-vis absorption measurement (Figure 4.6(b)). It is also demonstrate that the thin films of alloys can be efficiently doped by Sb dopant. The carrier concentration of thin films can be controlled from 5×10^{18} cm^{-3} to 5×10^{19} cm^{-3} by tuning the Sb flux with the cell temperature

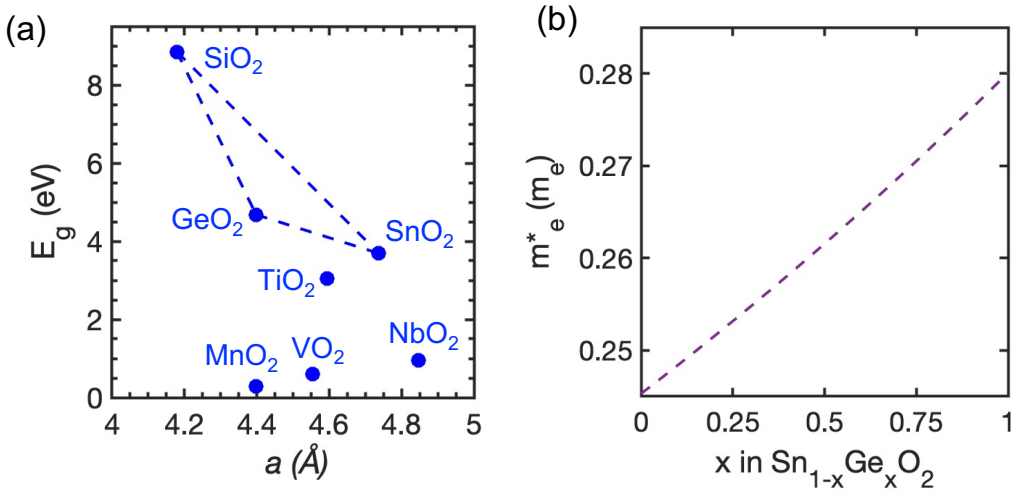

Figure 4.5: (a) The band gap and lattice parameter of rutile binary oxides (b) Predicted effective mass of (Sn,Ge)O_2 alloys

(Figure 4.6(c)).

This strategy can be expanded to the whole composition range of SiO_2/GeO_2/SnO_2 alloy system to further increase the band gap and obtain efficient doping. As the lattice constant of commercial rutile substrates (e.g., TiO_2 and MgF_2) have a lattice match with $GeSnO_2$ or $SiSnO_2$ alloy, film dislocation is expected to suppress and doping property can be improved for these alloys.

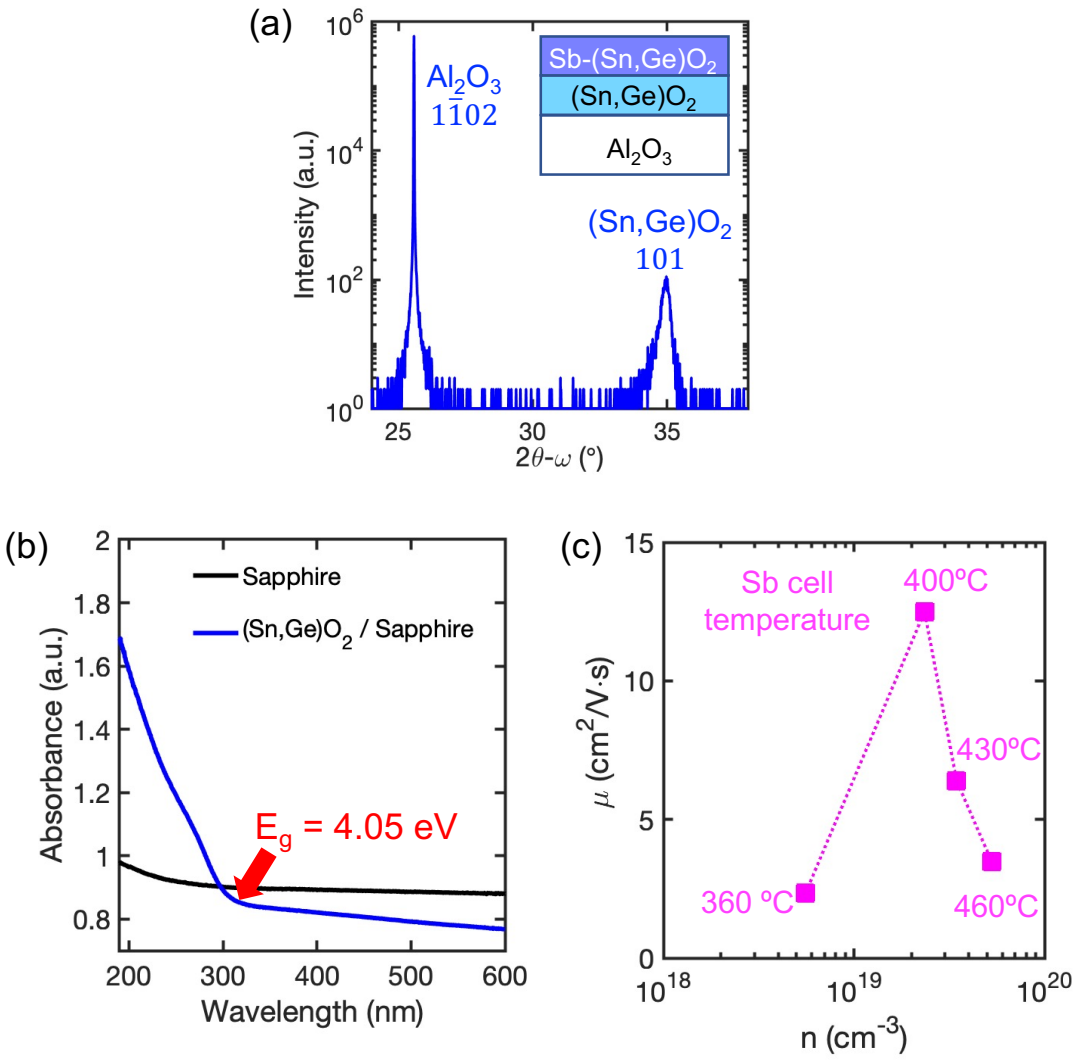

Figure 4.6: (a) X-ray diffraction of r-$Sn_{0.5}Ge_{0.5}O_2$ single crystalline thin films grown on R-plane sapphire substrates by molecular beam epitaxy (b) UV-Vis spectroscopy of $Sn_{0.5}Ge_{0.5}O_2$ thin films on sapphire substrates. The band gap of $Sn_{0.5}Ge_{0.5}O_2$ thin films is determined to be 4.05 eV. (c) The mobility versus carrier concentration of $Sn_{0.5}Ge_{0.5}O_2$ thin films with varied Sb dopant concentration characterized by hall measurement. To tune the concentration of Sb dopant, we varied Sb flux by using Sb cell temperature from 360°C to 460°C

BIBLIOGRAPHY

BIBLIOGRAPHY

[1] J. Y. Tsao, S. Chowdhury, M. A. Hollis, D. Jena, N. M. Johnson, K. A. Jones, R. J. Kaplar, S. Rajan, C. G. Van de Walle, E. Bellotti, C. L. Chua, R. Collazo, M. E. Coltrin, J. A. Cooper, K. R. Evans, S. Graham, T. A. Grotjohn, E. R. Heller, M. Higashiwaki, M. S. Islam, P. W. Juodawlkis, M. A. Khan, A. D. Koehler, J. H. Leach, U. K. Mishra, R. J. Nemanich, R. C. Pilawa-Podgurski, J. B. Shealy, Z. Sitar, M. J. Tadjer, A. F. Witulski, M. Wraback, and J. A. Simmons, "Ultrawide-Bandgap Semiconductors: Research Opportunities and Challenges," *Advanced Electronic Materials*, vol. 4, no. 1, pp. 1–49, 2018.

[2] G. F. Harrington and J. Santiso, "Back-to-Basics tutorial: X-ray diffraction of thin films," *Journal of Electroceramics*, no. 0123456789, 2021. [Online]. Available: https://doi.org/10.1007/s10832-021-00263-6

[3] S. Strite, "GaN, AlN, and InN: A review," *Journal of Vacuum Science Technology B: Microelectronics and Nanometer Structures*, vol. 10, no. 4, p. 1237, 1992.

[4] Y. Taniyasu, M. Kasu, and T. Makimoto, "Increased electron mobility in n -type Si-doped AlN by reducing dislocation density," *Applied Physics Letters*, vol. 89, no. 18, p. 182112, 2006.

[5] E. X. Zhang, C. X. Zhang, D. M. Fleetwod, R. D. Schrimpf, S. Dhar, S. H. Ryu, X. Shen, and S. T. Pantelides, "Bias-temperature instabilities in 4H-SiC metal-oxide-semiconductor capacitors," *IEEE Transactions on Device and Materials Reliability*, vol. 12, no. 2, pp. 391–398, 2012.

[6] E. Mollwo, G. Müller, and P. Wagner, "Energetische lage des Cu-akzeptorniveaus in ZnO-Einkristallen," *Solid State Communications*, vol. 13, no. 8, pp. 1283–1287, 1973.

[7] M. Nagasawa, S. Shionoya, and S. Makishima, "Electron effective mass of SnO2," *J. Phys. Soc. JAPAN*, vol. 20, p. 1093, 1965.

[8] A. Bally, "Electronic properties of nano-crystalline titanium dioxide thin films," vol. 2094, p. 140, 1999. [Online]. Available: http://biblion.epfl.ch/EPFL/theses/1999/2094/EPFL_TH2094.pdf

[9] D.-P. Frank Herklotz, "Hydrogen-related defects in ZnO and TiO2," *Dissertation*, p. 11, 2011.

[10] O. Mishima, J. Tanaka, S. Yamaoka, and O. Fukunaga, "High-temperature cubic boron nitride p-n junction diode made at high pressure," *Science*, vol. 238, no. 4824, pp. 181–183, 1987.

[11] A. T. Neal, S. Mou, S. Rafique, H. Zhao, E. Ahmadi, J. S. Speck, K. T. Stevens, J. D. Blevins, D. B. Thomson, N. Moser, K. D. Chabak, and G. H. Jessen, "Donors and deep acceptors in β-Ga2O3," *Applied Physics Letters*, vol. 113, no. 6, pp. 1–6, 2018. [Online]. Available: http://dx.doi.org/10.1063/1.5034474

[12] J. J. Lander, "Reactions of Lithium as a donor and an acceptor in ZnO," *Journal of Physics and Chemistry of Solids*, vol. 15, no. 3-4, pp. 324–334, 1960.

[13] Y. Seki, Y. Hoshino, and J. Nakata, " Remarkable p -type activation of heavily doped diamond accomplished by boron ion implantation at room temperature and subsequent annealing at relatively low temperatures of 1150 and 1300 °C ," *Applied Physics Letters*, vol. 115, no. 7, p. 072103, 2019.

[14] T. Matsuda, K. Yamada, Y. Shibata, H. Miura, and K. Sugiyama, "Doping effect of sodium on γ-irradiated magnesium oxide," *Journal of the Chemical Society, Faraday Transactions 1: Physical Chemistry in Condensed Phases*, vol. 83, no. 10, pp. 3107–3114, 1987.

[15] W. H. Sio, C. Verdi, S. Poncé, and F. Giustino, "Ab initio theory of polarons: Formalism and applications," *Physical Review B*, vol. 99, no. 23, pp. 1–21, 2019.

[16] Z. Hiroi, "Structural instability of the rutile compounds and its relevance to the metal-insulator transition of VO2," *Progress in Solid State Chemistry*, vol. 43, no. 1-2, pp. 47–69, 2015. [Online]. Available: http://dx.doi.org/10.1016/j.progsolidstchem.2015.02.001

[17] M. Higashiwaki, K. Sasaki, A. Kuramata, T. Masui, and S. Yamakoshi, "Gallium oxide (Ga 2O 3) metal-semiconductor field-effect transistors on single-crystal β-Ga 2O 3 (010) substrates," *Applied Physics Letters*, vol. 100, p. 013504, 2012.

[18] K. Kita, S. Suzuki, H. Nomura, T. Takahashi, T. Nishimura, and A. Toriumi, "Direct evidence of GeO volatilization from GeO2/Ge and impact of its suppression on GeO2/Ge metal-insulator-semiconductor characteristics," *Japanese Journal of Applied Physics*, vol. 47, no. 4 PART 2, pp. 2349–2353, 2008.

[19] W. D. Callister, *Materials Science and Engineering: An Introduction*, 7th ed. Wiley, 7th edition, pp.730, 2007.

[20] A. Brinkman, M. Huijben, M. Van Zalk, J. Huijben, U. Zeitler, J. C. Maan, W. G. Van Der Wiel, G. Rijnders, D. H. Blank, and H. Hilgenkamp, "Magnetic effects at the interface between non-magnetic oxides," *Nature Materials*, vol. 6, no. 7, pp. 493–496, 2007.

[21] S. Thiel, G. Hammerl, A. Schmehl, C. W. Schneider, and J. Mannhart, "Tunable quasi-two-dimensional electron gases in oxide heterostructures," *Science*, vol. 313, pp. 1942–1946, 2006.

[22] H. Lee, N. Campbell, J. Lee, T. J. Asel, T. R. Paudel, H. Zhou, J. W. Lee, B. Noesges, J. Seo, B. Park, L. J. Brillson, S. H. Oh, E. Y. Tsymbal, M. S. Rzchowski, and C. B. Eom, "Direct observation of a two-dimensional hole gas at oxide interfaces," *Nature Materials*, vol. 17, no. 3, pp. 231–236, 2018.

[23] J. Bardeen and W. Brattain, "Three-electrode circuit element utilizing semiconductive materials," p. United States Patent 2524035, 1950.

[24] M. M. Atalla, T. Tannenbaum, and E. J. Scheibner, "Stabilization of silicon surfaces by thermally grown oxides," *The Bell System Technical Journal*, vol. 38, no. 3, pp. 749–783, 1959.

[25] C.-T. Sah, "Evolution of the MOS transistors," *Proceedings of the IEEE*, vol. 76, no. 10, p. 1293, 1988.

[26] G. M. Moore, "Cramming more components onto integrated circuits," *Electronics*, vol. 38, no. 8, 1965. [Online]. Available: https://newsroom.intel.com/wp-content/uploads/sites/11/2018/05/moores-law-electronics.pdf

[27] R. Dupuis, "An introduction to the development of the semiconductor laser," *IEEE Journal of Quantum Electronics*, vol. 23, no. 6, pp. 651–657, 1987.

[28] H. Morkoc and P. M. Solomon, "The HEMT: A superfast transistor: An experimental GaAs-AlGaAs device switches in picoseconds and generates little heat. This is just what supercomputers need," *IEEE Spectrum*, vol. 21, no. 2, pp. 28–35, 1984.

[29] W. Shockley, "Circuit element utilizing semiconductive material," pp. United States Patent 2,569,347, 1951.

[30] S. Nakamura and M. R. Krames, "History of gallium-nitride-based light-emitting diodes for illumination," *Proceedings of the IEEE*, vol. 101, no. 10, pp. 2211–2220, 2013.

[31] B. J. Baliga, "Semiconductors for high-voltage, vertical channel field-effect transistors," *Journal of Applied Physics*, vol. 53, no. 3, pp. 1759–1764, 1982.

[32] ——, "Power semiconductor device figure of merit for high-frequency applications," *IEEE Electron Device Letters*, vol. 10, no. 10, pp. 455–457, 1989.

[33] U. K. Mishra and J. Singh, *Semiconductor device physics and design*. Springer, 2008.

[34] E. Johnson, "Physical limitations on frequency and power parameters of transistors," *1958 IRE International Convention Record*, pp. 27–34, 1965.

[35] M. Kneissl, Z. Yang, M. Teepe, C. Knollenberg, O. Schmidt, P. Kiesel, N. M. Johnson, S. Schujman, and L. J. Schowalter, "Ultraviolet semiconductor laser diodes on bulk AlN," *Journal of Applied Physics*, vol. 101, no. 12, p. 123103, 2007.

[36] C. G. Van de Walle, C. Stampfl, J. Neugebauer, M. D. McCluskey, and N. M. Johnson, "DOPING OF AlGaN ALLOYS," *MRS Internet J. Nitride Semicond. Res.*, vol. 4S1, p. G10.4, 1999.

[37] Y. Liang and E. Towe, "Progress in efficient doping of high aluminum-containing group III-nitrides," *Appl. Phys. Rev.*, vol. 5, p. 011107, 2018. [Online]. Available: http://dx.doi.org/10.1063/1.5009349

[38] N. Pant, Z. Deng, and E. Kioupakis, " High electron mobility of Al x Ga 1 x N evaluated by unfolding the DFT band structure ," *Applied Physics Letters*, vol. 117, no. 24, p. 242105, 2020.

[39] N. Donato, N. Rouger, J. Pernot, G. Longobardi, and F. Udrea, "Diamond power devices: State of the art, modelling, figures of merit and future perspective," *Journal of Physics D: Applied Physics*, vol. 53, no. 9, p. 093001, 2020.

[40] M.-A. Pinault, J. Barjon, T. Kociniewski, F. Jomard, and J. Chevallier, "The n-type doping of diamond : Present status and pending questions," *Physica B*, vol. 401-402, pp. 51–56, 2007.

[41] J. P. Goss, P. R. Briddon, M. J. Rayson, S. J. Sque, and R. Jones, "Vacancy-impurity complexes and limitations for implantation doping of diamond," *Physical Review B*, vol. 72, p. 035214, 2005.

[42] K. Sasaki, A. Kuramata, T. Masui, E. G. Víllora, K. Shimamura, and S. Yamakoshi, "Device-quality β-Ga 2o 3epitaxial films fabricated by ozone molecular beam epitaxy," *Applied Physics Express*, vol. 5, no. 3, p. 035502, 2012.

[43] N. Ueda, H. Hosono, R. Waseda, and H. Kawazoe, "Synthesis and control of conductivity of ultraviolet transmitting β-Ga2O3 single crystals," *Applied Physics Letters*, vol. 70, no. 26, pp. 3561–3563, 1997.

[44] Z. Guo, A. Verma, X. Wu, F. Sun, A. Hickman, T. Masui, A. Kuramata, M. Higashiwaki, D. Jena, and T. Luo, "Anisotropic thermal conductivity in single crystal β-gallium oxide," *Applied Physics Letters*, vol. 106, no. 11, p. 111909, 2015. [Online]. Available: http://dx.doi.org/10.1063/1.4916078

[45] K. A. Mengle and E. Kioupakis, "Vibrational and electron-phonon coupling properties of β-Ga ¡sub¿2¡/sub¿ O ¡sub¿3¡/sub¿ from first-principles calculations: Impact on the mobility and breakdown field," *AIP Advances*, vol. 9, no. 1, p. 015313, 2019.

[46] P. Hohenberg and W. Kohn, "Inhomogeneous electron gas," *Physical Review*, vol. 136, no. 4, p. B864, 1964.

[47] C. Freysoldt, B. Grabowski, T. Hickel, J. Neugebauer, G. Kresse, A. Janotti, and C. G. V. D. Walle, "First-principles calculations for point defects in solids," *Reviews of Modern Physics*, vol. 86, no. March, pp. 253–305, 2014.

[48] C. Freysoldt, J. Neugebauer, and C. G. Van De Walle, "Fully Ab initio finite-size corrections for charged-defect supercell calculations," *Physical Review Letters*, vol. 102, p. 016402, 2009.

[49] M. Yasaka, "X-ray thin-film measurement techniques," *The Rigaku Journal*, vol. 26, no. 2, pp. 1–9, 2010.

[50] G. Kresse and J. Hafner, "Ab initio molecular dynamics for liquid metals," *Physical Review B*, vol. 47, no. 1, pp. 558–561, 1993.

[51] G. Kresse and J. Furthmüller, "Efficiency of ab-initio total energy calculations for metals and semiconductors using a plane-wave basis set," *Computational Materials Science*, vol. 6, no. 1, pp. 15–50, 1996.

[52] J. Heyd, G. E. Scuseria, and M. Ernzerhof, "Hybrid functionals based on a screened Coulomb potential," *Journal of Chemical Physics*, vol. 118, no. 18, pp. 8207–8215, 2003.

[53] S. Baroni, S. D. Gironcoli, A. D. Corso, S. Scuola, I. Superiore, I. Istituto, F. Materia, I. Trieste, and P. Giannozzi, "perturbation theory," *Reviews of Modern Physics*, vol. 73, no. April, pp. 515–562, 2001.

[54] C. G. Van De Walle and R. M. Martin, "Theoretical study of band offsets at semiconductor interfaces," *Physical Review B*, vol. 35, no. 15, pp. 8154–8165, 1987.

[55] D. M. Ceperley and B. J. Alder, "Ground State of the Electron Gas by a Stochastic Method," *Physical Review Letters*, vol. 45, no. 7, pp. 566–569, 1980.

[56] P. Giannozzi, S. Baroni, N. Bonini, M. Calandra, R. Car, C. Cavazzoni, D. Ceresoli, G. L. Chiarotti, M. Cococcioni, I. Dabo, A. D. Corso, S. D. Gironcoli, U. Gerstmann, C. Gougoussis, A. Kokalj, M. Lazzeri, L. Martin-samos, N. Marzari, F. Mauri, R. Mazzarello, S. Paolini, A. Pasquarello, L. Paulatto, and C. Sbraccia, "Q UANTUM ESPRESSO : a modular and open-source software project for quantum simulations of materials," *Journal of Physics Condensed Matter*, vol. 21, p. 395502, 2009.

[57] M. S. Hybertsen and S. G. Louie, "Electron correlation in semiconductors and insulators: Band gaps and quasiparticle energies," *Physical Review B*, vol. 34, no. 8, pp. 5390–5413, 1986.

[58] J. Deslippe, G. Samsonidze, D. A. Strubbe, M. Jain, M. L. Cohen, and S. G. Louie, "BerkeleyGW: A massively parallel computer package for the calculation of the quasiparticle and optical properties of materials and nanostructures,"

Computer Physics Communications, vol. 183, no. 6, pp. 1269–1289, 2012. [Online]. Available: http://dx.doi.org/10.1016/j.cpc.2011.12.006

[59] J. Deslippe, G. Samsonidze, M. Jain, M. L. Cohen, and S. G. Louie, "Coulomb-hole summations and energies for GW calculations with limited number of empty orbitals: A modified static remainder approach," *Physical Review B*, vol. 87, no. 16, p. 165124, 2013.

[60] S. Poncé, E. R. Margine, C. Verdi, and F. Giustino, "EPW: Electron–phonon coupling, transport and superconducting properties using maximally localized Wannier functions," *Computer Physics Communications*, vol. 209, pp. 116–133, 2016.

[61] F. Macheda and N. Bonini, "Magnetotransport phenomena in p -doped diamond from first principles," *Physical Review B*, vol. 98, no. 20, p. 201201, 2018.

[62] S. Poncé, E. R. Margine, and F. Giustino, "Towards predictive many-body calculations of phonon-limited carrier mobilities in semiconductors," *Physical Review B*, vol. 97, no. 12, p. 121201, 2018.

[63] A. Segura, J. A. Sans, D. Errandonea, D. Martinez-García, and V. Fages, "High conductivity of Ga-doped rock-salt ZnO under pressure: Hint on deep-ultraviolet-transparent conducting oxides," *Applied Physics Letters*, vol. 88, no. 1, pp. 1–4, 2006.

[64] S. Chae, J. Lee, K. A. Mengle, J. T. Heron, and E. Kioupakis, "Rutile GeO2: An ultrawide-band-gap semiconductor with ambipolar doping," *Applied Physics Letters*, vol. 114, no. 10, p. 102104(5), 2019.

[65] J. B. Varley, A. Janotti, C. Franchini, and C. G. Van De Walle, "Role of self-trapping in luminescence and p-type conductivity of wide-band-gap oxides," *Physical Review B*, vol. 85, no. 8, p. 081109(R), 2012.

[66] C. Stampfl, J. Neugebauer, and C. G. Van De Walle, "Doping of AlxGa1-xN alloys," *Materials Science and Engineering B: Solid-State Materials for Advanced Technology*, vol. 59, no. 1-3, pp. 253–257, 1999.

[67] C. G. Van de Walle, "DX-center formation in wurtzite and zinc-blende," *Physical Review B - Condensed Matter and Materials Physics*, vol. 57, no. 4, pp. R2033–R2036, 1998.

[68] M. M. Tardío, R. Ramírez, R. González, and Y. Chen, "P-type semiconducting properties in lithium-doped MgO single crystals," *Physical Review B - Condensed Matter and Materials Physics*, vol. 66, no. 13, pp. 1–8, 2002.

[69] A. Zunger, "Practical doping principles," *Applied Physics Letters*, vol. 83, no. 1, pp. 57–59, 2003.

[70] Z. Bryan, I. Bryan, B. E. Gaddy, P. Reddy, L. Hussey, M. Bobea, W. Guo, M. Hoffmann, R. Kirste, J. Tweedie, M. Gerhold, D. L. Irving, Z. Sitar, and R. Collazo, "Fermi level control of compensating point defects during metalorganic chemical vapor deposition growth of Si-doped AlGaN," *Applied Physics Letters*, vol. 105, no. 22, p. 222101, 2014. [Online]. Available: http://dx.doi.org/10.1063/1.4903058

[71] A. Pandey, X. Liu, Z. Deng, W. J. Shin, D. A. Laleyan, K. Mashooq, E. T. Reid, E. Kioupakis, P. Bhattacharya, and Z. Mi, "Enhanced doping efficiency of ultrawide band gap semiconductors by metal-semiconductor junction assisted epitaxy," *Physical Review Materials*, vol. 3, p. 053401, 2019.

[72] S. Nakamura, T. Mukai, M. Senoh, and N. Iwasa, "Thermal annealing effects on p-type Mg-doped GaN films," *Jpn. J. Appl. Phys.*, vol. 31, pp. 139–142, 1992.

[73] A. W. Laubengayer and D. S. Morton, "Germanium. XXXIX. The polymorphism of germanium dioxide," *Journal of the American Chemical Society*, vol. 54, no. 6, pp. 2303–2320, 1932.

[74] M. Stapelbroek, B. D. Evans, and Division, "Exciton structure in the U.V. absorption edge of tetragonal GeO2," *Solid State Communications*, vol. 25, pp. 959–962, 1978.

[75] K. A. Mengle, S. Chae, and E. Kioupakis, "Quasiparticle band structure and optical properties of rutile GeO ¡sub¿2¡/sub¿ , an ultra-wide-band-gap semiconductor," *Journal of Applied Physics*, vol. 126, no. 8, p. 085703, 2019.

[76] H. Peelaers and C. G. Van de Walle, "Lack of quantum confinement in Ga2O3 nanolayers," *Physical Review B*, vol. 96, p. 081409(R), 2017.

[77] M. Feneberg, C. Lidig, K. Lange, M. E. White, M. Y. Tsai, J. S. Speck, O. Bierwagen, and R. Goldhahn, "Anisotropy of the electron effective mass in rutile SnO2 determined by infrared ellipsometry," *Phys. Status Solidi A*, vol. 211, pp. 82–86, 2014.

[78] Q. Yan, E. Kioupakis, D. Jena, and C. G. Van de Walle, "First-principles study of high-field-related electronic behavior of group-III nitrides," *Physical Review B*, vol. 90, p. 121201(R), 2014.

[79] K. A. Mengle, G. Shi, D. Bayerl, and E. Kioupakis, "First-principles calculations of the near-edge optical properties of β- Ga 2 O 3," *Applied Physics Letters*, vol. 109, p. 212104, 2016. [Online]. Available: http://dx.doi.org/10.1063/1.4968822

[80] Y. C. Yeo, T. C. Chong, and M. F. Li, "Electronic band structures and effective-mass parameters of wurtzite GaN and InN," *Journal of Applied Physics*, vol. 83, no. 3, pp. 1429–1436, 1998.

[81] B. Gunning, J. Lowder, M. Moseley, and W. Alan Doolittle, "Negligible carrier freeze-out facilitated by impurity band conduction in highly p-type GaN," *Applied Physics Letters*, vol. 101, no. 8, pp. 0–5, 2012.

[82] J. Neugebauer and C. G. Van De Walle, "Role of hydrogen in doping of GaN," *Applied Physics Letters*, vol. 68, p. 1829, 1996.

[83] K. Bushick, K. A. Mengle, S. Chae, and E. Kioupakis, "Electron and hole mobility of rutile GeO2 from first principles: an ultrawide- band-gap semiconductor for power electronics," *Appl. Phys. Lett.*, vol. 117, no. 18, p. 182104, 2020.

[84] P. Giannozzi, O. Andreussi, T. Brumme, O. Bunau, M. B. Nardelli, M. Calandra, R. Car, C. Cavazzoni, D. Ceresoli, M. Cococcioni, N. Colonna, I. Carnimeo, A. Dar Corso, S. de Gironcoli, P. Delugas, R. A. DiStasio Jr, A. Ferretti, A. Floris, G. Fratesi, G. Fugallo, R. Gebauer, U. Gerstmann, F. Giustino, T. Gorni, J. Jia, M. Kawamura, H.-Y. Ko, A. Kokalj, E. Kucukbenli, M. Lazzeri, M. Marsili, N. Marzari, F. Mauri, N. L. Nguyen, H.-V. Nguyen, A. Otero-de-la Roza, L. Paulatto, S. Ponce, D. Rocca, R. Sabatini, B. Santra, M. Schlipf, A. P. Seitsonen, A. Smogunov, I. Timrov, T. Thonhauser, P. Umari, N. Vast, X. Wu, and S. Baroni, "Advanced capabilities for materials modelling with Quantum ESPRESSO." *Journal of Physics: Condensed Matter*, vol. 29, no. 46, p. 465901, 2017. [Online]. Available: http://arxiv.org/abs/1709.10010

[85] F. Giustino, M. L. Cohen, and S. G. Louie, "Electron-phonon interaction using Wannier functions," *Physical Review B*, vol. 76, no. 16, p. 165108, 2007.

[86] Z. Feng, A. F. Anhar Uddin Bhuiyan, M. R. Karim, and H. Zhao, "MOCVD homoepitaxy of Si-doped (010) β-Ga2O3 thin films with superior transport properties," *Applied Physics Letters*, vol. 114, no. 25, p. 250601, 2019.

[87] M. Horita, S. Takashima, R. Tanaka, H. Matsuyama, K. Ueno, M. Edo, T. Takahashi, M. Shimizu, and J. Suda, "Hall-effect measurements of metalorganic vapor-phase epitaxy-grown p-Type homoepitaxial GaN layers with various Mg concentrations," *Japanese Journal of Applied Physics*, vol. 56, no. 3, p. 031001, 2017.

[88] P. Hermet, A. Lignie, G. Fraysse, P. Armand, and P. Papet, "Thermodynamic properties of the α-quartz-type and rutile-type GeO2 from first-principles calculations," *Physical Chemistry Chemical Physics*, vol. 15, no. 38, pp. 15 943–15 948, 2013.

[89] R. J. L. Andon and K. C. Mills, "The heat capacity of tetragonal germanium dioxide," *The Journal of Chemical Thermodynamics*, vol. 3, no. 4, pp. 583–587, 1971.

[90] S. Chae, K. A. Mengle, R. Lu, A. Olvera, N. Sanders, J. Lee, P. F. P. Poudeu, J. T. Heron, and E. Kioupakis, "Thermal conductivity of rutile germanium oxide," *Appl. Phys. Lett.*, vol. 117, no. 10, p. 102106, 2020.

[91] P. Türkes, C. Pluntke, and R. Helbig, "Thermal conductivity of SnO¡sub¿2¡/sub¿ single crystals," *Journal of Physics C: Solid State Physics*, vol. 13, pp. 4941–4951, 1980. [Online]. Available: http://iopscience.iop.org/0022-3719/13/26/015

[92] S. Chae, H. Paik, N. M. Vu, E. Kioupakis, and J. T. Heron, "Epitaxial stabilization of rutile germanium oxide thin film by molecular beam epitaxy," *Applied Physics Letters*, vol. 117, no. 7, p. 072105, 2020.

[93] C. A. Angell, "Formation of glasses from liquids and biopolymers," *Science*, vol. 267, no. 5206, pp. 1924–1935, 1995.

[94] P. J. Wolf, T. M. Christensen, N. G. Coit, and R. W. Swinford, "Thin film properties of germanium oxide synthesized by pulsed laser sputtering in vacuum and oxygen environments sputtering in vacuum and oxygen environments," *Journal of Vacuum Science Technology A*, vol. 11, p. 2725, 1993.

[95] S. Witanachchi and P. J. Wolf, "Activated reactive laser deposition of GeO2 films," *Journal of Applied Physics*, vol. 76, no. 4, pp. 2185–2190, 1994.

[96] C. N. Afonso, F. Vega, J. Solis, F. Catalina, C. Ortega, and J. Siejka, "Laser ablation of Ge in an oxygen environment: plasma and film properties," *Applied Surface Science*, vol. 54, pp. 175–179, 1992.

[97] C. Caperaa, G. Baud, J. P. Besse, P. Bondot, P. Fessler, and M. Jacquet, "PREPARATION AND CHARACTERIZATION OF GERMANIUM OXIDE THIN FILMS," *Mat. Res. Bull.*, vol. 24, pp. 1361–1367, 1989.

[98] N. R. Murphy, J. T. Grant, L. Sun, J. G. Jones, R. Jakubiak, V. Shutthanandan, and C. V. Ramana, "Correlation between optical properties and chemical composition of sputter-deposited germanium oxide (GeO x) films," *Optical Materials*, vol. 36, pp. 1177–1182, 2014. [Online]. Available: http://dx.doi.org/10.1016/j.optmat.2014.02.023

[99] A. Chiasera, C. Macchi, S. Mariazzi, S. Valligatla, L. Lunelli, C. Pederzolli, D. N. Rao, A. Somoza, R. S. Brusa, and M. Ferrari, "CO 2 Laser irradiation of GeO 2 planar waveguide fabricated by rf-sputtering," *Optical Materials Express*, vol. 3, p. 1561, 2013.

[100] N. Terakado and K. Tanaka, "Photo-induced phenomena in sputtered GeO2 films," *Journal of Non-Crystalline Solids*, vol. 351, pp. 54–60, 2005.

[101] J. Beynon, M. M. E. Samanoudy, and E. L. Shorts, "Evaluation of the composition of reactively evaporated GeOx thin films from optical transmission and XPS data," *Journal of Materials Science*, vol. 23, pp. 4363–4368, 1988.

[102] S. K. Wang, K. Kita, C. H. Lee, T. Tabata, T. Nishimura, K. Nagashio, and A. Toriumi, "Desorption kinetics of GeO from GeO2/Ge structure," *Journal of Applied Physics*, vol. 108, no. 5, 2010.

[103] P. Gross, C. Hayman, and J. T. Bingham, "Heats of Formation of Germanium Tetrafluoride and of the Germanium Dioxides," *Trans. Faraday Soc.*, vol. 62, pp. 2388–2394, 1966.

[104] O. J. Gregory and E. E. Crisman, "Applications of oxides and nitrides of germanium for semiconductor devices," *Integrated Circuits: Chemical and Physical Processing*, vol. 11, pp. 178–220, 1985.

[105] T. Bielz, S. Soisuwan, R. Kaindl, R. Tessadri, D. M. Többens, B. Klötzer, and S. Penner, "A high-resolution diffraction and spectroscopic study of the low-temperature phase transformation of hexagonal to tetragonal GeO2 with and without alkali hydroxide promotion," *Journal of Physical Chemistry C*, vol. 115, no. 19, pp. 9706–9712, 2011.

[106] J. Drowart, F. Degreve, G. Verhaegen, and R. Colin, "Thermochemical study of the germanium oxides using a mass spectrometer: Dissociation energy of the molecule GeO," *Transactions of the Faraday Society*, vol. 61, no. 052, pp. 1072–1085, 1965.

[107] J. H. Kwon, Y. H. Choi, D. H. Kim, M. Yang, J. Jang, T. W. Kim, S. H. Hong, and M. Kim, "Orientation relationship of polycrystalline Pd-doped SnO2 thin film deposits on sapphire substrates," *Thin Solid Films*, vol. 517, no. 2, pp. 550–553, 2008.

[108] K. Fukushima, G. H. Takaoka, and I. Yamada, "Epitaxial growth of tio2 rutile thin films on sapphire substrates by a reactive ionized cluster beam method," *Japanese Journal of Applied Physics*, vol. 32, no. 8 R, pp. 3561–3565, 1993.

[109] P. Vogt and O. Bierwagen, "Quantitative subcompound-mediated reaction model for the molecular beam epitaxy of III-VI and IV-VI thin films: Applied to Ga 2 O 3 , In 2 O 3 , and SnO 2," *Physical Review Materials*, vol. 2, no. 12, p. 120401(R), 2018.

[110] S. Raghavan, T. Schumann, H. Kim, J. Y. Zhang, T. A. Cain, and S. Stemmer, "High-mobility BaSnO3 grown by oxide molecular beam epitaxy," *APL Materials*, vol. 4, no. 1, pp. 28–33, 2016. [Online]. Available: http://dx.doi.org/10.1063/1.4939657

[111] R. H. Lamoreaux, D. L. Hildenbrand, and L. Brewer, "High-Temperature Vaporization Behavior of Oxides II. Oxides of Be, Mg, Ca, Sr, Ba, B, Al, Ga, In, Tl, Si, Ge, Sn, Pb, Zn, Cd, and Hg," *Journal of Physical and Chemical Reference Data*, vol. 16, no. 3, pp. 419–443, 1987.

[112] M. E. White, M. Y. Tsai, F. Wu, and J. S. Speck, "Plasma-assisted molecular beam epitaxy and characterization of SnO2 (101) on r-plane sapphire," *Journal of Vacuum Science Technology A*, vol. 26, no. 5, pp. 1300–1307, 2008.

[113] M. Micoulaut, L. Cormier, and G. S. Henderson, "The structure of amorphous, crystalline and liquid GeO2," *Journal of Physics Condensed Matter*, vol. 18, no. 45, p. R753, 2006.

[114] J. W. Goodrum, "Top-seeded flux growth of tetragonal GeO2," *Journal of Crystal Growth*, vol. 7, pp. 254–256, 1970.

[115] V. Agafonov, M. Michel, A. Kahn, and M. Perez Y Jorba, "CRYSTAL GROWTh BY CHEMICAL VAPOUR TRANSPORT IN THE Ge02-Ga203 SYSTEM," *Journal of Crystal Growth*, vol. 71, pp. 12–16, 1985.

[116] F. Jiang, L. Yang, D. Zhou, G. He, J. Zhou, F. Wang, and Z. G. Chen, "First-principles atomistic Wulff constructions for an equilibrium rutile TiO 2 shape modeling," *Applied Surface Science*, vol. 436, pp. 989–994, 2018. [Online]. Available: http://dx.doi.org/10.1016/j.apsusc.2017.12.050

[117] S. M. Sze and K. K. Ng, *Physics of Semiconductor Devices, 3rd ed. (John Wiley Sons, Hoboken, NJ, 2007)*, 2006.

[118] B. J. Baliga, *Fundamentals of Power Semiconductor Devices (Springer Science Business Media, Berlin)*, 2010.

[119] J. M. Dorkel and P. Leturcq, "Carrier mobilities in silicon semi-empirically related to temperature, doping and injection level," *Solid State Electronics*, vol. 24, no. 9, pp. 821–825, 1981.

[120] M. Levinshtein, S. Rumyantsev, and M. Shur, *Handbook Series of Semiconductor Parameters*, 1996, vol. 1.

[121] A. A. Lebedev, "Deep level centers in silicon carbide: A review," *Semiconductors*, vol. 33, no. 2, pp. 107–130, 1999.

[122] A. S. Barker and M. Ilegems, "Infrared lattice vibrations and free-electron dispersion in GaN," *Physical Review B*, vol. 7, no. 2, pp. 743–750, 1973.

[123] M. E. Levinstein, S. L. Rumyantsev, and M. S. Shur, *Properties of Advanced Semiconductor Materials: GaN, AlN, InN, BN, SiC, SiGe (John Wiley Sons, Hoboken, NJ)*, 2001.

[124] L. Binet and D. Gourier, "Origin of the blue luminescence of β-Ga2O3," *Journal of Physics and Chemistry of Solids*, vol. 59, no. 8, pp. 1241–1249, 1998.

[125] A. Kyrtsos, M. Matsubara, and E. Bellotti, "On the feasibility of p-type Ga 2 O 3," *Appl. Phys. Lett.*, vol. 112, p. 032108, 2018. [Online]. Available: http://dx.doi.org/10.1063/1.5009423

[126] A. T. Collins, E. C. Lightowlers, and P. J. Dean, "Lattice vibration spectra of aluminum nitride," *Physical Review*, vol. 158, no. 3, pp. 833–838, 1967.

[127] Y. Taniyasu, M. Kasu, and T. Makimoto, "An aluminium nitride light-emitting diode with a wavelength of 210 nanometres," *Nature*, vol. 441, no. 7091, pp. 325–328, 2006.

[128] J. Edwards, K. Kawabe, G. Stevens, and R. H. Tredgold, "Space charge conduction and electrical behaviour of aluminium nitride single crystals," *Solid State Communications*, vol. 3, no. 5, pp. 99–100, 1965.

[129] Y. Taniyasu, M. Kasu, and T. Makimoto, "Electrical conduction properties of n-type Si-doped AIN with high electron mobility (¿100 cm2 V-1 s-1)," *Applied Physics Letters*, vol. 85, no. 20, pp. 4672–4674, 2004.

[130] G. A. Slack, R. A. Tanzilli, R. O. Pohl, and J. W. Vandersande, "The intrinsic thermal conductivity of AIN," *Journal of Physics and Chemistry of Solids*, vol. 48, no. 7, pp. 641–647, 1987.

[131] A. Soltani, A. Talbi, V. Mortetb, A. Benmoussa, W. J. Zhang, J. C. Gerbedoen, J. C. De Jaeger, A. Gokarna, K. Haenen, and P. Wagner, "Diamond and cubic boron nitride: Properties, growth and applications," *AIP Conference Proceedings*, vol. 1292, no. November 2010, pp. 191–196, 2010.

[132] D. Litvinov, C. A. Taylor, and R. Clarke, "Semiconducting cubic boron nitride," *Diamond and Related Materials*, vol. 7, no. 2-5, pp. 360–364, 1998.

[133] H. Murata, T. Taniguchi, S. Hishita, T. Yamamoto, F. Oba, and I. Tanaka, "Local environment of silicon in cubic boron nitride," *Journal of Applied Physics*, vol. 114, no. 23, p. 233502, 2013.

[134] L. Weston, D. Wickramaratne, and C. G. Van de Walle, "Hole polarons and p-type doping in boron nitride polymorphs," *Physical Review B*, vol. 96, no. 10, p. 100102(R), 2017. [Online]. Available: https://link.aps.org/doi/10.1103/PhysRevB.96.100102

[135] K. Chen, B. Song, N. K. Ravichandran, Q. Zheng, X. Chen, H. Lee, H. Sun, S. Li, G. A. G. U. Gamage, F. Tian, Z. Ding, Q. Song, A. Rai, H. Wu, P. Koirala, A. J. Schmidt, K. Watanabe, B. Lv, Z. Ren, L. Shi, D. G. Cahill, T. Taniguchi, D. Broido, and G. Chen, "Ultrahigh thermal conductivity in isotope-enriched cubic boron nitride," *Science*, vol. 367, no. 6477, pp. 555–559, 2020.

[136] D. M. Roessler and W. A. Albers, "Infrared reflectance of single crystal tetragonal GeO2," *Journal of Physics and Chemistry of Solids*, vol. 33, pp. 293–296, 1972.